



## Supplementary Materials for **Cortical layer–specific critical dynamics triggering perception**

James H. Marshel\*, Yoon Seok Kim\*, Timothy A. Machado\*, Sean Quirin\*, Brandon Benson, Jonathan Kadmon, Cephra Raja, Adelaida Chibukhchyan, Charu Ramakrishnan, Masatoshi Inoue, Janelle C. Shane, Douglas J. McKnight, Susumu Yoshizawa, Hideaki E. Kato, Surya Ganguli, Karl Deisseroth†

\*These authors contributed equally to this work.

†Corresponding author. Email: [deissero@stanford.edu](mailto:deissero@stanford.edu)

Published 18 July 2019 on *Science* First Release  
DOI: 10.1126/science.aaw5202

### **This PDF file includes:**

Materials and Methods  
Supplementary Text  
Figs. S1 to S19  
References

## Materials and Methods

### In silico opsin screening, molecular cloning, and imaging

For the purpose of finding new classes of opsin genes, *in silico* screening was performed on the data of the Marine Microbial Eukaryote Transcriptome Sequencing Project (27). Transcript sequences were obtained via tblastn search against the eukaryotic transcriptome data using known opsin sequences as a query with the threshold of e-value 0.1; duplicated sequences and sequences shorter than 750 bp were excluded. Then, phylogenetic analysis was performed to search for putative functionally-novel opsin genes; to find channelrhodopsins with high cation conductance, we focused on sequences with more negatively charged amino acids in the transmembrane domains 1, 2, 3, and 7 comprising our structure-resolved ion-conducting pathway and guided by our structure-derived pore surface electrostatic model (see **Supplementary Text**).

The amino acid sequence was human codon optimized and synthesized by Genscript in pUC57 vectors, the gene was subcloned into an adeno-associated viral vector fused with enhanced YFP (EYFP) along with the trafficking sequence (TS) and ER export signal and under control of either the CaMKII $\alpha$  promoter for neuron expression or the Efl $\alpha$  promoter for HEK293 cell expression. For confocal images of opsin-expressing neurons, coverslips of transfected neurons were fixed for 15 minutes in 4% paraformaldehyde and mounted with PVA-DABCO. Images were acquired with a Leica DM600B confocal microscope.

The opsin sequence described herein and discovered via this workflow (from *Tiarina fusus* strain LIS, SEQ\_ID=MMETSP0472-20121206|19186), which we named ChRmine, was edited and used for subsequent functional analysis. The edited sequence was deposited in the GenBank database (accession number MN194599). All transcriptome data used in this study are available in the Marine Microbial Eukaryote Transcriptome Sequencing Project (MMETSP) (27).

*Histology, immunohistochemistry and confocal imaging:* Mice were anaesthetized with isoflurane and Beuthanasia-D, and transcardially perfused in cold 4% paraformaldehyde perfusion fix solution (Electron Microscopy Services, Hatfield, PA, USA). Brains were extracted and kept in the fixation solution for 24 hours at 4° C and then transferred to 30% sucrose in PBS to equilibrate for 2 days at 4° C. 40  $\mu$ m slices were cut on a freezing microtome and stored in cryoprotectant at 4° C. Sections were washed three times for 10 minutes each in 1X phosphate buffered saline (Thermo Fisher Scientific) then incubated for 60 mins in blocking buffer (PBS+0.3% TritonX and 3% normal donkey serum), all at room temperature, while rocking. Sections were incubated with primary antibodies diluted 1:500 in blocking buffer overnight at 4°C. The two primary antibodies used were rabbit anti-GFP (Fisher Scientific A11122) and mouse monoclonal anti-HA tag (Fisher Scientific A26183). Sections were then washed in PBST and incubated in secondary antibodies against rabbit conjugated to Alexa Fluor® 488 (A21206, Thermo Fisher Scientific) and against mouse conjugated to Alexa Fluor® 647 (A-31571, Thermo Fisher Scientific) for three hours at room temperature, diluted 1:500 in blocking buffer. This was followed by three washes of ten minutes each in PBST. The nuclei were stained by DAPI (4',6-diamidino-2-phenylindole) diluted 1:50000 in PBS for 30 min at room temperature, then washed again and mounted on slides with PVA-DAPCO. Confocal imaging of GFP fluorescence (for GCaMP expression), HA antibody staining for localization of the opsin, and DAPI for cytoarchitecture was performed using a Leica TCS SP5 confocal scanning laser microscope with a 20X or 40X oil objective. Co-localization was performed using 40x images (5-6 z slices through each section) by annotating GCaMP6m-expressing cell body locations and then overlaying these annotations and verifying expression in the anti-HA image. Images are displayed in the figure with 1% pixel saturation.

### In vitro characterization with one-photon electrophysiology

The hippocampi of Sprague-Dawley rat pups (Charles River) were removed at postnatal day 0 (P0), and CA1/CA3 regions were digested with 0.4 mg/ml papain (Worthington, Lakewood, NJ) and plated onto 12 mm glass coverslips pre-coated with 1:30 Matrigel (Beckton Dickinson Labware). Cells were plated in 24-well plates, at a density of 65,000 cells per well. The cultured neurons were maintained in Neurobasal-A medium (Invitrogen) containing 1.25% FBS (Fisher Scientific), 4% B-27 supplement (Gibco), 2 mM Glutamax (Gibco) and 2 mg/mL fluorodeoxyuridine (FUDR, Sigma), and kept in a humid culture incubator with 5% CO<sub>2</sub> at 37°C. Primary neuronal cultures were transfected 6-10 days *in vitro* (DIV). For each well to be transfected, a DNA-CaCl<sub>2</sub> mix containing with the following reagents was prepared: 2 µg of DNA (prepared using an endotoxin-free preparation kit (Qiagen)) 1.875 µl 2M CaCl<sub>2</sub>, and sterile water added for a total volume of 15 µl. An additional 15 µl of 2X filtered HEPES-buffered saline (HBS, in mM: 50 HEPES, 1.5 Na<sub>2</sub>HPO<sub>4</sub>, 280 NaCl, pH 7.05 with NaOH) was added, and the resulting 30 µl mix was incubated at room temperature (20-25°C) for 20 minutes. Meanwhile, the neuronal growth medium was taken out of the wells and kept at 37°C, and was replaced with 400 µl pre-warmed minimal essential medium (MEM). The DNA-CaCl<sub>2</sub>-HBS mix was then added dropwise into each well, and the plates were transported to the culture incubator for 45-60 minutes. Each well was then washed three times with 1 mL of pre-warmed MEM, after which the MEM was removed and the original neuronal growth medium was added back into the wells. The transfected neuronal culture plates were placed in the culture incubator for another 6 days.

Recordings in hippocampal cultured neurons were performed 4 - 6 days after transfection in Tyrode's solution: 150 mM NaCl, 4 mM KCl, 2 mM CaCl<sub>2</sub>, 2 mM MgCl<sub>2</sub>, 10 mM glucose and 10 mM HEPES-NaOH pH 7.4. Tyrode was perfused at a rate of 1 – 2 ml min<sup>-1</sup> and was kept at room temperature. Intracellular solution contained 140 mM K-gluconate, 10 mM HEPES-KOH pH 7.2, 10 mM EGTA and 2 mM MgCl<sub>2</sub>. Signals were amplified and digitized using the Multiclamp 700B and DigiData1400 (Molecular Devices, Sunnyvale, CA, USA). The Spectra X Light engine (Lumencor) served as a light source and was coupled into a Leica DM LFSA microscope. Borosilicate patch pipettes (4 – 6 MOhm) were pulled using a P2000 micropipette puller (Sutter Instruments, Novato, CA, USA). HEK293 cells (Thermo Fisher, cells identified by the vendor) were cultured as previously described (58). Cells were transfected using Lipofectamine 2000 (Life Technologies). Recordings in HEK293 cells were performed 12 - 36 hours after transfection in extracellular and intracellular solution as described above.

Voltage clamp recording was performed in the presence of bath-applied tetrodotoxin (TTX, 1µM; Tocris). For initial screening of action spectra, cells were held at resting potential of -70 mV, with 0.7 mW/mm<sup>2</sup> light delivery for 1 second at wavelengths (in nm) of 390, 438, 485, 513, 585 and 650, which were generated using filters of corresponding peak wavelengths and 15-30 nm bandpass. Liquid junction potentials (LJPs) were corrected using the Clampex build-in LJP calculator by subtracting 15 mV from measured values. For reversal potential measurement, HEK293 cells expressing opsins were held at resting potentials from -70 mV to +60 mV (after LJP correction) in steps of 10 mV, with 585 nm, 0.7 mW/mm<sup>2</sup> light delivered for 1 s.

Current clamp measurements were performed in the presence of glutamatergic synaptic blockers: 6-cyano-7-nitroquinoxaline-2,3,-dione (CNQX; 10µM, Tocris) for AMPA receptors and D(-)-2-amino-5-phosphonovaleric acid (APV; 25 µM, Tocris) for NMDA receptors. For light-sensitivity measurements, light was passed through a 585/29 nm filter (Thorlabs) and delivered through a 40x, 0.8 NA water immersion objective. For light pulse-width experiments, 585 nm light with 5 Hz frequency and 0.7 mW/mm<sup>2</sup> intensity was used at varying pulse-width values (in ms) of

0.1, 0.5, 1, 2, 5 and 10. For light sensitivity experiments, 585 nm light with 5 Hz frequency and 5 ms pulse-width was used at varying light power densities (in  $\text{mW}/\text{mm}^2$ ) of 0.002, 0.014, 0.08, 0.28, 0.7, 1.4 and 2.8. For spike fidelity experiments, 585 nm light with  $0.7 \text{ mW}/\text{mm}^2$  power density was used, with 1 ms pulse-width for ChRmine and 5 ms for bReaChES and CsChrimson. For all experiments, 5 - 7 cells were tested, and data collection across opsins was randomized and distributed to minimize across-group differences in expression time, room temperature, and related experimental factors.

For comparison of ChRmine and ChroME (**Fig. S3**), experiments were done in the same patch clamp recording set-up as the red-opsin characterization.  $0.5 \text{ mW}/\text{mm}^2$  lights at 390, 438, 470, 513, 585, 650 nms were used for action spectra measurements. For light pulse-width experiments, lights (585 nm for ChRmine, 470 nm for ChroME) with 5 Hz frequency and  $0.5 \text{ mW}/\text{mm}^2$  intensity were used at varying pulse-width values (in ms) of 0.1, 0.5, 1, 2, 5 and 10 and for light sensitivity experiments, same wavelengths of light with 5 Hz frequency and 5 ms pulse-width was used at varying light power densities (in  $\text{mW}/\text{mm}^2$ ) of 0.04, 0.08, 0.16, 0.25 and 0.5. All experiments were done on the same day, and data collection across opsins was randomized and distributed to minimize across-group differences in expression time, room temperature, and related experimental factors.

#### *In vitro* characterization preparatory to all-optical set-up

Dissociated hippocampal neurons were cultured and transfected with both red opsin variants and GCaMP6m as previously described (58). Coverslips of cultured neurons were transferred from the culture medium to a recording bath filled with Tyrode's solution containing (in mM, 129 NaCl, 5 KCl, 30 glucose, 25 HEPES-NaOH, pH 7.4, 1  $\text{MgCl}_2$  and 3  $\text{CaCl}_2$ ) supplemented with  $10 \mu\text{M}$  CNQX and  $25 \mu\text{M}$  APV to prevent contamination from spontaneous and recurrent synaptic activity. Optical stimulation and imaging were performed using a  $40\times/0.6\text{-NA}$  objective (Leica), sCMOS camera (Hamamatsu, ORCA-Flash4.0) and LED light source (Spectra X Light engine, Lumencor), all coupled to a Leica DMI 6000 B microscope. GCaMP6m was excited by 488 nm (Semrock, LL01-488-12.5) with the Spectra X Light engine. GCaMP6m emission was reflected off a dual wavelength dichroic mirror (Chroma, ZT488/594rpc) for orange light stimulation or another mirror (ZT488/640rpc) for red light stimulation, and passed through a 535-30-nm emission filter (Chroma, ET535/ 30 nm). Red-responsive opsins were activated with a Spectra X Light engine filtered either with 585 nm orange light (Semrock, FF01-585/29-25, 0.2 or  $2.0 \text{ mW}/\text{mm}^2$ ) or 635 nm red light (Semrock, FF01-635/18-25, 0.2 or  $2.0 \text{ mW}/\text{mm}^2$ ).

We used low-intensity 488-nm laser light ( $12 \mu\text{W}/\text{mm}^2$ ) for imaging GCaMP fluorescence without substantially activating red-responsive opsins. Images were acquired at 20 Hz using MicroManager (<http://micro-manager.org>). Light for stimulation was controlled by LabVIEW (National Instruments) and applied every 20 sec at an exposure time of 5, 25, 100, 400 and 800 msec. Imaging data were analyzed in MATLAB (MathWorks). Circular regions of interest (ROIs) were drawn manually based on the averaged image. We performed background subtraction before calculating  $\text{Ca}^{2+}$  signal.  $\Delta F/F$  response was calculated to normalize the signal in each ROI by dividing by its mean value of total fluorescence intensity and subtracting 1. Noise was calculated as the standard deviation of the total  $\Delta F/F$  fluctuation before the first stimulation. S.D. response was then computed as  $\Delta F/F$  response divided by noise. Peak amplitude was calculated from the maximum value between the stimulus onset and 2 sec after the stimulus cessation. To compare red-responsive opsins to triggered GCaMP6m kinetics, we calculated 400 ms exposure-triggered  $\text{Ca}^{2+}$  transients. Rise time ( $t_{\text{peak}}$ ) was defined as the time-to-peak from the beginning of the light

stimulus to the time point at which maximal-amplitude fluorescence was reached. The decay constants ( $\tau$ ) were determined by single exponential fit from the peak of the fluorescence response for 15 sec after stimulation.

#### In vitro characterization in two-photon electrophysiology

All two-photon electrophysiology experiments were conducted on a commercial microscope (Bruker Ultima running PrairieView v5.4) using a Nikon 16x/0.8 NA (CFI75) long-working-distance objective for light delivery. For two-photon stimulation, spiral scanning was performed through a defined spiral ROI with 25  $\mu\text{m}$  diameter, with 12 rotations per spiral, and 4 ms total exposure duration with 80 MHz laser repetition rate (Coherent Chameleon Ultra II). For imaging, a second 80 MHz laser (Coherent Chameleon Ultra II) was relayed through a resonant galvo path for 30 Hz imaging rates, to match the imaging characteristics present for the *in vivo* experiments. As each plane in the behavior *in vivo* imaging experiments was recorded at  $\sim 2.7$  Hz, the imaging rate was appropriately modified by acquiring a new image every 370 ms such that the patched cell was sampled at  $\sim 2.7$  Hz.

The two-photon stimulation and imaging light paths shared a common objective, tube lens and scan lens—but in contrast to the *in vivo* behavior imaging datasets, for the *in vitro* characterization data, the photostimulation galvanometer pair was smaller than the imaging galvanometer pair (3 mm vs. 6 mm). This effectively scaled down the actualized NA for photostimulation from the stated microscope objective values. Experiments were performed with cultured hippocampal neurons expressing ChRmine-EYFP through AAV transfection, and the same intracellular and extracellular solutions for one-photon electrophysiology characterization were used for recording.

For two-photon action spectra and power spectra characterization, recordings were done in voltage clamp mode at holding voltage of -70 mV. Action spectra were measured in randomized trial order at wavelengths (in nm) of 800, 860, 920, 980, 1035, 1080, at the laser power of 20 mW. Power spectra were measured in randomized trial orders at powers (in mW) of 0, 5, 10, 15, 20, 25, 30, at the two-photon wavelength of 1035 nm. All measurements were normalized by the maximum value of the single recording session. Experiments were done in 6 different cells.

For spike fidelity and imaging laser cross-stimulation experiments, recordings were done in current clamp mode, under the membrane potential at -65 mV to -70 mV. Spike fidelity was estimated by stimulation of cells at frequencies (in Hz) of 5, 10, 20, 30, with 1035 nm laser at 20 mW. For cross-stimulation experiments, membrane voltage was observed during image acquisition as a function of imaging power (920 nm, at 2.8 Hz frame-rate) at 0, 20, 40, and 60 mW. Data collection across opsin expressing neurons was randomized.

#### Electrophysiology data analysis

pClamp 10.6 (Molecular Devices), and Prism 7 (GraphPad) software were used to record and analyze data. Statistical analyses were performed with two-tailed unpaired t-test or one-way ANOVA. Data is presented as mean  $\pm$  s.e.m.  $P < 0.05$  is defined to be statistically significant.

For preparation of phylogenetic trees, opsin sequences were first aligned using Clustal Omega server (<https://www.ebi.ac.uk/Tools/msa/clustalo/>) and later calculated using AQUAPONY (<http://www.atgc-montpellier.fr/aquapony/aquapony.php>) and TreeDyn (<http://www.treedyn.org/>) for circular and rectangular trees, respectively, and for rectangular one the lines to leaves were trimmed to fit into a given space. The homology model of ChRmine was

built using the C1C2 crystal structure (PDB ID: 3ug9 (59)) as a template, using RosettaCM method. All molecular graphics figures were prepared with Cuemol (<http://www.cuemol.org>).

### Mouse *in vivo* experiments

*Viral constructs:* The genes for GCaMP6m (60) and soma-targeted (31) ChRmine were cloned in a cis configuration separated by the ribosomal skip motif p2A under the CaMKII $\alpha$  promoter in an AAV2 backbone. This construct was sequenced for accuracy, tested for *in vitro* expression in cultured hippocampal neurons and packaged by the Stanford Neuroscience Gene Vector and Virus Core (GVVC) as AAV8/Y733F to create AAV8-CaMKII $\alpha$ -GCaMP6m-p2a-ChRmine-TS-Kv2.1-HA (used in all mice except for one). AAV8-CaMKII $\alpha$ -GCaMP6m-p2a-ChRmine-TS-HA was used in the remaining single mouse (mouse 2 in behavioral cohort). Maps and sequences are available at <http://optogenetics.org/>, plasmids are available at Addgene (#130988 to 131004), and prepackaged viruses can be purchased from the Stanford GVVC for the following constructs:

pAAV-CaMKII $\alpha$ -ChRmine-eYFP-WPRE  
pAAV-CaMKII $\alpha$ -ChRmine-eYFP-Kv2.1-WPRE  
pAAV-CaMKII $\alpha$ -ChRmine-mScarlet-WPRE  
pAAV-CaMKII $\alpha$ -ChRmine-mScarlet-Kv2.1-WPRE  
pAAV-hSyn-ChRmine-eYFP-WPRE  
pAAV-hSyn-ChRmine-eYFP-Kv2.1-WPRE  
pAAV-hSyn-ChRmine-mScarlet-WPRE  
pAAV-hSyn-ChRmine-mScarlet-Kv2.1-WPRE  
pAAV-Ef1 $\alpha$ -DIO-ChRmine-eYFP-WPRE  
pAAV-Ef1 $\alpha$ -DIO-ChRmine-eYFP-Kv2.1-WPRE  
pAAV-Ef1 $\alpha$ -DIO-ChRmine-mScarlet-WPRE  
pAAV-Ef1 $\alpha$ -DIO-ChRmine-mScarlet-Kv2.1-WPRE  
pAAV-CaMKII $\alpha$ -GCaMP 6m-p2A-ChRmine-Kv2.1-WPRE  
pAAV-hSyn-GCaMP 6m-p2A-ChRmine-Kv2.1-WPRE  
pAAV-CaMKII $\alpha$ -mScarlet-WPRE  
pAAV-hSyn-mScarlet-WPRE  
pAAV-Ef1 $\alpha$ -DIO-mScarlet-WPRE

*Surgery:* All animal procedures followed animal care guidelines approved by Stanford University's Administrative Panel on Laboratory Animal Care (APLAC) and guidelines of the National Institutes of Health. Male C57/BL6 mice (8-12 weeks) were anesthetized with 5% isoflurane for induction and ~1-2% isoflurane during surgery. The skull was exposed, cleaned and coated with a layer of Vetbond (3M). A circular (1 cm diameter, 1 mm height) titanium implant with a counter bore (8 mm outer diameter and 6 mm through hole) was affixed to the skull with Metabond dental cement (Parkell) centered on -2.75 mm (lateral) and -2.25 mm (posterior) from bregma over the lateral portion of primary visual cortex of the left hemisphere (imaging experiments were performed approximately 500  $\mu$ m medial and posterior from this location, and thus were more centrally located within primary visual cortex). The mouse was transferred to a head clamp device designed to firmly hold the metal implant by an angled groove around its perimeter (this same head clamp device design was used to hold the animal under the two-photon microscope and thus had micron-level stability). A circular craniotomy was performed using a high-speed drill by slowly drilling away bone within the perimeter of the through hole of the implant. Once the bone was as thin as possible, but before drilling all the way through the bone,

the remaining intact bone was pulled away with forceps to reveal the underlying cortex with the dura fully intact. A glass pipette injection needle (~25  $\mu\text{m}$  diameter, angled tip) calibrated to the stereotaxic coordinates and filled with the virus was lowered into the cortex to a depth of ~400  $\mu\text{m}$ . 500 nl of virus (typically  $4 \times 10^{12}$  vg/ml) was injected over ~5 min and then the pipette was lowered to ~600  $\mu\text{m}$  and another 500 nl was injected over an additional ~5 min. The pipette was left in place in the brain following injection for at least 3 minutes and then slowly retracted. A 4 mm glass coverslip affixed with UV-cured optical glue (Newport) to a titanium cannula of the same diameter (the cannula also had an ~8mm flange at the top to register with the outer circular implant) was applied the surface of cortex and cemented in place with Metabond. For analgesia up to 72 hours, buprenorphine sustained release (SR) was injected pre-operatively at 0.3-1.0 mg/kg subcutaneously, or buprenorphine (0.05-0.1 mg/kg) was injected by subcutaneous or intraperitoneal injections.

*Visual stimulation:* Drifting sine wave gratings, consistent with high-acuity vision relying on V1 ((60) 0.2 cycles/degree spatial frequency; 2 Hz temporal frequency; 2, 3, 4, 5, 12, 25, or 50% contrast), were generated using custom software in Psychtoolbox running on MATLAB (code available online adapted from (48)) and presented on a calibrated liquid crystal display monitor placed 15 cm from the mouse's eye, centered on the retinotopically targeted location in V1 (48). The gratings subtended 60 deg of visual space and were surrounded by uniform gray around the rest of the screen. A trial began with a 100 ms, 5 kHz tone cue. 1.25 seconds later, the drifting grating was displayed for 3 seconds. The next trial began ~4.5-9 seconds later depending on whether the mouse made an error during the answer window and received a time out as penalty (no time outs were added for naïve mice or mice in the conditioning phase below). A uniform gray screen was presented between drifting grating presentation.

*Behavioral training:* Mice were kept on a reverse day/night cycle. Mice were habituated to the experimenter and to a floating Styrofoam ball and behavior apparatus (Phenosys) for approximately 3 days (the setup was either under the microscope or replicated in a behavioral chamber for initial training before imaging experiments; mice were briefly anesthetized with isoflurane prior to head fixation and allowed to fully recover before proceeding). For discrimination behavior training, mice were water restricted and first allowed to lick freely to trigger immediate water delivery from a lickport by triggering an infrared optical lickometer (Sanworks). This was repeated daily until the animal immediately and consistently consumed water once presented with the lickport. Then, mice were presented with visual stimuli (50% contrast 0 and 90° gratings, see below) using the same trial structure as above, without penalties. If the mice licked during the answer window (1-3 seconds after visual stimulus onset) during the 0° (target) stimulus, they immediately received a water reward (~6  $\mu\text{l}$ ). During this conditioning phase, mice always received ~6  $\mu\text{l}$  of water at the end of target visual stimulus presentation, in addition to any lick-triggered reward. Once mice reliably licked to the target stimulus before the free water was delivered at the end of the trial (mean 6.8 days), they advanced to the discrimination task in which water was only delivered if they licked during the answer window during target stimulus presentation, and time outs (4.5 sec) were added to the end of error trials (misses/false alarms). If the mice did not show discrimination behavior improvement over the course of 4-5 days, a mild air puff directed toward the mouse's face was added as immediate penalty for false alarms. This air puff was eventually added for all mice for consistency. Training continued until mice had nearly 100% hit rates and discriminated 50% contrast gratings with  $\geq 2 d'$  for at least 3

days (mean 9 days total). Then, an equal number of 25% contrast gratings trials were added to the protocol and training continued for 3 days. The same criteria were applied until the task included 2, 12, 25 and 50% contrasts (mice generally could not discriminate 2% contrast gratings). If not done so already, mice were additionally trained under the microscope until behavior was stable to all contrasts before advancing to all-optical experiments.  $d'$  was defined as  $\text{norminv}(\text{Hit Rate}) - \text{norminv}(\text{False Alarm Rate})$  in MATLAB. For the  $d'$  calculation, rates equaling 100% or 0% were adjusted to 99% and 1% respectively. Percent correct was computed for a given condition(s) as  $[(\text{Hits}) + (\text{Correct Rejections})]/(\text{Total Trials})$ .

*In vivo visual and optogenetic stimulation experiments:* Once trained (or in the case of naïve mice, once habituated to the head-fixed floating ball setup under the microscope), mice performed the task (or passively viewed visual stimuli) while volumetric two-photon  $\text{Ca}^{2+}$  imaging was performed in V1 and visual stimuli were presented to the animal. A series of reference images were collected of the volume to aid in alignment to the same region on subsequent days. Neural  $\text{Ca}^{2+}$  responses were analyzed as described below in order to identify ensembles for stimulation on subsequent days/experiments.

Mice returned to the microscope each day and the field of view was aligned to the reference images from the reference experiment. This was accomplished using an automated image registration algorithm (based on the same cross-correlation procedure described below for subsequent analysis) that reported the real-time offsets in pixels between the current imaging field of view (streamed from the microscope acquisition pipeline with minimal latency) and the reference images. In addition, a real-time overlay image was presented to allow the experimenter to optimize x, y, z and  $\theta$  for precise alignment. This was done before beginning the stimulation experiment using several imaging planes throughout the volume. During the volumetric imaging and stimulation experiments, a similar program reported real-time offsets and displayed image overlays (allowing the experimenter to correct for any offsets online using the motorized translation stage), and could be alternated between imaging planes throughout the volume in order to confirm alignment across cortical layers (see **Fig. S9**).

On randomly interleaved trials (usually up to ~312 total trials per session), visual stimuli were presented to the animal or ensemble stimulation (tuned- or random-, target or distractor ensembles) were stimulated with the MultiSLM (see below). For naïve mice, contrasts included 12, 25 and 50%, as well as an equal number of 0% (no visual stimulus), and optogenetic ensemble stimulation occurred on 2/3 of 0% contrast trials (balanced tuned and random ensemble stimulation trials) but was never paired with visual stimulation. Trial order was pseudorandomized for all condition types, and re-randomized if the trial order contained  $> 3$  target, distractor, or low contrast ( $\leq 5\%$ ) conditions in a row. For the behavioral cohort, the same paradigm was used, except optogenetic stimulation could occur alone, or in combination with the visual stimuli (randomly interleaved, balanced trials), and the low contrast condition was exchanged from 0% to 2, 3, 4 or 5% and back to 0% over the course of the contrast ramp experiments. Following the contrast ramp experiments, the low contrast condition was kept at 0% for subsequent experiments (for example, layer-specific ensemble stimulation experiments described below). For the behavior cohort, licking during target stimuli (0° gratings, 0° tuned ensemble or size-matched “0°” designated random ensemble) during the answer window (1-3 sec after stimulus onset) triggered a water reward. Licking during distractor stimuli (90° grating, 90° tuned ensemble or size-matched “90°” designated random ensemble) during the answer window triggered an air puff. Errors (misses or false alarms) resulted in a time out (4.5 sec) at the end of the trial. Importantly, the microscope



hardware performed the same operations on every trial, regardless of condition (e.g., galvanometer spiral scanning, laser shutter opening, imaging scanning pattern, spatial light modulator phase mask transition, etc.), with the exception of the laser power applied to the holograms (either 0 power or power calculated to stimulate the ensemble with 10 mW instantaneous power delivered to each cell for 0.63 ms at ~30 Hz using the MultiSLM timing protocol in **Fig. S4J**, see below), such that all experiment sounds were the same between all conditions. All mice that proceeded through the contrast ramp and simultaneous layer 2/3 and 5 stimulation experiments are included in the manuscript. Four additional mice that proceeded only through the contrast ramp experiment, but in which we increased laser stimulation power beyond the typical protocol (i.e., to attempt to offset weaker stimulation responses) or could not account for z drift over the course of experimental sessions, were excluded.

For analyses in **Fig. 4H,I**, a single one-way ANOVA was performed for each ensemble condition (tuned and random) followed by Tukey HSD post hoc tests. Each data point is from a single session in a single mouse returning to the same tuned and random ensembles, except for the new ensembles condition in which entirely new tuned or random ensembles were stimulated (from a distinct volume/population,  $\Delta z = 30 \mu m$ ) and the no stimulation condition. Conditions with < 10 trials were excluded.

#### All-optical physiology microscope design and characterization

As described in detail below, the all-optical (read/write) microscope used in this manuscript was optimized to address neural ensembles distributed over large volumes beyond millisecond temporal precision for the first time. Achieving these biologically-important specifications required development and optimization of several components, including an entirely new, high-pixel-count, fast spatial light modulator (SLM) with new electronics and software interfaces (MacroSLM), new multiplexing strategies (MultiSLM, **Figs. S4-8**), and a unique pairing with a three-dimensional (3D) imaging strategy during head-fixed mouse behavior.

In prior work, when realizing all-optical physiology using SLMs at high spatial resolution (e.g.,  $NA > 0.4$ ), the addressable targeting volume has thus far been significantly constrained relative to the available imaging volume due to a ceiling on the number and size of available pixels provided with current commercial devices. Furthermore, generation of new ensemble-targeting hologram patterns using near-infrared wavelengths has been limited in overall refresh rate by the SLM response time and the stimulation durations required by previous multi-photon optogenetic opsins and protocols (see, for example, refs (24–26, 32, 61)). This has restricted the ability to write in activity patterns at fundamental biological timescales (~1 ms) over volumes spanning several cortical layers and whole brain areas in the mouse (~0.5-1mm spatial scale). Therefore, we sought a solution where the addressable optogenetic volume meets or exceeds the volume available for imaging, potentially spanning multiple functional areas/volumes across cortical layers—and developed a hardware and biological interface allowing millisecond-level precision of ensemble stimulation during behavior.

*MacroSLM:* To achieve the frame rates, trigger responsiveness, and 3D field of view used in this work, we designed and built a custom liquid crystal on silicon (LCoS) spatial light modulator (SLM). The MacroSLM achieves 500 Hz hologram-to-hologram frame rate at  $\lambda = 1064 \text{ nm}$  at 85% diffraction efficiency (**Fig. S4E**). The square 1536 x 1536 pixel array was selected to provide near uniform 2P excitation efficiency and low chromatic dispersion across the transverse dimensions of the sample at high numerical aperture (NA) (**Fig. S4A,B**) and employs high-voltage (0-12V

analog) pixel addressing, and carefully-timed transient voltages (also known as overdrive (62)), for increased liquid crystal (LC) response speed, requiring development of new driving electronics. In addition, a built-in water-cooled, copper heat sink allows temperature control for the LC to operate at a fixed temperature where LC viscosity is low, thereby improving the maximum refresh rate, while adjusting automatically for illumination- and data-throughput-related heating effects.

*MacroSLM optimization for three dimensional fields of view:* Achieving a large addressable field of view with high spatial precision was a key driving force behind the design of the MacroSLM, influencing the choice of pixel count and pixel size. Pixel count determines the addressable holographic field of view of the microscope when the magnification of the optical system is fixed to image the SLM onto the pupil of the objective lens. The MacroSLM 1536 x 1536 pixel array provides a theoretically addressable field of view of  $\gg 1\text{mm}$  at high NA ( $> 0.4$ ) when using appropriate relay optics and microscope objectives (i.e. a total magnification of 0.469x into the pupil of an Olympus 10x/0.6NA objective, **Fig. S4A**) We designed the SLM with a relatively large 20  $\mu\text{m}$  pixel pitch to achieve several advantages over smaller pixels. The large pixel pitch makes the effect of fringing fields small and minimizes interpixel cross-talk ((63) that would otherwise act like an unwanted low-pass filter on the pattern that the SLM displays). This allows the SLM to maintain high diffraction efficiency (DE) at large steering angles, including when generating large numbers of excitation spots. The resulting large 30.7 x 30.7 mm array allows the input beam to be spread over a large square area which, along with internal light shielding layers, aids peak power handling. The large pixel pitch was also chosen for several important reasons: it enables large voltage swings (here 0-12 V analog), which in turn increases hologram transition speed; it is sufficient to store enough charge (178 fF) to hold the electric field across the liquid crystal while it is switching patterns; and it provides an extremely high fill factor since the active pixel (19.5  $\mu\text{m}$  width) is much larger than the gap between the pixel pads needed to prevent shorting (0.5  $\mu\text{m}$ ). Ultimately, fill factor determines the DE ceiling of the device, with  $\text{DE} = (\text{fill factor})^2 \times \text{pixel reflectivity}$ , or theoretically for this device  $(0.96)^2 \times 0.95 = 0.88$ . This high DE improves overall efficiency of the system while minimizing potential artifacts from non-diffracted light. Also, achieving this DE value through realizing a high-fill-factor obviates the need for a dielectric mirror coating, which is typically used to increase DE, but dielectric mirrors increase the chances of unwanted optical artifacts and are associated with decreased LC response time. Lastly, larger pixels will be responsible for minimizing the lateral chromatic aberration inherent to using the SLM as a diffractive optic when addressing large fields-of-view (maximum deflection angle is  $1.4^\circ$ ) and therefore improve the relative efficiency for multi-photon excitation at the focal spot (64). Our calculations indicate that when using the fixed-wavelength ultrafast laser source reported herein (Coherent Monaco 1035-80-60 at  $\lambda = 1035\text{nm}$ ) at a pulse-width ( $\text{sech}^2$ ) of  $\Delta t \approx 300\text{fs}$  (spectral width of 4.5 nm), a maximum chromatic shift of only  $\pm 0.64\ \mu\text{m}$  would be present at the maximum diffraction angles necessary to address the full-width of the scanned imaged plane (reported herein to be  $710 \times 710\ \mu\text{m}$  with a Nikon 16x/0.8NA objective and  $1020 \times 1020\ \mu\text{m}$  with an Olympus 10x/0.6NA objective).

*MacroSLM liquid crystal speed response:* High-voltage (0–12 V analog) pixel addressing makes the LC response fast, along with the use of high transient voltages (also known as “overdrive”, see ref (62)). ‘Phase wrapping’ was implemented for each pixel to shorten the distance in phase between phase values in time. We also maintain the LC temperature with the use of backplane Peltier heating/cooling, allowing the device to operate at a temperature ( $45^\circ\text{C}$ ) where LC viscosity

is low while also adjusting for the varying heating effects of high-power laser illumination. We optimized the SLM thickness for the use of overdrive at our NIR (~1064 nm) target wavelength, and for maintaining full  $\geq 2\pi$  phase modulation.

*MacroSLM data handling:* Data handling is another significant aspect for increasing speed, since the system must be capable of calculating the required transient voltages to achieve fast LC switching from phase to phase at each pixel, while loading the transient 1536x1536 images onto the SLM pixels at ~1250 Hz continuous frame rate. We use a custom field-programmable gate array (FPGA) solution for handling these high data rates, including on-board storage of 2045 images, on-board application of spatially-varying voltage calibrations, and on-board calculation of individual transient voltages for every pixel. The driver board receives data over a PCIe interface to a Xilinx Kintex-7 primary FPGA. This FPGA distributes the data to 8 secondary Kintex-7 FPGAs using the Xilinx Aurora high-speed serial interface. Each secondary FPGA is capable of performing the overdrive processing for, and supplies the data to, its own section of the SLM (this feature was not yet available for data collected in this manuscript; overdrive frames were precomputed and loaded into the on-board storage for these experiments). The primary FPGA also contains a Microblaze soft microcontroller that performs a number of additional functions, such as loading certain parameters over I2C, temperature monitoring, and automatic safety-shutdown for both the driver board and SLM head. Interruptible image downloads mean that new holograms can be triggered at arbitrary rates exceeding 1 kHz (rather than at integer multiples of the SLM's base refresh rate), without missing triggers. For integration into precisely timed and synchronized experiments, the high-speed triggering system instructs the SLM to transition to the next commanded hologram with low latency and jitter. The latency between a trigger arriving and the voltage changing on the SLM is 6  $\mu$ s with a range of 3-9  $\mu$ s, so that the transition to a new hologram can be very predictably initiated. We developed a MATLAB-based software development kit (SDK) to interface with the SLM. Under these conditions, we could trigger and transition between different holograms at 330-500 Hz with 85-100% target hologram efficiency (**Fig. S4E**).

*All-optical physiology microscope design:* We developed a custom MultiSLM photostimulation path that was integrated into a commercial multi-photon imaging microscope including a resonant-scanner imaging path and piezo-coupled microscope objective holder (Bruker Nano Surfaces Division, Ultima, Middleton, WI). We developed custom optical elements and opto-mechanics, alongside commercial elements when possible, to integrate the optogenetic stimulation path, including the multiple SLMs, into this microscope. The optical path was modeled in both Zemax OpticStudio (Zemax LLC, Kirkland, WA) and MATLAB (The Mathworks, Natick, MA) and optimized to maximize the field of view at the full available back aperture of the microscope (**Fig. S4A, B**). Integration is realized via a two-position drop-down mirror located before the existing uncaging galvanometer unit of the microscope. For the imaging light path, a tunable-wavelength femtosecond pulsed light source is utilized (Coherent Chameleon Ultra II,  $\lambda_{typ.} = 920$ nm, Santa Clara, CA). For the optogenetic stimulation, a fixed-wavelength ( $\lambda = 1035$ nm) femtosecond pulsed light source (Coherent Monaco 1035-80-60, Santa Clara, CA) is used at a user-selected 10 MHz pulse repetition rate. The integrated gate and power-modulation signals of the optogenetic laser were utilized to guarantee zero residual optogenetic-laser illumination on sample. An optical switch (Conoptics LTA360-80 with 302RM driver) (OS, **Fig. 2A**) is used to selectively direct the optogenetic stimulation light towards two alternative paths at 200 kHz temporal resolution, each path with a dedicated SLM. Each path has a 20x beam expander (Thorlabs GBE20-B) (BE, **Fig.**

**2A**) and a custom pair of turning prisms (Edmund Optics, 36°-54°-90° prism, NIRII coated, PN 913418) (TP1 and TP2, **Fig. 2A**, see also **Fig. S7A-E**) to maintain a compact footprint, thereby minimizing mechanical drift issues as well as facilitating simple beam alignment by keeping the optics at 90° angles (**Fig. S7D**). One light path requires a pair of half-wave plates (Thorlabs WPH20ME-1064) (HWP, **Figs. 2A** and **S7D**) in order to maintain optimal polarization alignment through the turning prisms, the SLM liquid crystal alignment layer and the beam combining polarization cube (Thorlabs PBS513) (PBS, **Fig. 2A**). A custom optical relay (Special Optics 54-44-783 AR-coated doublet and 54-8-750 AR-coated triplet) (RL1 and RL2, **Fig. 2A**) was designed to de-magnify the SLM active area at a 5:1 ratio, matching the SLM size to the clear aperture of the dedicated optogenetic galvanometers (OGS, 6 mm clear aperture, **Fig. 2A**) mounted within the commercial multi-photon microscope. This relay was optimized to correct for chromatic aberration, field curvature and distortion. To block residual DC signal from the un-diffracted optogenetic beam off the SLMs, a pair of magnets (D101-N52, K&J Magnetics, Inc, Pipersville, PA) are mounted to each side of a glass cover slip (Fisher Scientific, 12-546-2) and placed in the intermediate image plane of the microscope (located between the two lenses of the SLM relay, BB, **Fig. 2A**). A majority of the optogenetic optical path resides on custom 3D printed optomechanics which facilitates alignment and improves compactness as well as total costs (**Fig. S7F**, for individual mechanical parts the files are available through contacting the authors). The optogenetic galvanometers (OGS, **Fig. 2A**) are utilized to generate the temporal spiral raster scans which trace the SLM-diffracted beamlets across the neuron cell body membranes. The optogenetic and resonant-imaging beams are combined by a dichroic notch filter (Semrock NFD01-1040) (DC, **Fig. 2A**). After both beams are combined, they pass through the commercial scan lens, tube lens and emission filter (SL, TL, and FLTR\_EM, respectively, **Fig. 2A**) before reaching the microscope objective. Axial scanning during image acquisition was realized with a 1 mm-throw piezo-coupled microscope objective (objective for 3D scanning: Nikon 16x/0.8NA (16XLWD-PF), whereas the objective for 2D imaging: Olympus 10x/0.6NA). Optical fluorescence emission is collected by the appropriate microscope objective (OBJ, **Fig. 2A**) and redirected via the emission filter to a collection lens and a pair of PMTs (PMT1 and PMT2, **Fig. 2A**) which collect the red and green fluorescence channels (523/70nm and 627/73nm).

*Precise temporal and spatial optogenetic control:* To increase temporal resolution beyond that achievable by a single SLM capable of operating at up to 500 Hz (**Fig. S4E**), we demonstrated alternating optogenetic excitation from either SLM1 or SLM2 in the MultiSLM system (**Figs. 2C-G** and **S4F**). At the maximum temporal resolution tested, a  $\Delta t_e = 210 \mu\text{s}$  spiral raster scan was designed using a 5-rotation, 10  $\mu\text{m}$  diameter spiral for optogenetic light exposure and validated with the Olympus 10x/0.6 NA physiology objective at 20-30 mW/cell (**S4G, S5A-H**). This spiral was generated by manipulating the Bruker PrairieView (version 5.4U1 r104) generated spiral with the above settings such that the interior 1 $\mu\text{m}$  diameter of the scan was omitted. This short stimulation-duration is many-fold faster than previously reported for *in vivo* two-photon optogenetics (e.g., see refs (24–26)). Post-exposure, each SLM has 1.79 ms to load the next hologram in the sequence, ensuring that the hologram is nearly fully-formed to maximize fidelity and minimize DC illumination before exposing the sample. Therefore, when each SLM is running at 500 Hz and is temporally interleaved at uniform intervals, full 1 kHz temporal resolution is realized (**Figs. 2C-G** and **S4H, S5I-L**). This approach realizes efficient targeting precision across a full 1.03x1.03 mm field of view with little apparent roll-off in optogenetic excitation success rate vs position in the field (**Fig. 2C**), average of 8 randomized trials of the  $e_1$ - $e_6$  ensemble (**Fig.**

**2F**), photostimulation along with control (**Fig. S5J**, please see Data analysis of microscope performance section below for criterion discussion). Alternatively, a burst-mode operation (**Fig. S4I**) is available where both SLM1 and SLM2 are pre-loaded with the necessary holograms and each is sequentially illuminated to expose the sample to an optogenetic illumination pattern, with the sequential temporal difference limited only by the gating time of the Pockels cell (here,  $\Delta t = 80 \mu s$  is conservatively applied). This burst mode operation was employed during all the visual *in vivo* experiments reported herein (**Fig. S4J**) as a means to maximize the number of neurons stimulated per unit time. In those experiments all the targets in the ensemble were randomly distributed across two groups, and each group was assigned an individual SLM for the duration of the experiment. Note that all three-dimensional holograms are calculated as discussed in (65).

In order to image multiple axial planes, we opted for a lighter microscope objective (Nikon 16x/0.8 NA) to reduce the inertial mass burden on the rapidly scanning piezo to help maintain its lifetime. Notably, this solution using a piezo-scanning objective does allow for rapid scanning across multiple axial layers while maintaining the ideal optical imaging performance of the microscope (**Fig. S4C**). Despite the temporal lag of acquiring an image from each axial slice (33 ms per slice), the optogenetic photoexcitation can be performed volumetrically, simultaneously. Using the viral vector approach taken here, selective expression is observed in layer 2/3 and layer 5 (**Fig. 2B**) and three-dimensional, simultaneous optogenetic excitation is realized across the full volume of  $0.71 \times 0.71 \times 0.37 \text{ mm}$ , capable of targeting layer 2/3 through layer 5 in this preparation (**Fig. S6L,M**, 30 Hz at 20 mW/cell at the objective, 0.63 ms, 9 rotations, 15  $\mu m$  spirals). This spiral was generated by manipulating the Bruker PrairieView (version 5.4U1 r104) generated spiral with the above settings such that only the final 630 $\mu s$  are used. This was also the configuration used for all *in vivo* visual experiments, except the power was reduced to 10 mW/cell at the objective (see below); thus, the characterization measurements at higher power described here are conservative with regard to stimulation spatial precision. Note that losses due to scattering were assumed (mean scattering length,  $\rho = 150 \mu m$ ) and that the power delivered to targets at different depths ( $z$ ) would each be scaled by adding an amplitude term to each target in the hologram (65) weighted by the function ( $\sqrt{e^{z/\rho}}$ ).

In order to assess the potential for putative ‘off-target’ excitation from our optogenetic illumination, we quantified the relative fluorescence modulation of neighbors to the targeted location. Under the system configuration **Fig. S4A**, and during the same experiment reported in **Fig. 2C**, we had randomly interleaved trials where variable ensemble sizes ( $N=25, 50$  and  $160$  temporally interleaved) were targeted, in addition to control trials with no optogenetic intervention. The pixel-wise  $\Delta F/F$  across the entire images are shown in **Fig. S5A-C** and **G-I**, to facilitate visual inspection of the data for successful target stimulation across the field as well as potential ‘off-target’ excitation. One second of data pre-stimulus was used to calculate the baseline value and the mean value of the final 2.5 seconds of optogenetic stimulus was used to calculate the  $\Delta F/F$ . To further evaluate this potential, we highlight one ROI and document where putative neurons have been identified via application of a CNMF algorithm relative to the targets (**Fig. S5D**). Four target neurons and 20 neighboring neurons were selected for viewing the  $\Delta F/F$  traces in **Fig. S5E**. The traces are generated by making the CNMF masks into binary spatial filters and then performing the  $\Delta F/F$  calculation on the data. To quantify the potential for a neighboring neuron to be excited by a nearby target, we plot the average  $\Delta F/F$  of putative neurons as a function of the distance to any target (**Fig. S5F**). The distance metric was calculated using the ROI centroids of neighboring neurons and pooling all neighbors which would reside in annular rings separated in  $10 \mu m$  increments. The average  $\Delta F/F$  of all neighboring neurons was normalized by the average  $\Delta F/F$  of

all targets (see discussion below in data analysis). This analysis indicates that while the optogenetic stimulus is spatially-precise, a nearby neighbor separated  $<20\mu\text{m}$  away from the target neuron may occasionally experience associated excitation. We note that it is not clear the degree to which this neighboring excitation is related to stray light, local synaptic connectivity or poor target selection. To present a clear summary of this conclusion, we identify one region of the field where both a tight cluster of neurons was occasionally stimulated while also there were trials with only a single member of the cluster stimulated. By requiring that a cluster of neighboring neurons was stimulated, we have a positive control that the neighboring neurons express the opsin. In **Fig. 2G**, we presented the intensity images of the local field-of-view during the optogenetic stimulus window (top) for cases of spontaneous activity, single-target stimulation and multiple-target stimulation. Note that the images have been scaled to the maximum intensity of the multiple target image to view the differences across all pixels in that field-of-view. In the bottom row, we present the associated traces of nearby neurons which are in this positive control group.

To further assess the spatial optogenetic precision of our stimulation system, we selectively targeted optogenetic perturbations to be localized by anatomical perturbation only to layer, including L4 where expression is not present in the cell bodies (**Fig. S6L**). We measured all resulting activity in unbiased fashion across the entire imaged volume by subsampling the images into  $8\times 8$  pixel bins and reporting the modulation in fluorescence during optogenetic perturbation as a function of the tissue depth from the most superficially sampled image. As expected, based on the precision of the point spread function of our system (0.48 NA, **Fig. S6A, B**), layer 4 stimulation did not yield activity modulation in neighboring layers (**Fig. S6M**). In the same experiments, on randomly interleaved trials, we stimulated neurons in layer 2/3 and/or 5 for comparison, which elicited robust responses. It is also important to note that, as a result of the axial translation of the microscope objective during volumetric imaging, the spiral-scan stimulation will correspondingly be slightly tilted through the cell body, relative to normal. However, this is minimized in our setup due to the short exposure times required with this opsin/optics combination. As an example, the maximum axial slew rate of the objective in our experiments was  $\sim 2\ \mu\text{m}/\text{ms}$ . Since all individual exposures in the protocols introduced in **Fig. S4G-J**, and used throughout the manuscript, are below 0.63 ms, we expect a maximum axial blur due to microscope objective motion to be  $\leq 1.2\ \mu\text{m}$ .

Lastly, as the optical characteristics of brain tissue are typically unfavorable for deep imaging and photo-stimulation, as compared to the performance at superficial depths, we quantify the influence of tissue depth on our optical and optogenetic performance. Concerns, such as the increased likelihood of scattering events, as well as greater aberrations due to the propagation of light through a greater amount of inhomogeneous tissue, are known to contribute to non-ideal performance and, as a result, much effort within the neuroscience and optical sciences community has been placed towards minimizing these losses through compensating measures such as adaptive optics. With respect to the optical performance reported in this manuscript, we note that the spiral scanning of the photo-stimulation beam across the cell in the transverse dimension results in an illumination pattern  $\sim 10\times$  larger than the ideal transverse point spread function (PSF). As a result, we believe that aberrations of the PSF in this dimension would minimally increase the total size and therefore targeting precision would remain relatively robust from L2/3 (**Fig. S6C**) to L5. However, the axial elongation of the PSF may be critically influenced by these effects and we will therefore document our findings.

To quantify the influence of optical quality on tissue depth, we use our MultiSLM to raster-scan a focused optogenetic beam into the exact same sample prep used in the behavior experiments.

A 3D, in vivo image stack is acquired which spans from the dura to layer 5. Naturally present lipofuscin granules are utilized as red fluorescent point source proxies (**Fig. S6D**) since they are uniform in size throughout the acquired volume (actual transverse FWHM was measured to be  $\sim 8\mu\text{m}$ ). We document that the relative axial elongation of this PSF proxy from L2/3 to L5 is  $\sim 3\mu\text{m}$ , or  $\sim 20\%$  of the ideal PSF (**Fig. S6F,G**). To place this in context, Layer 2/3 cortical neurons are typically  $15\mu\text{m}$  in diameter and Layer 5 slightly larger (we measured  $\sim 2\mu\text{m}$  larger in transverse extent from in vivo data), so this broadening of the PSF is still a small fraction relative to the cell body.

Given this measure for the expected axial elongation of the PSF using lipofuscin as proxy beads, for reference we next compare with the axial FWHM measurements of imaged neurons found in the simultaneously acquired GCaMP channel of the 3D image stack (**Fig. S6E**). From this measurement, we observe a relative difference in the measured axial FWHM of the neurons in L2/3 vs L5 which is greater than that expected from optical effects alone ( $\sim 8\mu\text{m}$ , **Fig. S6H,I**). This remains consistent with the expectation that the average cell body size is larger in Layer 5 relative to Layer 2/3. Taken together, these observations indicate that while we do observe some relative axial elongation to be present, the degree of this elongation may scale proportionally to the relative increase in neuron cell body size. Also, the absolute size of the PSF remains well-matched to the size of a cell body target in either L2/3 or L5. As a result, we would expect there to be no relative increase in off-target photo-stimulation in Layer 2/3 relative to Layer 5.

To directly address this question of axial optogenetic excitation precision, we replicate the same conditions as the bias experiments (**Fig. 6**) (e.g. 6 image planes spaced  $65\mu\text{m}$  apart, same optogenetic stimulation power, etc.) and axially displace ( $dz$ ) the target spots in order to map this effect onto the neural activity readout (**Fig. S6J, K**). Specifically, we focused on the experiments when  $N = 4$  targets were simultaneously excited in alternatively L2/3 or L5, as this was where we observed the differential threshold for driving behavior. For these measurements, trials were randomly interleaved with the projected optogenetic stimulation pattern being axially displaced randomly from  $-65 < dz < 65\mu\text{m}$  in  $5\mu\text{m}$  intervals (5 trials at each  $z$ -offset). The results demonstrate an optical physiology PSF with no clear bias of L5 over L2/3 (FWHM =  $27.7 \pm 9.1\mu\text{m}$  vs  $26.3 \pm 6.0\mu\text{m}$  from Gaussian fit to the data, error is reported as 95% confidence interval), respectively,  $N = 7$  neurons each) and is in agreement with our inferences from the prior measurements.

*Imaging and Optogenetic beam alignment:* Spatial alignment of the targeting and imaging beams was accomplished by using the SLMs and optogenetic galvanometers to burn a constellation of holes into a thick fluorescent slab and then to register them to the collected imaging frame via manual identification of the hole centroids. A rigid, affine transform was defined for each axial position (at up to 7 axial planes) and a linear fit was implemented to characterize how each of the 9 affine transform coefficients would vary as a function of axial plane. This fit was stored and later recalled when generating the hologram patterns to be generated for targeting identified neurons in the sample. The axial localization of the imaging and optogenetic stimulation beams was characterized by measuring the fluorescence signal as a thin fluorescence slab ( $< 5\mu\text{m}$ ) was translated through the beam (**Fig. S6A**).

The phase control afforded by the SLMs was exploited in two additional capacities to mitigate inherent optical challenges. First, due to the non-unity fill-factor of the SLM, a fixed amount of light will remain un-diffracted from the SLM and be focused in the sample plane unless mitigating steps are taken. First, we addressed this by placement of a beam block, in the form of a

pair of magnets mounted to a cover slip (BB, **Fig. 2A**) in the intermediate image plane located between relay lens 1 and 2 (RL1 and RL2). This effectively blocked any light from undesirably focusing into our sample plane. To further address any potentially un-blocked, un-diffracted light focusing in the sample, we opted to de-collimate the beam expander (BE, **Fig. 2A**) such that the native foci of the SLMs were located approximately  $300 \mu\text{m}$  above the native imaging plane of the microscope objective. This axial shift of the native SLM focal plane was compensated by adding a complementary focusing and spherical aberration correction term to the SLM phase mask, such that the un-diffracted illumination focuses  $\sim 300 \mu\text{m}$  above the targeting volume. The second capacity in which the SLMs were exploited to mitigate optical challenges was by employing an optical aberration correction algorithm which accounted for a) slight deviations from phase uniformity across the entire  $30.7 \times 30.7 \text{ mm}$  face of the SLM and b) potential aberrations from optical misalignment or inherent to the optics. The aberration correction was realized by manually adjusting the weights of a linear summation of Zernike polynomials (up to  $Z^{16}$ ) to account for the phase aberration (**Fig. S4D**), as measured by maximizing the fluorescence signal excited from a thin layer ( $< 5 \mu\text{m}$ ) of fluorescent material on a glass slide (66). The dominant phase errors were found to be astigmatism and spherical, with an additional defocus term which accounted for making the optogenetic target and the imaging plane effectively co-planar. The astigmatism phase correction likely compensated for any residual surface error not already corrected by the SLM look-up table.

*Optical power considerations for all-optical physiology:* It is worthwhile to note that in addition to considering instantaneous power, the time-averaged power into the sample (which is most likely related to brain heating) is minimal due to the very low duty cycles of each optogenetic photo-excitation exposure. For example, to target all 160 cells shown in **Fig. 2C-G** required only:

$$\frac{30 \text{ mW}}{\text{cell}} \times 160 \text{ cell} \times \left( \frac{29 \text{ Hz} \times 0.21 \text{ ms}}{1000 \text{ ms}} \right) = 29.2 \text{ mW}$$

of average power during the 3 seconds of optogenetic stimulation. Further reducing time-averaged power into the brain, optogenetic stimulation epochs were generally a fraction of the total trial time (e.g., minimum 3 out of 8 seconds in behavioral trials).

For all behavior-related imaging experiments (e.g. Figs. 3-6), we image 6/11 frames for one piezo-scanned volume (5 frames are dropped on piezo flyback) at 2.75Hz, thereby reducing the duty cycle of imaging laser illumination to 55%. Total heat load is bound between the lowest imaging power in L2/3 (30mW) and the maximum in L5 (120mW), where the imaging power was scaled with an exponential gradient value of 7.62 to continuously adjust power for each imaging plane (using Bruker PrairieView). This corresponds to imaging powers of  $P_{plane} = 30, 40, 52, 70.4, 93.7$  and  $120\text{mW}$  at nominal axial piezo positions of 0, 65, 130, 195, 260,  $325\mu\text{m}$ , respectively. Therefore, assuming the per plane duty cycle as  $D_{plane} = \frac{1}{11}$ , an estimate of the total average heat load to the sample would be,

$$\sum_{N=1}^6 D_{plane} P_{plane,N} = 36.9 \text{ mW}$$

from the imaging laser, where N is the index for each plane. Optogenetic stimulation from the objective was  $< 10\text{mW}$  per target in L2/3 and scaled to an absolute maximum of  $< 120\text{mW}$  per target in L5 in order to compensate for scattering losses from additional tissue ( $10\text{mW} \times e^{-\frac{370\mu\text{m}}{\tau}}$



), assuming a scattering length of  $\tau = 150\mu\text{m}$ . Stimulation was delivered in 0.61ms durations at 30.206Hz for a time-averaged power of [0.18-2.2mW] per target. In general, the combined time-averaged power including imaging and optogenetic stimulation lasers during visual experiments was  $< 50 \text{ mW}$ .

*Mitigation of photo-stimulation artifact in images:* As noted elsewhere (25, 26), the optogenetic stimulation creates an image artifact due to the excitation of GCaMP in the targeted cells. Here, due to the low-duty cycle of the optogenetic stimulation, this artifact is present in only a small percentage of the imaging pixels (e.g., one 210  $\mu\text{s}$  optogenetic stimulation will create artifact in only 0.6% of the total image). Furthermore, the artifact band is dithered across trials such that when the artifact pixels are excluded from any individual trials (see below), the trial-averaged results will reconstruct a full, artifact-free image (**Fig. S8**).

*Data analysis of microscope performance:* Multi-photon imaging data in **Figs. 2, S5, and S6** was processed in MATLAB (R2017a, The Mathworks, Natick MA). Non-overlapping ROIs were defined from manual selection of targets. After defining the regions of interest (ROIs), the image movies were Kalman filtered (gain = 0.5, noise = 0.05) and data was then extracted by using each ROI as a binary mask and calculating the mean signal for each image frame. From this time-series ROI signal, the  $\Delta F/F$  was calculated using the mean of the final 1/5 duration of the time-series data as the baseline measurement of each respective ROI. In **Fig. 2C**, for a neuron ROI to be deemed a positive optogenetic stimulation it must pass the following two criteria: a) the difference of the mean signal from the stimulation signal and the pre-stimulation baseline must be greater than  $2\sigma$  ( $p \leq 0.025$ ), and b) the difference of the mean signal and the post-stimulation baseline must be greater than  $2\sigma$  ( $p \leq 0.025$ ). Note that the trial-averaged artifact in **Fig. 2C-G** was negligible due to: the phase offset of the image acquisition (30 Hz) and the optogenetic stimulation (29Hz), which decreased the probability of the artifact being present in the same pixel across sequential frames; the minimal duration / line width of the artifact ( $\frac{210\mu\text{s}}{64.9\mu\text{s}/\text{line}}$  lines for each group in the stimulus, accounting for 3.8% of the image).

#### Data analysis of *in vivo* visual experiments

*Preprocessing of in vivo visual experiment imaging data and selection of stimulated ensembles:* Raw imaging data were loaded into MATLAB (R2016a, The Mathworks, Natick MA) and analyzed using built in functions, MATLAB Distributed Computing Server, and custom scripts. To reduce processing time by  $\sim 6$  fold ( $n$  slices) and facilitate activity-guided experiments, raw images ( $\sim 40,000$  images per session, per channel) were processed in parallel in a computing cluster in which each optical slice (a defined depth in the volume) was processed by a single multi-core computing node. Data was served to each node by a high-performance data server in RAID 1+0 configuration in a 10-Gigabit network.

Any pixels in the image that were collected during optogenetic stimulation were replaced with “not a number” (NaN), and omitted from all subsequent analyses. Images from a single imaging plane in the volume were aligned to a reference image by determining the highest cross-correlation coefficient between each image and the reference image in a 20-pixel shift-window in X and Y. For the reference visual-only experiment, the reference image was defined as the average image of frames 10-50 from the imaging session. For each subsequent imaging session, the cross-correlation alignment procedure was repeated in the following order. First, the reference image was defined as the average of all images from the aligned, already motion-corrected visual-only

experiment. The cross-correlation algorithm was applied to determine the optimal shifts to align Kalman filtered (gain = 0.5, noise = 0.05) imaging data from the current session to the reference experiment. These shifts were applied to the raw (non-Kalman filtered) data. A new reference image was defined as the mean image across the current, aligned dataset, and used to perform a final cross-correlation based motion correction for the current dataset. In this way, each session's dataset was aligned to the reference experiment using temporally-smoothed data, and further fast-motion corrected using its own reference.

Aligned imaging data from the reference visual-only experiment were input into the constrained nonnegative matrix factorization (CNMF) algorithm (67). The spatial components estimated by CNMF were alone used to define a single set of cell masks across experimental sessions. Time courses for each cell were defined by averaging pixels within each cell mask for each image frame. Cell time course data were organized by trial, and baseline-normalized (to compute  $\Delta F/F$ ) by the following formula:  $(R_i - F)/F$ , where  $R_i$  is the cell's fluorescence at each time point  $i$ , and  $F$  is the cell's mean fluorescence during the three frames before a visual or optogenetic stimulus for each trial. No neuropil subtraction was applied to the data. The rigid alignment algorithm described above (well-suited for the high-speed imaging data, with minimal warping in each 33ms frame), and alignment of the imaging volume to the reference experiment during each session (maintained in real-time using online cross-correlation software during image acquisition, see above), allowed us to use the same cell masks across sessions in order to conserve cell identity.

Tuned ensembles were defined as neurons (any mask segments resembling dendrites were removed by visual inspection) which responded robustly and reliably (at least 3 of 8 time points  $> 0.3 \Delta F/F$ , and  $p < 0.05$  t-test stimulation epoch versus baseline) to either the  $0^\circ$  or  $90^\circ$  50% contrast visual stimulus, with an orientation selectivity index (OSI) greater than 0.5. OSI was defined by the following formula:  $(R_{\text{pref}} - R_{\text{orth}})/(R_{\text{pref}} + R_{\text{orth}})$ , where  $R_{\text{pref}}$  is the response during the visual stimulus to the preferred orientation, and  $R_{\text{orth}}$  is the response to the orthogonal orientation. For these analyses of the reference visual experiment (but not subsequent analyses), cell time courses were Kalman filtered (gain = 0.5, noise = 0.05) before computing  $\Delta F/F$ . Tuned ensemble sizes were  $0^\circ$ : 32, 26, 27, 37 and  $90^\circ$ : 19, 40, 33, 26 for each mouse in the naïve cohort, respectively (Naïve Mouse 1-4). Tuned ensemble sizes were  $0^\circ$ : 55, 42, 33, 53, 33, 32, 29 and  $90^\circ$ : 38, 37, 28, 46, 42, 45, 46 for each mouse in the behavioral cohort, respectively (Trained Mouse 1-7). Random ensembles were randomly selected from the remaining population across the volume to match the number of neurons in the respective tuned ensembles. For stimulation of sub-ensembles in each cortical layer, either all of the neurons from the tuned ensemble from an anatomically-defined layer were used, or a randomly selected subset of those neurons was used, where the number of neurons was defined for each subset tested.

*Statistical analysis of co-activity:* Stimulated neurons and any neuron masks containing pixels within a  $20.85 \mu\text{m}$  (15 pixels) radius, including any neurons above or below stimulated neurons within a cylinder with the same radius, were excluded from all analyses of co-activity. On each day, high contrast visual trials (50% contrast; no optogenetic stimulation) were used to find reliable (significant two-tailed Wilcoxon signed-rank test, MATLAB function, frames 5 and 6 versus baseline frames 2 and 3), orientation selective (OSI  $> 0.5$ , calculated as above) neurons. Importantly, frames 5 and 6 occurred during the "Sample Window", that is during the visual or optogenetic stimulus but before any water reward or air puff was delivered. These reliable, orientation-selective neurons, which were distinct from the original tuned ensembles as described above, were used to define the tuned populations for network analyses. Neurons within these tuned

populations that reliably increased fluorescence across trials of a specific optogenetic ensemble condition (significant two-tailed Wilcoxon signed-rank test, frames 5 and 6 versus frames 2 and 3, Figs. 4J-N, S12A,B:  $p < 0.05$ , Figs. 5D,E, 6A-D, S15A,B:  $p < 0.01$ ) were deemed co-active. To define the fraction of co-active neurons for each condition, the number of co-active neurons was divided by the number of tuned neurons.

For scatter plots, each data point is the result from a single optogenetic ensemble stimulation condition from a single day. Relationships between the number of stimulated neurons and the fraction of co-active neurons were computed using the Spearman's correlation coefficient, with significance defined by a two-tailed test versus no correlation (built in MATLAB function). To statistically compare  $\rho$  values, a two-tailed Fisher's z transformation was performed.

For bar graphs, the number of co-active neurons and tuned neurons were each summed across sessions for each mouse to define each mouse-identified data point plotted on the figure, and across mice for summary data. A two-tailed Pearson's chi square test was used to statistically compare frequencies of co-activity on pooled data across mice between conditions (SPSS). To account for the contribution of mouse identity, additional statistics are presented here using the Cochran-Mantel-Haenszel (CMH) test, in which data are stratified by mouse identity. The CMH tests yielded comparable results to the Pearson's chi squared test in all instances. A Breslow-Day test was run to test the assumption of homogeneity of the odds ratio for each CMH test. The Breslow-Day test rejected the null hypothesis that the odds ratio was equal across mice for the following statistical tests, implying that an interaction may have existed between mouse identity and observed co-activity counts. These included Tuned After Contrast Ramp (**Fig. 4L**), Random After Contrast Ramp (**Fig. 4M**), Tuned vs. Random Before Contrast Ramp (**Fig. 4N**), Tuned vs. Random After Contrast Ramp (**Fig. 4N**), Iso vs. Ortho (**Fig. 5D**), Layer 2/3 vs Layer 5 Iso Tuned (**Fig. 6C**), Layer 2/3 Iso vs. Ortho (**Fig. S15A**), and Layer 5 Iso vs. Ortho (**Fig. S15A**). Pearson's chi square tests were run independently for each mouse for each of these instances and were found to be significant to at least  $p < 0.05$  for 4/5, 4/5, 4/5, 3/5, 5/5, 3/4, 5/5, and 5/5 mice, with effect directions always matching the pooled data, for each of these comparisons respectively. Layer 2/3 vs. Layer 5 Iso Tuned (**Fig. S15A**) had 4/5 mice with significant Pearson's chi square tests ( $p < 0.001$ ) going in the direction of increased layer 5 recruitment vs. layer 2/3, and Mouse 3 had greater layer 2/3 recruitment than layer 5 ( $p = 0.046$ ).

*Statistical analysis of neuronal dynamics:* All classifier and neural decoding analyses were performed in Python 3.6 and used open source libraries listed below. This analysis is presented in parts of **Fig. 3**, **Fig. 5**, and **Fig. 6** as well as all of **Fig. S10-S15** (except for **S12A**).

*Neural decoding analysis using sparse logistic regression:* In order to select cells to include in our neural decoding analysis for a given mouse, we first identified all neurons that were ever optogenetically stimulated on any experimental day or condition. Then we defined a column of exclusion with an approximately  $20.85 \mu\text{m}$  (15 pixel) radius around each of these stimulated neurons to conservatively identify any neuron that might have been erroneously stimulated during our experiments. Other neurons whose fluorescence signals were contaminated by stimulation artifacts were also removed during this process (see above). This neuron selection procedure differs slightly from the one used for the statistical analysis of co-activity (see previous methods section) in that all neurons that were *ever* stimulated in a mouse (plus surrounding neurons) were excluded on all days to facilitate training regression models that generalize between experiments where different ensembles were optogenetically stimulated.

Our regression models were trained only on experimental trials where mice watched a visual stimulus and no neurons were optogenetically stimulated. Specifically, for each experimental day, we found each condition where a visual stimulus was presented (at any contrast between 12-50%). Then from each one of these trials, we computed the average fluorescence of each neuron across two fluorescence frames after stimulus onset (frames 5 and 6 of 19 total imaging frames/trial; the same frames used for co-activity analyses above). These two frames were specifically chosen to eliminate the frame where fluorescence was rising at the onset of the visual stimulus (frame 4) and to also eliminate the later frames during the stimulus where either a water reward or punishing air puff could have been delivered. This process yielded a vector of length equal to the number of unstimulated neurons in each dataset, for each trial. We concatenated each of these vectors into a matrix of size equal to the number of trials by the number of unstimulated neurons. Importantly, only this visual-stimulus-only data was ever used to train our regression models. The same models were then used to predict condition type (target vs. distractor) on all other kinds of data (i.e. during optogenetic stimulation of different types). This procedure was identically followed in both the behavioral cohort of mice (where reward and airpuff stimuli were present) and the naïve cohort of mice (where neither stimulus existed).

We then took this data matrix and another vector containing the true stimulus type (target, 0° or distractor, 90°) and used them to fit a set of sparse logistic regression models. This procedure was repeated independently for each mouse. To perform the regression model fitting, we used a class in Python's scikit-learn package named LogisticRegression with the penalty argument set to 'L1.' Each of the five models was trained on a distinct random fifth of all of the trials presented (five-fold cross validation). Classifier weights and predictions reported are means across all five of the regression models trained for each mouse. Finally, we found that across all  $n = 5$  behavioral mice (**Fig. S12**) and  $n = 4$  behaviorally naïve mice (**Fig. S10**), setting the sparseness parameter ( $1/\lambda$ ) equal to 0.5 approximately minimized the training error in each case. Models generating all results reported had  $1/\lambda$  set to this value.

Across  $n = 4$  behaviorally naïve mice (and 2 tuned + 2 random ensembles for each mouse; 60 stimulation trials from each neuron were used in this analysis), we tested that the effective size of the tuned and random optogenetically-stimulated ensembles was comparable. This was computed by using a Wilcoxon signed-rank test to compare the average fluorescence in the baseline period (frames 1 and 2) to the average fluorescence after optogenetic stimulus onset (frames 5 and 6) across all individual trials from each targeted neuron. The significantly recruited fraction of tuned ensembles ranged from 0.4-0.92. This fraction for random ensembles ranged from 0.37-0.74. A paired t-test revealed no significant difference between these two distributions, ( $p = 0.48$ ) (**Fig. S10C**).

This same analysis was also applied to  $n = 3$  behaviorally trained mice (40 stimulation trials/neuron were used for this analysis; there were 2 tuned and 2 random ensembles analyzed for each mouse). In contrast to the naïve mice, our conservative metric found that there was a significant difference in stimulation efficacy between the size-matched random and selective ensembles. The significantly recruited fraction for tuned ensembles ranged from 0.58-0.9. For random ensembles it ranged from 0.26-0.75. A paired t-test revealed a significant difference here, \*\*\*  $p < 0.001$  (**Fig. S12D**).

*Neural trajectory analysis using PCA:* In a similar manner to the procedure described above for our decoding analysis, we used Principal Components Analysis (PCA; scikit-learn class PCA) to visualize the average population response of all trials of an identical experimental condition, on a

given experimental day. Principal components were identified using a data matrix composed of the mean fluorescence responses across all neurons to both the target, 0° and distractor, 90° visual stimuli (contrast ranged from 12 to 50%; in the absence of any optogenetic stimulation). Since each trial was 19 frames long, this yields a training matrix of size: (19 x 2) x number of neurons. The first two principal components estimated from this data matrix were used to plot all neural trajectories for an individual mouse in all experimental conditions.

A similar analysis using Partial Least Squares Regression (scikit-learn function PLSRegression) was performed with the identical data matrices, but also with ground truth visual stimulus information (target, 0° vs. distractor, 90°). This approach yielded nearly identical results to PCA—despite the fact that the latent dimensions were explicitly derived to separate target from distractor conditions, rather than to simply maximize variance explained (**Fig. S14**).

*Psychometric curve fitting:* To assess the relationship between either neural or behavioral performance and the size of an optogenetically stimulated ensemble, we used an open-source package called Psignifit-python (68) to fit logistic psychometric curves of the following form:

$$\psi(x) = \gamma + (1 + \lambda - \gamma) S(x; m, w)$$

$$S(x; m, w) = \frac{1}{1 + e^{-2 \log\left(\frac{1}{0.05} - 1\right) \frac{x-m}{w}}}$$

We fitted three parameters of the curve: the threshold  $m$ , width  $w$ , and the lapse rate  $\lambda$ . The lower asymptote parameter,  $\gamma$ , was fixed to 50%. Psychometric curves fit in this manner are presented as a visual aid for interpreting the data and were statistically analyzed as described in the text.

In **Fig. 6F** and **Fig. 6H**, individual points correspond to experimental conditions taken from single days and single mice; mean  $\pm$  s.e.m. are shown for each ensemble size bin (the bin width is 4 neurons). This subset of data was used to compute a two-way ANOVA to compare the effect of ensemble laminar position on classifier performance (F) or animal behavior (H). Equivalent numbers of layer 5 neurons were more successful at driving performance ( $p < 0.01$  for classifier data,  $p = 0.023$  for behavioral data, main effect of layer). Matched target and distractor ensembles differ in size by at most one neuron.

*Open source packages used:* The following open source Python libraries were used in the statistical analyses of the data presented in this paper:

IPython (69): <https://ipython.org/>

Numpy (70): <http://www.numpy.org>

Matplotlib (71): <http://www.matplotlib.org>

Psignifit 4 (68): <https://github.com/wichmann-lab/python-psignifit>

Pandas (72): <https://pandas.pydata.org/>

Scikit-learn (73): <http://scikit-learn.org/stable/index.html>

SciPy (74): <http://www.scipy.org>

Seaborn: <http://seaborn.pydata.org>

Statsmodels (75): <https://www.statsmodels.org/stable/index.html>

## Supplementary Text

### I. Structural insights into the high conductance of ChRmine

Although ChRmine was discovered through our functional metagenomic screening targeting for joint exhibition of properties required for the experiments shown here, the mechanisms underlying its unique functionality remain unclear. However, recent advances in structural understanding of channelrhodopsins (ChRs) have provided a foundation for understanding of the basis of ion selectivity and spectral sensitivity (58, 59, 76). Although ChRmine shows low similarity to previously studied ChRs, mechanistically important features, such as transmembrane domains 3,6 and 7 comprising the retinal-binding pocket and ion-conducting pathway, exhibit high sequence homology (**Fig. S1**), suggest structural explanations for the properties of ChRmine based on structural and biochemical studies of other ChRs.

In ChRmine, Asp115 (Glu162 in C1C2 and Glu129 in CrChR2), which may form a counter-ion network along with Asp253 (Asp292 in C1C2 and Asp253 in CrChR2) to the protonated retinal Schiff base, is thus one carbon shorter than its glutamate counterparts in C1C2 or CrChR2 (**Fig. S1**). This difference may slightly destabilize the hydrogen-bonding network between the protonated Schiff base and its counter-ion, which would lead to elevation of the energy of the ground state of the protein and result in less energetic, more red-shifted photons sufficing for driving the transition to the light-activated state (76). Moreover, the homology model (**Fig. S2F**, built on C1C2 crystal structure as a template) reveals that overall electrostatic surface potential of ChRmine is even more negatively charged than that of the lower-photocurrent cation-conducting channelrhodopsin C1C2, suggesting a more suitable ion-conducting pore/vestibule structure for deterring anion flux and thus allowing greater cation flux. This model would be consistent with prior findings showing how surface electrostatics determine ChR ion selectivity, and together may explain how ChRmine can give rise to higher photocurrent magnitude than other cation ChRs (58, 76). Further structural and spectroscopic studies are clearly needed to completely understand the molecular mechanisms of ChRmine.

### II. Side-by-side comparison of ChRmine and ChroME

To fully confirm the suitability of ChRmine for all-optical experiments, we directly compared the opsin with ChroME, another engineered opsin previously reported to be suitable for multiphoton optogenetics (26). We have performed *in vitro* electrophysiology of the two opsins under the same experimental conditions (intracellular solution, extracellular Tyrode, transfection period, light source). As previously reported, we observed a blue-shifted action spectrum and high photocurrents from ChroME-expressing cells (up to ~2 nA under its maximally responsive, blue-shifted light stimulation, **Fig. S3A, B**); nevertheless, significantly higher currents were observed in ChRmine cells (~4nA under red-shifted light). Most importantly, we observed high light sensitivity (100% spike probability down to 0.08 mW/mm<sup>2</sup> / 0.5 ms pulse width, **Fig. S3C, D**) in ChroME-transfected neurons, concordantly with the data previously reported, as well as neurons expressing ChRmine (26). However, as expected from the blue-shifted action spectrum, ChroME-expressing neurons failed to reliably elicit spiking in response to red-shifted light, whereas ChRmine cells could spike down to 0.08 mW/mm<sup>2</sup>. Finally, we were able to confirm that under our imaging conditions, ChroME and ChRmine drove equivalent levels of depolarization in cell culture (**Fig. S3E, F**).

In side-by-side comparison, we have shown that 1) ChroME has a more blue-shifted action spectrum than ChRmine; 2) ChroME is more sensitive to blue light (which includes the 2P

wavelength of 920nm used for imaging) relative to orange light; and 3) for both ChroME and ChRmine, the 920 nm imaging laser under 2P conditions does not elicit notable membrane depolarization (Fig. 1M, N, S3E, F). These data suggest that ChroME is suitable for all-optical experiments in which blue actuators and red sensors are required, in contrast to ChRmine, a potent red excitatory opsin suitable to be used combinatorially with blue sensors or actuators.

### III. Temporal and Spatial Multiplexing of Spatial Light Modulators (MultiSLM)

A general description of the theory and possible embodiments of this brain interface, MultiSLM, are provided here. For more details on the instantiations used in the manuscript, see **Materials and Methods**, and **Figs. 2, S4-8**. Additional instantiations are described in **Figs. S18, S19**.

MultiSLM was designed as an optical hardware solution for spatially specific >kHz targeting of any of the thousands of neurons located throughout a three-dimensional (3D) volume of tissue. While imaging neural activity (e.g., fluorescent activity reporter), simultaneous photostimulation (e.g., with optogenetics) of user-specified targets is possible—both at high spatial resolution (< 1  $\mu\text{m}$  lateral). One to hundreds of diffraction limited spots can be generated in precise locations, simultaneously (within < 1 ms), using holograms generated by combining high peak power lasers with an array of several customized, high-resolution spatial light modulators (SLMs) which are controlled by custom computational hardware and software.

In addition to enhancing the individual performance of an SLM, the MultiSLM approach presented here utilizes multiplexing of multiple optical beams (e.g. using polarization-states or chromatic-dependent optics) to gain additional utility beyond a single SLM device. Generally, laser light can originate from 1 or more lasers and be de-multiplexed into at least 2 distinct channels. The channels can be de-multiplexed using an array of strategies for beam separation across multiple channels simultaneously, or directed to different channels (SLMs) in rapid sequence, with temporal precision on the order of microseconds. A number of strategies are available to add additional SLM modules – yielding 4 or more SLMs in one system (**Figs. S18 and S19**). These channels are then multiplexed after the SLMs into a common optical axis by using dichroic mirrors, polarization beam splitters, high speed polarization switches (or electro-optic modulators) and/or 50/50 beamsplitters, which are carefully aligned with angle and polarization tuning.

When multiplexing across SLMs, two operation modes—sequential and simultaneous—can be realized and the choice of multiplexing mechanism will influence the performance of these two mode options, as discussed in more detail below. In Sequential Mode, the refresh times are staggered across individual SLMs (each with  $\sim 500$  Hz refresh rate); thus, the effective temporal resolution of distinct ensemble addressing can exceed 1 kHz. In Simultaneous Mode, multiple SLMs are simultaneously projecting to the sample, allowing more neurons to be targeted at precisely the same time (for example, over a larger volume if the SLMs are spatially tiled; **Fig. S19**). In all designs, no optical interference is expected to occur between distinct MultiSLM system optical paths since different polarizations, wavelengths and/or optical path lengths are used (and in all presented instantiations, the femto-second, pulsed stimulation laser(s) are synchronized at the source and pulsed with low duty cycle on the nanosecond scale).

Temporal precision and excitation duration (< 640 $\mu\text{s}$ ) are tightly controlled with custom software and electro-optic modulators (Pockels cells and/or polarization switches), for example, to drive a single spike in each targeted neuron using optogenetics. The SLM modulated light reflects off a set of high-speed galvanometer mirrors which move the SLM generated hologram

rapidly in the volume, for example, to create a spiral motion spanning the size of a typical neuron. This pattern could be divided into multiple “mini-spirals” to span most of the neuron cell body more rapidly, with greater efficiency. This motion moves the spot around the cell body of the neuron using empirically-derived parameters for velocity and spatial resolution to reliably yield a spike in the neuron (reaching saturating photocurrent in the best case, or at least enough photocurrent to reliably elicit a spike). It should be noted that, alternatively, a disc of light or virtually any image pattern can be created using SLM-based holography to stimulate an entire neuron cell body, or other part of a neuron, such as a dendritic spine, without the need to move the galvanometer mirrors, but with a lower light power density and thus far lower multiphoton efficiency (in standard two-photon excitation, light power density—modeled as numerical aperture of the system producing the excitation spot—is thought to influence the multiphoton effect exponentially to the fourth power (77), and is one of the single largest determinants of multiphoton excitation probability). Additionally, a grid of dots or other arbitrary pattern of light can be created to match the features (i.e., neuron cell body locations) in the volume for imaging or stimulation. In the instantiation presented in the current manuscript, the galvanometer mirrors are part of a modified two-photon microscope which has two additional sets of galvanometer mirrors, including a resonant scanner dedicated to imaging at high rates.

The wavelengths for SLM optogenetic stimulation are chosen to excite optogenetic actuators (e.g., ChRmine) at or near their peak excitation wavelengths, while minimally exciting neural activity sensors (e.g., GCaMP). This allows simultaneous opsin stimulation and neural activity imaging from the same population of neurons. Thus, the effects of stimulated patterns of activity on local dynamics can be read out in real time with neural activity imaging at single cell resolution. In low stimulation-duty cycle experiments, it may be advantageous to simply omit stimulation epochs from imaging data (as in the current manuscript), since the stimulation laser will elicit some unwanted activity sensor fluorescence. More generally, synchronizing imaging and photostimulation lasers (typically kHz-MHz repetition rates of tens to hundreds of femtosecond pulses) could permit photostimulation to occur out of phase with imaging at the level of laser pulse times (by varying optical path lengths), such that light and fluorescence artifacts caused by optogenetic photostimulation could be completely removed with a lock-in amplifier, chopper circuit operating on the MHz or GHz scale (depending on the laser source repetition rates; fluorescence decay time constants of activity reporters, such as those based on green fluorescent protein (GFP), are likely to be on the order of a few nanoseconds and thus within a fraction of the period of high repetition rate lasers, e.g., 12.5 ns for 80 MHz). Even if lasers are not synchronized with each other, high-speed electronic acquisition circuits could at least partially remove photostimulation artifacts by precisely gating acquisition on laser pulse times. Similar high-speed, laser-synchronized electronic acquisition circuits have been demonstrated previously for spatiotemporal multiplexed two-photon imaging (78). These approaches may thus have utility not only for artifact subtraction, but also for multiplexed imaging applications using MultiSLM holography for excitation of multiple points of interest at once in combination with non-scanning acquisition and computational methods that measure and estimate location information of recorded signals in 3D (53, 64, 67).

As demonstrated in this manuscript, essentially any neurons in the three-dimensional field of view accessible with a single two-photon objective are addressable to stimulate with high precision. Thus, natural patterns of activity can be precisely replayed into the population, for example, to create artificial perceptions, or to artificially reinforce learning. Furthermore, the generated pattern of activity can be altered in precise ways, or combined with other experimental



manipulations, to help understand the necessity and sufficiency of quantifiable features of the pattern on neural coding robustness, perception and behavior. In these ways, this novel device and experimental strategy may open fundamental new insights into the complexities of the brain.

*MultiSLM Sequential Mode:* The MultiSLM design allows for the overall hologram generation rate of the system to surpass the hologram generation rate of any single SLM in the system, by staggering the triggering of individual SLMs in the system, each running at maximum hologram generation rate (plus dwell time on a given hologram). The following equations describe the design and limits on the Sequential Mode of operation.

$$P_{SLM} = L + r_{SLM} + (2 * \sigma_L) + (2 * \sigma_r)$$

Where  $P_{SLM}$  is the period in time that the SLM takes to reach complete formation of a hologram (including time to load phase mask onto the SLM and time for the liquid crystal to respond and reach desired phase level to successfully generate the hologram, see **Fig. S4F**),  $r_{SLM}$  is the mean hologram generation time of the SLM from start to completion,  $L$  is the mean latency from input trigger to beginning of hologram generation by the SLM,  $\sigma_L$  is the standard deviation of latency from trigger input to the time the SLM begins transitioning to the next hologram, and  $\sigma_r$  is the standard deviation of  $r_{SLM}$ . Assuming a normal distribution of  $L$  and  $r_{SLM}$ , this achieves an estimate of  $P_{SLM}$  that is true 95% of the time.

Following from this, the hologram refresh rate of a given SLM in the system is:

$$R_{SLM} = \frac{1}{P_{SLM}}$$

The hologram refresh rate of the MultiSLM system in Sequential Mode,  $R_{seq}$ , that is the rate at which new holograms can be created, is:

$$R_{seq} = \frac{N_{SLM}}{P_{SLM} + d}$$

Where  $d$  is the duration that a formed hologram is displayed (e.g., to illuminate the sample for a desired period of time typically on the order of hundreds of microseconds), and  $N_{SLM}$  is the number of SLMs in the MultiSLM system.

So far, this assumes that  $P_{SLM}$  and  $d$  are each the same for all SLMs in the system. More generally, periods, durations, latencies and jitters can be determined for each SLM in the system and summed to determine  $R_{seq}$ :

$$R_{seq} = \sum_{i=1}^{N_{SLMs}} \frac{N_{SLM}}{P_{SLMi} + d_i}$$

The period of the MultiSLM system,  $P_{seq}$ , is:

$$P_{seq} = \frac{1}{R_{seq}}$$

The duty cycle of stimulation,  $D$ , is defined as:

$$D = \frac{d * N_{SLM}}{P_{seq}}$$

assuming equal interval in time between illumination of each SLM in the MultiSLM system. 100% duty cycle is achieved for all:

$$P_{seq} \leq d * N_{SLM}$$

The maximum hologram refresh rate of the MultiSLM system,  $MAX(R_{seq})$ , occurs with 100% duty cycle when

$$P_{seq} = d * N_{SLM}$$

and laser exposure duration times for each SLM in the MultiSLM system,  $LaserExposure_{Time}$ , are spaced sequentially in time such that:

$$LaserExposure_{Time_{i+1}} = LaserPulse_{Time_i} + \left( \frac{P_{seq}}{N_{SLM}} \right)$$

and the laser pulse duration,  $LaserExposure_{Duration}$ , equals  $d$ :

$$LaserExposure_{Duration} = d$$

and triggers to a given SLM,  $T_i$ , repeat with period  $P_{trig}$ , such that:

$$P_{trig} = P_{seq}$$

assuming that all SLMs in the system have equal  $P_{SLM}$  (otherwise, timings should account for the different periods of each SLM to achieve the same effect).  $MAX(R_{seq})$  increases as  $d$  approaches zero.

Furthermore, the improvement in hologram refresh rate of the MultiSLM compared to the hologram refresh rate of a single SLM in the system,  $R_{SLM}$ , is:

$$MAX(R_{seq}) = (R_{SLM} + d) * N_{SLM}$$

Increased temporal precision [beyond that afforded by the  $MAX(R_{seq})$  at 100% duty cycle] can be generated for all:

$$P_{seq} > d * N_{SLM}$$

leading to lower than 100% duty cycle. This also has the effect of lowering the average power delivered to the sample proportional to the reduction in duty cycle (see below). Higher temporal precision could be applied in a burst mode (that is the array of SLMs are illuminated in rapid sequence at or near 100% duty at the higher rate and overall in less time than  $P_{seq}$ , followed by a time period to allow the completion of  $P_{seq}$ ) or the higher temporal precision can be achieved while maintaining equal, sequential spacing between SLMs as described above for the 100% duty cycle implementation.

The maximum temporal precision,  $MAX(p)$ , that is the precision in stimulation time that can be guaranteed by the system, is ultimately limited by the Pockels cell response time (or more generally whatever device is used to modulate the laser beam such as electro-optic modulator, acousto-optic modulator, polarization switch, shutter, etc),  $r_{PC}$ :

$$MAX(p) = r_{PC}$$

assuming modulator driver electronics with equal or better temporal precision as  $r_{PC}$  (if this assumption is not met, then the limiting factor is driver signal sample rate). Furthermore, it is assumed that:

$$r_{PC} \ll d$$

A exposure of laser power to illuminate the hologram is calibrated in intensity depending on the hologram generated (e.g., calibrated to achieve equal hologram spot intensity regardless of imaging depth in scattering tissue), is created by a calibrated signal sent by the modulator electronics, which in conjunction with a polarizing beam splitter and beam dump, achieves the desired power level for the hologram after the light has passes through all optics and biological tissue. Additional software corrections in the hologram generation code can normalize the intensity of spots across the field of view (FOV) to account for diffraction efficiency fall off from the center of the FOV. The timing of the laser exposure for a given SLM should have duration  $d$  and be synchronized to start with the completion time of the hologram generation by an SLM, such that:

$$LaserExposure_{Time_i} = T_i + P_{SLM_i}$$

In Sequential Mode, the overall laser power stimulated at one time corresponds to the laser power of the laser exposure generated,  $LaserExposure_{Power}$ , at that time to illuminate a single hologram generated by a single SLM in the system, without overlap with illumination of other SLMs. Thus, the maximum exposure power,  $MAX(LaserExposure_{Power})$ , is limited to the maximum power allowable for any one SLM ( $SLM_{damagethresh}$ ) or hologram ( $Hologram_{thresh}$ ). The power may be further limited based on the peak power allowable into the biological tissue,  $PeakPower_{biothresh}$ , which may depend on the duration of  $d$ .

Thus:

$$LaserExposure_{Power} < SLM_{damagethresh}(d)$$

and

$$LaserExposure_{power} < Hologram_{thresh}$$

and

$$LaserExposure_{power} < PeakPower_{biothresh}(d)$$

Furthermore, an allowable average power limit may further constrain the allowable  $LaserExposure_{power}$ , for example, in the case when accumulated heating over a longer period of time must be avoided, such as over the full period of the system,  $P_{seq}$  (but other time durations can be used depending on the application). Depending on empirically determined limits of power into biological tissue, a limit may be set taking the form of:

$$\sum_{i=1}^{N_{SLM}} \frac{LaserExposure_{power_i}}{P_{seq}} * D < AveragePower_{biothresh}$$

where lower duty cycle ( $D$ ) can increase the allowable  $LaserExposure_{power}$ , up to peak power limitations.

*MultiSLM Simultaneous Mode:* In some configurations, the MultiSLM system can be run in synchronized mode, such that independent holograms generated across all of the SLMs are illuminated by laser exposures at the same time,

$$LaserExposure_{Time_i} = LaserExposure_{Time_{i+1}} = \dots = LaserExposure_{Time_{N_{SLM}}}$$

In this configuration, the damage threshold of a single SLM can be overcome by distributing more power onto more than one SLM.

$$MAX(Power_{simul}) \leq SLM_{damagethresh}(d) * N_{SLM}$$

As in the case of Sequential Mode, power limits will still remain in place regarding peak and average power into the biological tissue, and would be summed across laser power used for each SLM in the system:

$$\sum_{i=1}^{N_{SLM}} LaserExposure_{power_i} < PeakPower_{biothresh}(d)$$

$$\sum_{i=1}^{N_{SLM}} \frac{LaserExposure_{power_i}}{P_{seq}} < AveragePower_{biothresh}$$

Some sources of noise depending on the stimulation pattern (hologram) could benefit from distributing the pattern generation across multiple SLMs, instead of a single SLM. For example, complex holograms involving generation of many spots, or complex shapes may be achieved with

fewer artifacts (e.g., higher intensity spots or pattern with lower background and/or lower speckle). Since each laser source(s) can produce synchronized pulses across multiple optical paths (corresponding to each optical path in the MultiSLM system), with temporal delay lines for each path (as will occur easily given the extremely low duty cycle of the pulsed laser source and the typical length differences between optical paths on an optical table), the holograms are not generated simultaneously at the femtosecond timescale, but would be synchronized at the microsecond timescale. This design removes any chance of optical interference between the holograms generated on each SLM in the MultiSLM system.

In Simultaneous Mode, duty cycle would be lower than Sequential Mode; and depends on  $d$  and the period of the slowest SLM in the system:

$$D_{simul} = \frac{d}{MAX(P_{SLM})}$$

Since all SLMs are illuminated at the same time, the maximum period is limited by the period by the period of the slowest SLM in the system:

$$P_{simul} = MAX(P_{SLM}) + d$$

The refresh rate in Simultaneous Mode is comparable to the refresh rate of a single SLM:

$$R_{simul} \approx MAX(R_{SLM})$$

and is equal to the inverse of  $P_{simul}$ :

$$R_{simul} = \frac{1}{P_{simul}}$$

#### IV. Conceptual overview of models and simulations

In this part of the supplementary appendix, we address the theoretical implications of important puzzles raised by our data. The first puzzle is that optogenetic stimulation of a small number of neurons with similar tuning, often as little as 20, can excite a non-negligible, finite fraction of the entire population of the rest of the recorded neurons. Moreover, the threshold for external stimulation to trigger percepts that can guide behavior is equally low. These results are remarkable considering the population of similarly tuned V1 neurons to a particular oriented grating can be quite large, numbering in the several thousands. Thus these data reveal that the V1 cortical network seems to be highly excitable, with stimulation of a vanishingly small fraction of the entire network recruiting a finite fraction of the network and triggering perception. The second puzzle then is, with such a low threshold for network excitation, why don't spontaneous fluctuations in network activity elicit both false positive global network excitation events and false percepts at an appreciable rate?

In section V we quantitatively address this puzzle in a simple model of independently firing Poisson neurons. Using biologically motivated numbers for the size  $N$  of the cortical population

of similarly tuned excitatory neurons, the rate  $r$  of spontaneous firing, and typical integration time constants of cells  $\Delta$ , we show that it can in principle be possible to choose a threshold for both network excitation and perception, such that in a large population of  $O(N)$  neurons, optogenetic stimulation of only  $O(\sqrt{N})$  neurons could reliably trigger excitation of a finite fraction of the population, *without* spontaneous fluctuations triggering false positive neural or perceptual events at any appreciable rate. This analysis quantitatively explains why such a low threshold of stimulation of about 20 cells for triggering network excitation and perception is viable given biologically plausible parameters governing V1 ensemble population sizes, spontaneous activity rates, and single neuron integration time constants. However, this analysis does not provide a network mechanism that instantiates such a low threshold for network excitation.

To discover a proof of principle instantiation of such a network mechanism, we describe a simple modeling framework for a network of excitatory and inhibitory cells in section VI. Readers who are interested in the network model can skip directly to section VI. In relation to our experiment, this network is a model of the population of excitatory cells with similar tuning to a single oriented grating, also connected to a population of inhibitory cells. This model, while simple, is still rich enough to make predictions about how the fraction of active excitatory and inhibitory cells varies over time, both in the spontaneous state, and in response to optogenetic stimulation. Moreover in section VII, we analyze theoretically the properties of the fraction of active excitatory and inhibitory neurons as a function of the strength of connectivity, single neuron thresholds and nonlinearities, and properties of exogenous inputs.

While we exhibit a critically excitable model that is consistent with the remarkable finding that as few as 30 stimulated neurons can elicit large network responses, while 10 cannot, we cannot of course claim that no other qualitatively distinct models might also be consistent with the data. Such models may include for example non-mean field models with local or otherwise structured connectivity; in fact, the regime of connectivity in which our model satisfies the above criteria gives one such example of structured versus random connectivity. The main goal of our modeling was not to model the V1 recordings in detail, but rather to provide a proof of principle realization of a large neural network of  $O(N)$  neurons, in which stimulation of only  $O(\sqrt{N})$  neurons could reliably trigger excitation of a finite fraction of the population, *without* spontaneous fluctuations triggering false positive neural or perceptual events at any appreciable rate.

But regardless of the particular modeling choices we use to realize such a network, our combined theory and experiment reveals a key concept required of *all models* in order be consistent with the V1 data, namely the notion of *critical excitability*, in which the stimulation threshold for both exciting a large fraction of the network, and triggering perception, is not much higher than the size of population activity fluctuations about the spontaneous state.

## V. A simple theory of critically excitable neural dynamics in a Poisson model

Consider a population of  $N$  neurons that, in a spontaneous network state, all fire in a Poisson manner at a low spontaneous rate  $r$ . In the context of our work, this population of neurons corresponds to a selective neural ensemble of excitatory cells that are similarly tuned to the same oriented grating. Let  $n$  denote the total number of neurons that fire in the entire population within a time window  $\Delta$ . In the spontaneous state,  $n$  is then a Poisson random variable with mean  $\mu =$

$Nr\Delta$  and standard deviation  $\sigma = \sqrt{Nr\Delta}$ . For large values of  $Nr\Delta$  we can approximate  $n$  as a Gaussian random variable with the same mean and standard deviation. Now further suppose the neurons are recurrently connected in a way such that if the total number of neurons  $n$  that fire within a time window  $\Delta$ , either due to spontaneous fluctuations or due to external excitation, exceeds a threshold  $\theta$ , then the network undergoes a global excitation event in which a large fraction of the network fires. This implies that if we optogenetically stimulate a number of  $N_s$  neurons within a time window  $\Delta$ , while the network is in the spontaneous state, we will be able to trigger a network excitation event with some probability  $P(N_s)$ . This probability should become close to 1 as  $N_s$  becomes large. An interesting network property is the minimum number of neurons we need to stimulate so that we obtain a network excitation event with a high probability, for example a probability of  $P = 0.95$ . We will denote this number of neurons required to obtain an excitation event with such high probability by  $N_h$ . Our data suggests the intriguing observation that this minimal number  $N_h$  required for network excitation is much less than the total number of neurons  $N$  in the selective ensemble.

However, we also wish to ensure that the rate of spontaneous network excitation events  $r_s$  due to spontaneous activity remains low. This spontaneous rate is given by  $r_s = P(0)/\Delta$  where  $P(0)$  is the probability of global network excitation if  $N_s = 0$  cells are optogenetically stimulated. The key issue is then whether it is possible to choose biologically plausible parameters so that one can stimulate network excitation events with high probability with a very small  $N_h \ll N$ , while still ensuring the rate of spontaneous excitation events  $r_s \ll 1\text{Hz}$  remains very small. To address this issue we compute both  $r_s$  and  $N_h$  as a function of  $Nr\Delta$  and the network excitation threshold  $\theta$ . First we note that  $P(N_s)$  is simply the probability that  $n + N_s$  is greater than  $\theta$ , where  $n$  is the random number of neurons already spontaneously active during the stimulation window. Here we are assuming that the  $N_s$  neurons we are stimulating are not already spontaneously active, which is a good assumption when both  $n$  and  $N_s$  are much smaller than  $N$ . This assumption is consistent with the data and the regime in which we will eventually apply our theory. Thus  $P(N_s)$  is simply the probability that a Gaussian random variable with mean  $Nr\Delta + N_s$  and standard deviation  $\sqrt{Nr\Delta}$  exceeds the threshold  $\theta$ .  $P(N_s)$  is given by

$$P(N_s) = H\left(z_\theta - \frac{N_s}{\sqrt{Nr\Delta}}\right), \quad (1)$$

where  $z_\theta = (\theta - Nr\Delta)/\sqrt{Nr\Delta}$  is a z-scored version of the threshold for network excitation that reflects how many neurons one needs to stimulate to go from the spontaneous mean  $\mu = Nr\Delta$  to the threshold  $\theta$ , measured as a fraction of the spontaneous standard deviation  $\sigma = \sqrt{Nr\Delta}$ . Also  $H(x) = \int_x^\infty \frac{dz}{\sqrt{2\pi}} e^{-z^2/2}$  is the probability a zero mean unit variance Gaussian variable exceeds  $x$ . The function  $P(N_s)$  is a monotonically increasing function of  $N_s$ .

From this function, we can obtain  $r_s = H(z_\theta)/\Delta$ . And we obtain  $N_h$  as the solution to  $P(N_h) = 0.95$ . We denote  $x_h$  as the solution to  $H(x_h) = 0.95$ , then we obtain  $N_h = \sqrt{Nr\Delta}(z_\theta + |x_h|)$ , where the numerical value of  $x_h$  is given by  $x_h = -1.65$ . These results quantitatively capture the tradeoff induced by varying the threshold  $\theta$ . Increasing  $\theta$  also increases the z-scored threshold  $z_\theta$ , and thereby decreases the spontaneous rate  $r_s$  of excitation events, but also increases the minimum number of neurons  $N_h$  needed to reliably trigger a global network excitation event with high probability. Conversely, decreasing  $\theta$  makes the network more sensitive by reducing

$N_h$ , but also increases the rate  $r_s$  of false positive spontaneous excitation events. However, varying  $\theta$  yields dramatically different effects on  $r_s$  and  $N_h$ . In particular, increasing  $\theta$  (and therefore increasing the z-scored threshold  $z_\theta$ ) *exponentially* suppresses  $r_s$  but only leads to a modest, *linear* increase in  $N_h$ . Therefore by setting a relatively low threshold for excitation so that the z-scored threshold  $z_\theta$  is a fixed constant, *independent* of the network size  $N$  (i.e. say 5 or 10), we can make the spontaneous rate exponentially small in  $z_\theta$ , while still ensuring that the minimum number of neurons  $N_h$  needed to reliably trigger excitation remains proportional to the standard deviation of the spontaneous fluctuations, which grows only as the square-root of the tuned-ensemble size  $N$ . In essence this corresponds to a situation in which the network ensemble has a low excitation threshold that lies just above what spontaneous fluctuations could reliably reach. However, the threshold is not so high that a small number of  $O(\sqrt{N})$  additional stimulated neurons, of size proportional to the  $O(\sqrt{N})$  size of these same spontaneous fluctuations, cannot push the network over the threshold for a global excitation event.

We can now employ biologically plausible numbers to test this simple framework. A reasonable estimate for the tuned-ensemble size is given by  $N$  of order of magnitude in the thousands. For simplicity we take  $N = 5000$ . Previous studies of spontaneous activity in mouse primary visual cortex suggest a low spontaneous rate of  $r = 0.2\text{Hz}$ . We consider a time window of  $\Delta = 20\text{ms}$ , proportional to the typical membrane time constant over which neurons can integrate spikes. This yields a total population mean spike count of  $\mu = Nr\Delta = 20$  and spontaneous fluctuations of standard deviation  $\sigma = \sqrt{Nr\Delta} = 4.47$ . Now suppose we set a threshold  $\theta$  corresponding to a z-scored threshold  $z_\theta = 5$ . Then  $r_s = H(z_\theta)/\Delta = 1.43 \times 10^{-5}\text{Hz}$ . With this small rate of spontaneous events, we would observe on average 1 spontaneous network excitation event, or false positive percept, every 19 hours. However, we could still reliably trigger an global network excitation event by optogenetically stimulating only  $N_h = \sqrt{Nr\Delta}(z_\theta + |x_h|) = 4.47 \times (5 + 1.65) = 30$  neurons, which is much less than the ensemble size of  $N = 5000$ , and similar to what we observe in our data. Thus overall, this analysis provides a simple and quantitative framework for thinking about low thresholds for global network excitation or perception can be. Furthermore, when combined with our experiments, this framework suggests that V1 may have organized its internal connectivity and thresholds so as to be highly sensitive to the simultaneous excitation of exceedingly small numbers selectively tuned neurons, without suffering from unreasonable rates of false positive spontaneous network excitation events.

## VI. A Model of a critically excitable recurrent network

While the above considerations of spontaneous activity suggest thresholds for external stimulation to trigger global network excitation or percepts could be as low as of  $O(\sqrt{N})$ , it does not exhibit any neural network capable of achieving this lower bound. Here, we provide, as a proof of principle, one network that can do so. The key idea behind our network model is to employ a highly excitable excitatory subnetwork that can itself be bistable, with both a low and a high activity state. However, we connect it to an inhibitory network with delayed inhibition, though other undiscovered mechanisms might suffice. This sets up an excitable network dynamics in which optogenetic stimulation of a subset of excitatory cells can yield the activation of a large fraction of the excitatory subnetwork, before the slow inhibition is engaged and brings this activity back down. The challenge in the network, as explained in the previous section, is to tune the



recurrent excitatory and inhibitory connectivity strength so that small optogenetic perturbations would elicit a strong circuit-wide response, while the fluctuations of spontaneous state due to spontaneous external inputs would not de-stabilize the spontaneous resting state. In the following section below, we will explain in more detail how we can analytically derive recurrent excitatory and inhibitory weights to satisfy these objectives. In this section, we simply present the resultant network, so the reader can understand the model without having to read the theory behind its derivation.

We consider a simple, standard neural network model of firing-rate neurons previously used in many scenarios to analyze neural circuit dynamics (79). We assume two populations of such neurons (**Fig. S17A**): one population of  $N$  excitatory neurons (denoted by  $E$ ) and one population of  $N$  inhibitory neurons (denoted  $I$ ). For simplicity, we employ the same population size  $N$  for both the  $E$  and  $I$  populations, as we can trade off population size with strength of connectivity without significantly affecting the final conclusions derived from our model. The excitatory population can be thought of as a single population of V1 excitatory cells all with similar preferred tuning to a particular orientation.

In our model, the instantaneous output firing activity  $s_i^A(t)$  at time  $t$  of each neuron  $i = 1, \dots, N$  in population  $A$  (where  $A \in \{E, I\}$ ) is given by

$$s_i^A(t) = \phi(x_i^A(t) - T^A). \quad (2)$$

Here,  $x_i^A(t)$  is the input to each neuron,  $T^A$  is the firing threshold for neurons in population  $A$ , and  $\phi$  is a nonnegative sigmoidal transfer function that approximates the relation between the input and the output firing rate of the neuron. In particular  $\phi(x)$  increases monotonically from 0 for large negative  $x$  and rises to 1 for large positive  $x$  taking the intermediate value  $\phi(x) = 1/2$  for  $x = 0$ . Thus if the internal input  $x_i^A(t)$  is far above the threshold  $T^A$ , then the neuron is active with  $s_i^A(t)$  close to 1. A temporal average of  $s_i^A(t)$  then yields the neuron's firing rate. While our conclusions hold for general sigmoidal input-output nonlinearities, we run our simulations with the particular form  $\phi(x) = e^{gx}/(1 + e^{gx})$ , where  $g$  is the gain of non linearity.

In turn, in our model, the input  $x_i^A(t)$  to each neuron is obtained by a leaky integration of activity via

$$\tau_A \frac{d}{dt} x_i^A(t) = -x_i^A(t) + u_i^A(t) + \xi_i^A(t), \quad (3)$$

where  $\tau_A$  is the integration time constant of neurons in population  $A$ ,  $u_i^A(t)$  is the total summed activity of sources both internal and external to the network, and  $\xi_i^A$  is a potential source of stochastic noise, which may itself be internal to each neuron or originate from external inputs to the network. We assume the mean of  $\xi_i^A(t)$  is zero and its variance is  $\sigma_0^2$ . The total summed activity  $u_i^A(t)$  is given by

$$u_i^A(t) = \sum_j W_{ij}^{AE} s_j^E(t) - \sum_j W_{ij}^{AI} s_j^I(t) + I^A(t). \quad (4)$$

It consists of three components: (1) a contribution from the excitatory population activity  $s_j^E(t)$  weighted by a synaptic connectivity matrix  $W_{ij}^{AE}$  from neuron  $j$  in the  $E$  population to neuron  $i$  in the  $A$  population, (2) a contribution from the inhibitory population activity  $s_j^I(t)$  weighted by a synaptic connectivity matrix  $W_{ij}^{AI}$  from neuron  $j$  in the  $I$  population to neuron  $i$  in the  $A$  population, and (3) an external input  $I^A$  that is broadcast to all neurons in population  $A$ . Loosely speaking, one could think of the different terms in (4) as different synaptic input currents, and the leaky integration in (3) as corresponding to the passive integration of these synaptic inputs by a membrane potential like variable  $x_i^A(t)$ , so  $\tau_A$  would roughly correspond to the membrane time constant.

We next consider an ensemble of network connectivities that are chosen randomly according to the probabilistic rule

$$W_{ij}^{AB} = \frac{1}{pN} w^{AB} \times \begin{cases} 1 & \text{with probability } p, \\ 0 & \text{otherwise} \end{cases}, \quad (5)$$

where  $w^{AB}$  are all positive  $O(1)$  numbers. In principle the connection probability  $p$  could depend on  $A$  and  $B$ . Without loss of generality, we take the connection probability to be uniform between pairs of populations, as changes in connection probability between population pairs can be traded off against changes in the strength of nonzero connectivity  $w^{AB}$  between population pairs  $A$  and  $B$ , without altering the main conclusions of our analysis. In this model, each active presynaptic neuron contributes  $\sim \frac{1}{pN}$  to the postsynaptic neuron's input, and there are  $pN$  neurons from each population projecting to each neuron on average, yielding a total mean  $O(1)$  input current with a magnitude similar to the threshold. Fluctuations due to heterogeneous activity across presynaptic neurons contribute only term of order  $1/\sqrt{N}$ . Thus, this network operates in a mean driven regime, with fluctuations originating from the external noise term  $\xi(t)$ .

For our simulations, we have chosen a set of parameters  $w^{AB}, \sigma_0$  so that the system is in a state of critical excitability. Here, the net excitatory synapses are not too strong, and random fluctuations due to the noise  $\sigma_0$  are not amplified through the positive feedback in the network, yielding a stable low activity spontaneous state. However, the feedback is finely tuned so that a small amount of excitation on top of the spontaneous activity results in a strong positive feedback that de-stabilizes the spontaneous state and initiates a global network excitation event amongst the fast excitatory cells. The slower inhibitory population follows the excitatory one, and eventually shuts it off, generating a transient network excitation. The difference in the inhibitory and excitatory time constants, and the relative strengths of the inhibitory and excitatory synapses, combine to determine the height and duration of the excitatory peak (here slower and weaker inhibitory feedback leads to a stronger and more long-lasting excitatory response). The amount of noise  $\sigma_0$  is chosen so that the network's spontaneous activity is similar in magnitude to that observed in the spontaneous activity of V1 in awake mice. The rest of the parameters are tuned to achieve critical excitability as explained above. A detailed theoretical analysis of this dynamics, and of how parameters can be chosen, is given in the following section. Simulation results are presented in **Fig. S17B,C**, which contains full numerical values for the simulation parameters.

## VII. Self-consistent mean field analysis of the population dynamics

In the following theoretical analysis of the network model defined in the previous section, we consider a simpler form of the activation function, for which neurons are either active, or silent, depending on their synaptic input.

$$\phi(x) = \begin{cases} 1 & x \geq 0 \\ 0 & x < 0 \end{cases} \quad (6)$$

This function can be considered as a high gain, or large  $g$  approximation of the sigmoid activation function  $\phi(x) = e^{gx}/(1 + e^{gx})$  (**Fig. S17D**). Nevertheless, all the qualitative results of our analysis hold for this more general activation. Moreover, the gain  $g$  of the sigmoid can be traded off against the strength  $w^{AB}$  of the synaptic weights, to achieve similar network behaviors.

In the limit of large  $N$ , statistical properties of the neural population dynamics in equations (2), (3), and (4), converge to deterministic mean quantities that do not depend on the detailed realization of the random connectivity in (5). Mean field theory can then be used to analytically compute these statistical properties. Two such key properties are the population average activity of each population  $A$  in the network, given by

$$\frac{1}{N} \sum_{i=1}^N s_i^A(t) = m^A. \quad (7)$$

and the heterogeneity, or variance of the population activity around its mean, given by

$$\frac{1}{N} \sum_{i=1}^N (s_i^A(t) - m^A)^2 = m^A(1 - m^A). \quad (8)$$

Because we are focusing our theory on the Heaviside nonlinearity in (6), in which each neuron is either active (with  $s_i^A(t) = 1$ ) or inactive (with  $s_i^A(t) = 0$ ),  $m^A$  is between 0 and 1 and can be thought of as the fraction of active neurons in the population at an instant of time. Similarly, the variance in (8) can be thought of as the variance of a 0 – 1 Bernoulli variable with a probability  $m^A$  of being active.

Over time, the network dynamics will settle into a stationary state in which the fraction of active neurons  $m^A$  will become independent of time (up to fluctuations that are of order  $1/\sqrt{N}$ ). This constant value of  $m^A$  can be computed in mean field theory by demanding a simple self consistency condition: the statistics of the inputs across neurons must be consistent with the statistics of the output  $m^A$ . However, since the inputs to each neuron are in turn generated by the outputs of the neural population, the input statistics are also a function of  $m^A$ . Thus demanding self-consistency of the statistics of inputs and outputs of the neural population yields an implicit equation whose solution enables us to determine  $m^A$  and its dependence on all parameters.

To obtain this self consistent equation, we first compute the statistics of the inputs  $u_i^A$  across neurons  $i$  in each population  $A$ . The population mean of the synaptic input currents  $u_i^A$  can be computed by averaging (4) across neurons, yielding

$$\frac{1}{N} \sum_{i=1}^N u_i^A \equiv u_A = pN(w^{AE}m^E - w^{AI}m^I + w^{A0}m^0) = \frac{1}{N} \sum_{i=1}^N x_i^A. \quad (9)$$

Moreover, in a stationary state, the population mean of the synaptic currents  $u_i^A$  equals the population mean of the membrane voltages  $x_i^A$  (up to fluctuations that are  $O(1/\sqrt{N})$ ) because we are assuming the noise  $\xi_i^A$  in (3) is zero mean. Also, we have parameterized the external input  $I^A$  as

$$I^A = w^{A0} m^0. \quad (10)$$

We can think of  $m^0$  as the fraction of active neurons in an outside population, distinct from either the  $E$  or  $I$  populations, and this external population provides inputs to each population  $A \in \{E, I\}$  through mean synaptic connectivity parameter  $w^{A0}$ .

Now the actual membrane potential of each individual neuron  $x_i^A(t)$  will vary across neurons  $i$  at any instant of time  $t$ . The heterogeneity, or variance, in membrane potentials about the population mean  $u_A$  is due to the noise,  $\xi_i^A(t)$  in (4), and is given by

$$\sigma_A^2 = \frac{1}{N} \sum_{i=1}^N (x_i^A - u_A)^2 = \sigma_0^2 + O\left(\frac{1}{N}\right), \quad (11)$$

Where the extra terms of  $O\left(\frac{1}{N}\right)$  are due to the variance in the recurrent input from the network.

Now equations (9) and (11) describe how the mean  $u_A$  and variance  $\sigma_A^2$ , respectively, of the distribution of membrane voltages  $x_i^A$  across neurons  $i$  in population  $A$ , depend on the fraction of active neurons  $m^E$  and  $m^I$  in the  $E$  and  $I$  populations. However, these fractions are in turn determined by the distribution of membrane voltages  $x_i^A$  across neurons  $i$ , through the single neuron nonlinear input-output map in (6). Thus self-consistency imposes additional relations between the fraction of active neurons  $m^A$  and membrane potential statistics  $u_A$  and  $\sigma_A^2$  given by

$$m^A = \frac{1}{N} \sum_{i=1}^N s_i^A(t) = \frac{1}{N} \sum_{i=1}^N \phi(x_i^A(t) - T^A). = \int dx \mathcal{N}(x; u_A, \sigma_A^2) \phi(x - T^A), \quad (12)$$

where  $\mathcal{N}(x; \mu, \sigma^2) = \exp(-\frac{1}{2}(x - \mu)^2/2\sigma^2)/\sqrt{2\pi\sigma^2}$  is the normal distribution with mean  $\mu$  and variance  $\sigma^2$ . In the last step in (12) we have replaced the sum over neurons with an integral over a Gaussian distribution of membrane voltages with the appropriate mean and variance. This Gaussian distribution is justified by central limit arguments, under the assumption that each neuron receives many weakly correlated inputs. A graphic representation of how the distribution of membrane voltages and the single neuron nonlinearity conspire in (12) to generate the fraction of active neurons is shown in **Fig. S17D**.

For the step function  $\phi(x)$  in (6) we can easily perform the integral on the RHS to get

$$m^A = H\left(\frac{T^A - u^A}{\sigma_0}\right), \quad (13)$$

where

$$H(x) = \frac{1}{\sqrt{2\pi}} \int_x^\infty dz e^{-z^2/2} = \frac{1}{2} \operatorname{erfc}(x/\sqrt{2}). \quad (14)$$

Since mean  $u_A$  and variance  $\sigma_0^2$  of the distribution of membrane voltages are themselves functions of  $m^E$  and  $m^I$ , through (9) and (11), (13) yields a pair of self-consistent equations for  $m^E$  and  $m^I$  which determine the fraction of active neurons in each population in a stationary state. We next examine solutions to these equations.

The motif of strong excitatory positive feedback stabilized by delayed inhibition yields a threshold like behavior in which stimulation of a small number of cells above threshold yields a large response. A key issue then is, the threshold must be low enough so that the requisite number of stimulated cells to yield a large network response is small, as seen in the data, but not so small so that spontaneous fluctuations can reliably trigger global, false positive network excitation events at appreciable rates. We now examine conditions under which we can generate such a tuned, sensitive threshold by tuning network connectivity.

To allow a strong excitatory response, we assume that the membrane potential of the excitatory neurons is faster than the inhibitory neurons,  $\tau_E < \tau_I$ . To simplify the theoretical analysis, we will work in the limit where  $\tau_E \ll \tau_I$ . In this limit we can decouple the dynamics of the inhibitory and the excitatory populations. Furthermore, the full dynamics of the system is well described by the nullclines, where the time derivatives of either the mean excitatory or inhibitory activities are zero. We first analyze the excitatory subnetwork at fixed mean external inhibition. The mean activity of the excitatory population in a stationary state at a fixed mean inhibitory synaptic current  $I$  is obtained by inserting the above choices into (13):

$$m^E = H\left(\frac{T^E + I - w^{EE}m^E}{\sigma_0}\right), \quad (15)$$

The stationary mean firing rates of the excitatory population  $m^E$  are given by the solutions of (15), and depend on the amount of inhibition  $I$  received from the inhibitory population. The graphical solutions of (15), for various values of  $I$  are depicted in **Fig. S17E**. Interestingly, for a fixed threshold  $T^E$ , as  $I$  varies, the system goes through two dynamical bifurcations. At low values of  $I$  there is a single stationary state with  $m^E \approx 1$ . This corresponds to a situation in which the weak inhibitory input  $I$  is unable to balance the strong recurrent excitation, which then drives a large fraction of the network into a high activity state.

As  $I$  increases, at some point  $I = I'$ , there is a saddle-node bifurcation, where two new stationary solutions (in addition to the stable high activity stationary solution) appear at some low value of  $m^E$ . One of these new solutions is stable, and the other unstable. As  $I$  further increases, the two new solutions drift apart: the stable one approaches zero, and the unstable one approaches the high activity stable point. This intermediate range of inhibition corresponds to an excitatory subnetwork that is *bistable*, with two possible activity states. Which one gets chosen depends on the initial fraction  $m^E$  of active neurons. If this fraction is below (above) the level of the single unstable fixed point, this fraction will be driven to that of the low (high) activity stable state. The distance between the low activity fixed point and the unstable fixed point then constitutes a type of excitability threshold. In essence it determines how many excess neurons must fire to push the network out of its low activity state and into its high activity state.

At some point  $I = I'' > I'$ , a reverse saddle-node bifurcation takes place, and the low-activity stationary solution becomes the only stable solution. This corresponds to a situation in which the inhibition  $I$  is so strong that the excitatory subnetwork cannot stably maintain any high activity state.

While the above analysis of the excitatory subnetwork was predicated upon the assumption that the inhibitory subnetwork had a fixed constant level of population activity  $m^I$ , thereby providing a fixed mean inhibitory current  $I$  to all neurons in the excitatory subnetwork, in reality the fraction of active excitatory ( $m^E$ ) and inhibitory ( $m^I$ ) cells can jointly co-vary. We can use this degree of freedom to choose all the connectivity parameters within and between the  $E$  and  $I$  populations so that the joint mean field fixed point  $(m^E, m^I)$  yields a particular synaptic current input  $I$  onto the excitatory subnetwork. We can tune connectivity parameters so that this net inhibition  $I$  is just above the first bifurcation point  $I'$ , so that the low activity state and the unstable fixed point in  $m^E$  are close to each other. This corresponds to a low threshold for excess excitation in the excitatory subnetwork to run-away to the high activity state, only to be brought back down when the delayed inhibition is engaged. However, we must still tune connectivity parameters so that  $I$  is sufficiently above  $I'$  that spontaneous fluctuations do not cause this transient runaway of the excitatory subnetwork.

More quantitatively, the inhibitory population will flow toward the stable stationary states given by the solutions of

$$m^I = H\left(\frac{T^I + w^{II}m^I - w^{EI}m_*^E}{\sigma_0}\right), \quad (16)$$

where  $m_*^E$  is one of the stable stationary solutions for the excitatory population in (15) with the relation between  $m^I$  and  $I$  given by the inhibitory component of the synaptic current in (9). We note that the model does not require recurrent inhibitory connections, and we can set  $w^{II} = 0$  or any number. A schematic illustration of the dynamical landscape set by the two nullclines associated with the joint equations (15) and (16) is depicted in **Fig. S17F**.

Note, that in order for the network to exhibit critical excitatory behavior, with slow relaxation back to resting state, the synaptic weights must obey some relations. In particular, there are two conditions that must be met. The first requirement corresponds to an inequality that ensures that the inhibitory synaptic current onto the excitatory subnetwork is strong enough to bring the excitatory subnetwork back to the low activity state if it starts in the high activity state. This requirement can be written as

$$w^{EI}m_*^I > I'', \quad (17)$$

where  $m_*^I$  is the high activity stable solution to (16). The value  $I''$  is itself a function of  $w^{EE}$  and  $\sigma_0$ . This is a weak constraint, and does not require fine tuning of the synaptic weights.

The second requirement is a tight requirement related to the fine tuning of the threshold for excitability. It requires that at the stationary state we have

$$w^{EI}m_*^I = I' + \epsilon, \quad (18)$$

where  $I'$  depends on  $w^{EE}$  and  $\sigma_0$ , and  $\epsilon \ll 1$  has the same units as the threshold. The smaller  $\epsilon$  is, the smaller the stability region of the low activity stable state, and the smaller the number of excess excitatory neurons needed to elicit a global network response. However, if it is set too small, then the network will suffer from high rate of spontaneous false positive excitation events.

Now, given that fluctuations in the spontaneous mean activity  $m^E$  are as small as  $O(1/\sqrt{N})$ , we can set  $\epsilon$  to be as small as  $O(1/\sqrt{N})$  without triggering an appreciable rate of false positive global network excitation driven by spontaneous activity. This in turn implies that the distance from the low activity stable fixed point to the unstable fixed point, in the excitatory subnetwork, measured in terms of fraction of active neurons is  $O(1/\sqrt{N})$ . This small distance means that, in terms of the total number of neurons, if  $O(\sqrt{N})$  of them have excess excitation, for example due to direct optogenetic stimulation, this tiny subpopulation, which is a vanishing fraction of the total population size  $N$  as  $N$  gets large, can elicit a large network response in which a *finite* fraction of neurons fire.

Thus this finely-tuned critically excitable model provides a proof of principle realization of a neural network that can be highly sensitive to external inputs (achieving the lower bound of sensitivity to stimulation of only  $O(\sqrt{N})$  neurons, as laid out in Sec. VI. ), while still maintaining low levels of spontaneous activity without appreciable false positive global network excitation events.





**Fig. S1. Structure-based sequence alignment of natural channelrhodopsin genes.** The sequences are ChRmine (GenBank ID: TBD), *Gt*ACR1 (GenBank ID: AKN63094.1), *Gt*ACR2 (AKN63095.1), *Cr*ChR1 (GenBank ID: 15811379), *Cr*ChR2 (GenBank ID: 158280944), VChR1 (UniProtKB ID: B4Y103), and Chrimson (Genbank ID: AHH02126.1). The sequence alignment was created using PROMALS3D and ESPript3, followed by manual re-alignment of TM1s, which were apparently misaligned. Predicted transmembrane domains are shown as coils. Structurally important residues are highlighted with red boxes and white font color, with other residues showing high sequence homology highlighted with blue boxes and red font color.

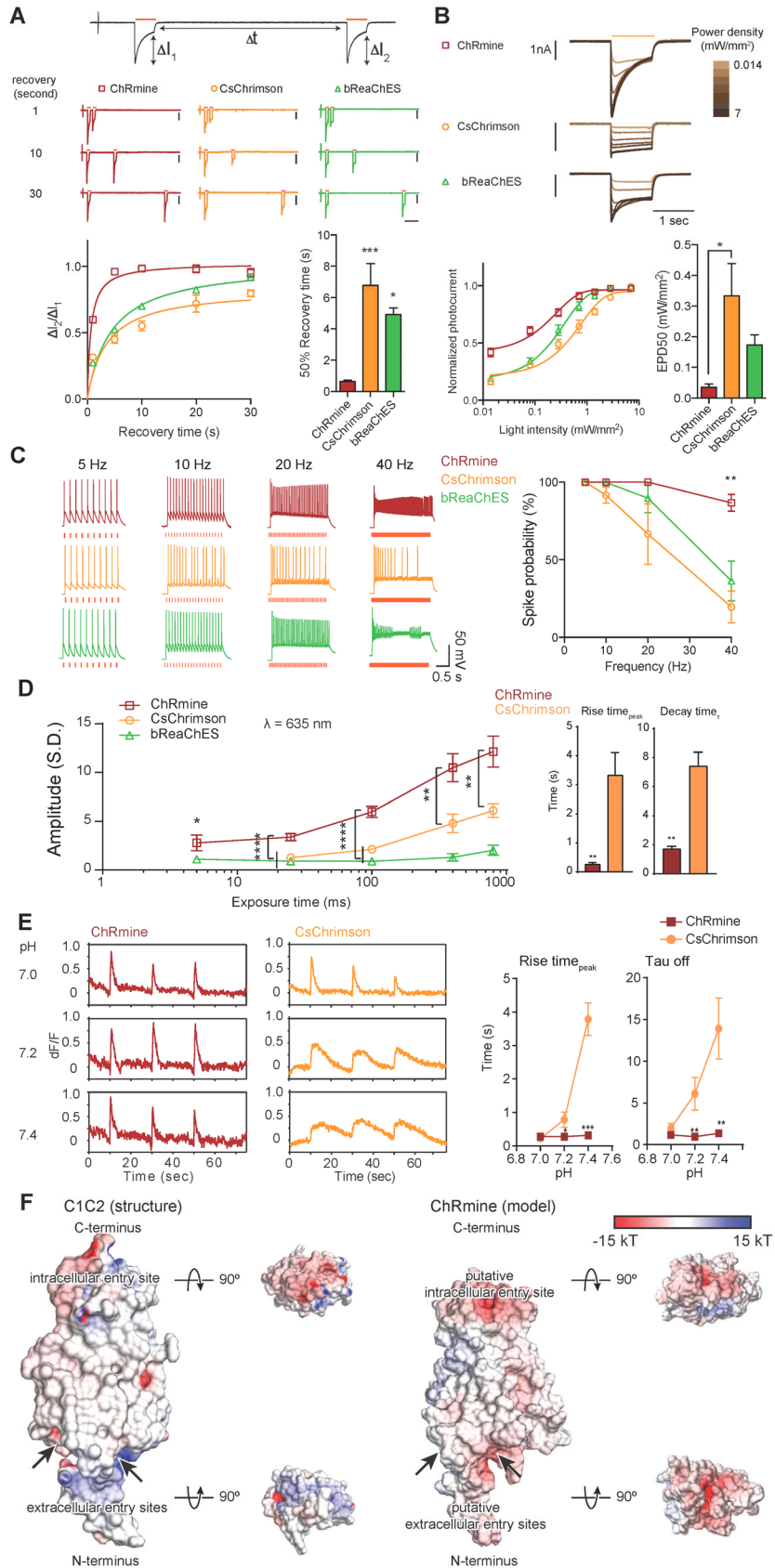


**Fig. S2. Electrophysiological and structural characterization of ChRmine.** (A) Top - example traces showing channelrhodopsin recovery from desensitization after 1 s, 10 s and 30 s dark recovery times. Peak photocurrent magnitudes before ( $\Delta I_1, I_{\text{peak}1} - I_{\text{stationary}1}$ ) and after ( $\Delta I_2, I_{\text{peak}2} - I_{\text{stationary}2}$ ) the recovery time interval ( $\Delta t$ ), and 1 second of light illumination periods (585 nm, 0.7 mW/mm<sup>2</sup>, orange lines) are shown in the scheme. Bottom - time-dependent recovery plotted against the recovery time interval (left). Note that 50% recovery time constant of ChRmine was significantly faster than that of CsChrimson or bReaChES. (right). (means  $\pm$  s.e.m. n = 5 – 6 cells. \* p < 0.05, \*\*\* p < 0.001 in one-way ANOVA with Dunnett's test). Vertical scale bars = 1 nA current amplitude, horizontal scale bar = 1 second. (B) Top - examples traces showing channelrhodopsin photocurrents across different light intensities. Photocurrents were measured with 585 nm, 1 sec light stimulation at power densities of (in mW/mm<sup>2</sup>) 0.014, 0.08, 0.28, 0.7, 1.4, 2.8 and 7. Bottom - normalized photocurrents plotted against the light intensities (left). Note that Effective Power Density for 50% maximal photocurrent (EPD50) for ChRmine is significantly lower than that of CsChrimson (means  $\pm$  s.e.m. n = 5 – 6 cells. \* p < 0.05 in one-way ANOVA with Dunnett's test). (C) Red-shifted channelrhodopsin spike fidelity. All spiking protocols used a train for 2 seconds and 0.7 mW/mm<sup>2</sup> light power was used for illumination. For light width, 1 ms for ChRmine and 5 ms for bReaChES and CsChrimson were used, as determined from the light sensitivity measurement from **Fig. 1**. (means  $\pm$  s.e.m. n = 5 -7 cells, \*\* p < 0.01 in one-way ANOVA with Tukey's test). (D) Left - Trial-averaged Ca<sup>2+</sup> response peak amplitude to ChRmine (red), CsChrimson (orange) and bReaChES (green) after pulses of 2, 5, 25, 100, 400, or 800 ms in response to 635 nm light. Right – Summary of rise and decay kinetics of Ca<sup>2+</sup> transients in response to 635 nm, 800 ms light pulses. bReaChES data not plotted in kinetics since the amplitude is too small for precise analysis (mean  $\pm$  s.e.m, n = 5-7 cells, \*\* p < 0.01, \*\*\* p < 0.001; one-way ANOVA with Tukey correction). (E) Left- representative Ca<sup>2+</sup> imaging traces response to indicated pH<sub>ext</sub> (7.0, 7.2, 7.4) at 585 nm light pulse, under the same experimental setup as indicated in (**Fig. 1H**). Right - trial-averaged Ca<sup>2+</sup> response kinetics to ChRmine (red) and CsChrimson (orange) at indicated pHs (mean  $\pm$  s.e.m of n = 5-7 cells. \* p < 0.05, \*\* p < 0.01, \*\*\* p < 0.001 in two-tailed t-test). (F) Surface electrostatic potentials of the crystal structure of C1C2 (left) and homology model of ChRmine (right), built using RosettaCM (80), with C1C2 structure as a template. The surface is colored on the basis of electrostatic potential contoured from -15 kT (red) to +15 kT (blue). White denotes 0 kT. Surface potential was calculated using PDB2PQR (81) for both *GtACR1* and C1C2 models. Note that homology model-based comparison indicates more electronegative surface potential of ChRmine than that of C1C2.

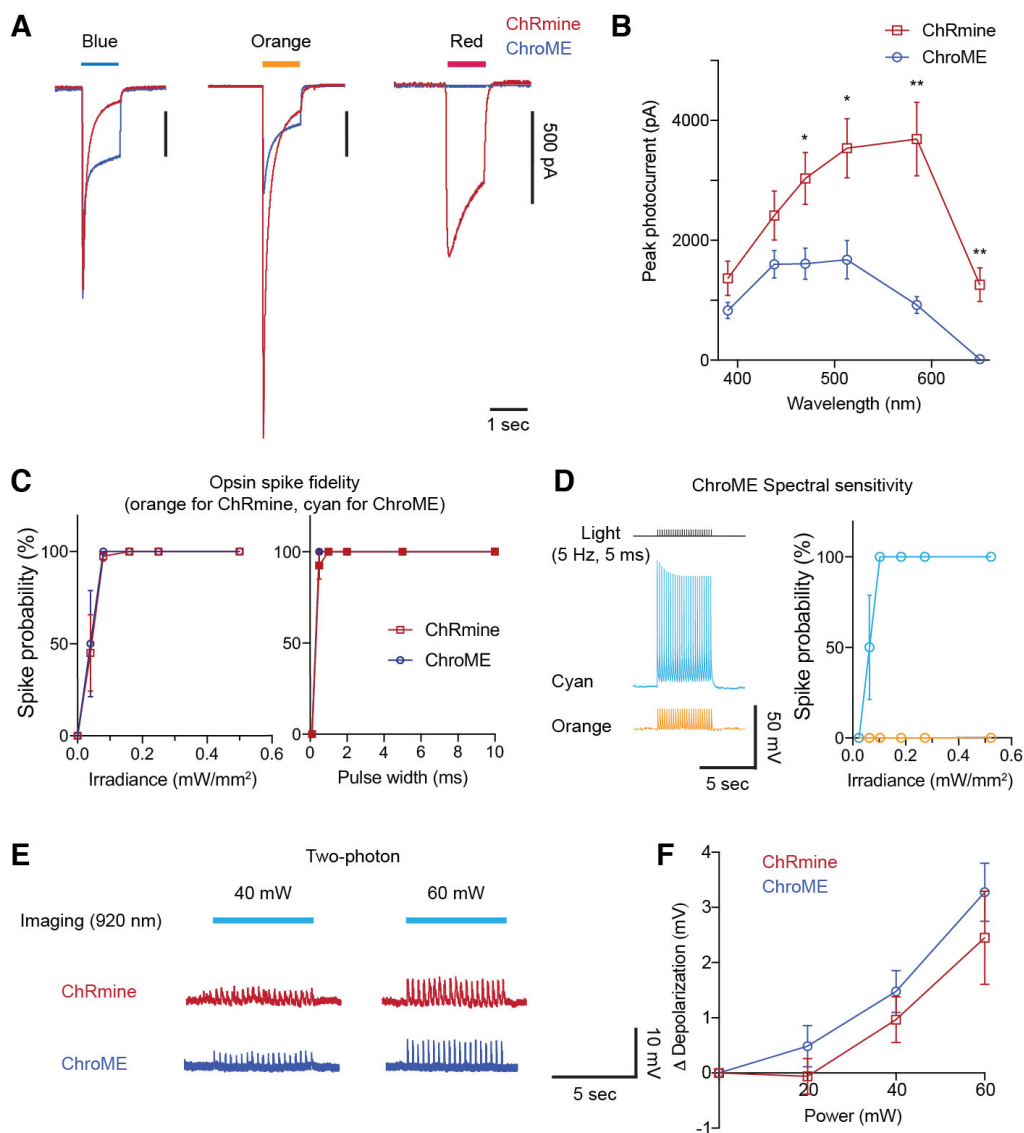


**Figure S3. Comparison of ChRmine and ChroME under identical experimental conditions.**

(A) Representative voltage-clamp traces of ChRmine and ChroME-expressing neurons responding to 1 s blue (438 nm, 0.5 mW/mm<sup>2</sup>), orange (585 nm, 0.5 mW/mm<sup>2</sup>) and red light (650 nm, 0.5 mW/mm<sup>2</sup>). (B) Action spectra of ChRmine and ChroME in cultured neurons using peak currents after 1 s stim (0.5 mW/mm<sup>2</sup>) (mean ± s.e.m. n = 6 cells, \* p < 0.05, \*\* p < 0.01, two-tailed t-test). (C) Left - probability of evoking spikes at different intensities of light at 5 Hz for 2 s, pulse width 5 ms. Right - probability of evoking spikes for different light pulse widths delivered at 5 Hz for 2 s and 0.5 mW/mm<sup>2</sup>. (mean ± s.e.m. n = 4 cells). (D) Left - current-clamp traces; ChroME reliably induced spikes with cyan light (470 nm, 5 ms pulse width, 5 Hz pulses) but not with orange light (585 nm, 5 ms, pulse width, 5 Hz pulses). Right - summary of ChroME spike fidelity in response to orange or blue light (mean ± s.e.m., n = 4 cells). (E) Voltage clamp traces during 40 mW and 60 mW imaging exposure (right) ( $\lambda = 920$  nm, 2.8 Hz frame-rate). (F) Summary of experiments in (E) (mean ± s.e.m. n = 5 cells for ChroME and 4 for ChRmine). Note that depolarizations in ChroME and ChRmine are not significantly different across all powers (two-tailed t-test, p = 0.757).

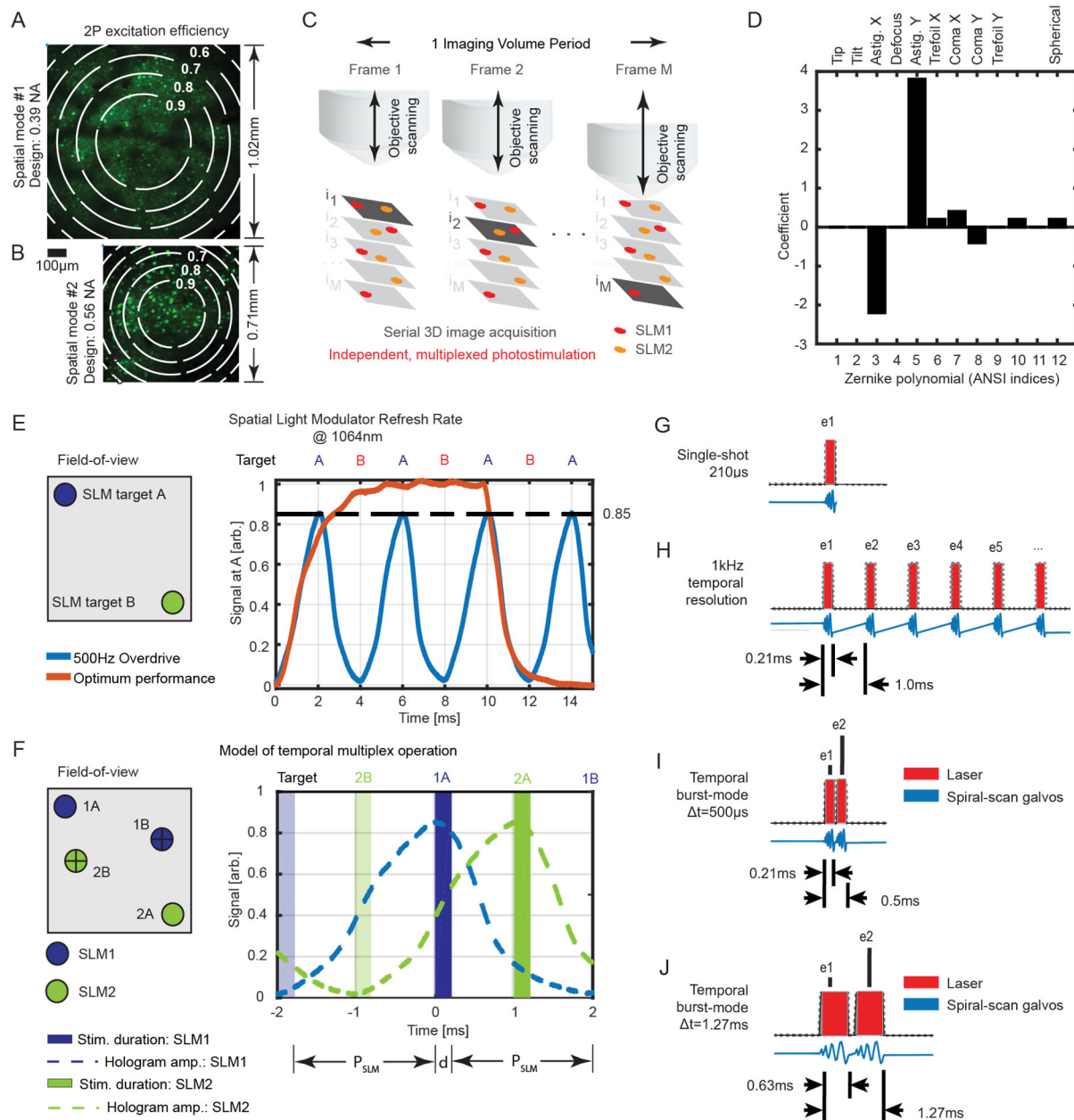


**Fig. S4. Theoretical and operational properties of the microscope.** (A) Theoretical multiphoton excitation efficiency curves for two alternative microscope objectives. The Olympus 10x/0.6NA multiphoton objective affords a large transverse field-of-view (1.02 mm x 1.02 mm) at a theoretically lower excitation NA (0.39). White contour lines document the graded multi-photon excitation efficiency as a function of field position. (B) The Nikon 16x/0.8NA multiphoton objective compromises on the transverse field size (0.71mm x 0.71mm) in order to realize a more precise theoretical point spread function (PSF) (NA = 0.56) (bottom). (C) 3D imaging with optogenetic photoexcitation is realized by use of a piezo-coupled microscope objective for imaging while the SLM volumetrically addresses cells for optogenetic stimulation. During each frame

acquisition (frames 1 to M), all SLMs are able to volumetrically address the sample across N axial image planes ( $i_1$  to  $i_N$ ). Because of the piezo movement, the constellation of optogenetic targets will be axially offset during each frame acquisition, requiring a compensating quadratic phase offset to the SLM phase masks for each axial position. **(D)** Representative adaptive optical correction to the SLM/optogenetic stimulation path as represented by Zernike polynomials. Application of the superposition of these polynomials as a compensatory phase mask results in the optimization of the optical PSF. The most significant aberrations are associated with astigmatism and possibly compensating for deformations across the face of the large-format SLMs (66). **(E)** The maximum refresh rate of the large-format SLM is benchmarked at optimum diffraction efficiency (and slow refresh rate) (red) in comparison to the operation using software overdrive at 500Hz (blue) by placing a photodiode at the target A position. Alternating between holograms which alternatively place a spot at position A and alternative positions (e.g. position B) reveals that 85% of the optimum performance can be realized at a 500Hz switching rate. Note the measurement is at  $\lambda=1064\text{nm}$ , in the wavelength range where we plan to operate, since LC response is often more than 3x faster at visible wavelengths (82). **(F)** A diagrammatic description of the temporal interleaving sequence using multiple SLMs. As each target/group hologram is exposed (e.g. solid bar SLM1 / target 1A @  $t = 0\text{ms}$ ), the alternate SLM is already constructing the next hologram (e.g. dashed-line SLM2 / target 2A @  $t = 0\text{ms}$ ). The maximum temporal resolution of a single SLM is limited by the sum of the SLM rise time ( $P_{\text{SLM}}$ ) and optogenetic exposure time (d). **(G)** The MultiSLM with ChRmine technology allows significantly faster ensemble stimulation paradigms than previous studies. For example, a single hologram must be maintained for 5 ms duration to drive a spike in (26). We report exposures driving spikes in cell ensembles (i.e. e1) at 0.21ms durations with spiral-scanning galvos across the cell membrane. **(H)** Exploiting the fast optogenetic exposure and SLM dynamics, as well as temporal interleaving of multiple SLMs, results in a lower practical limit of 1.79ms rise times and 0.21ms exposures for a 1 kHz temporal resolution spike train for neuron ensembles e1 - eN. **(I)** For a multiple SLM system, the system may run in a burst-mode where the interval between two successive ensembles, addressed by SLM1 and SLM2 respectively, can be continuously variable, down to the switching time of the Pockels cell ( $< 50\mu\text{s}$ ). **(J)** Increasing the spiral size (15 $\mu\text{m}$  diameter, excluding the central  $\sim 4\mu\text{m}$ ) correspondingly increased the necessary exposure time. Note all behavior optogenetic stimulation protocols in Fig. 3-6 were operated using this condition with a switching time of 80 $\mu\text{s}$ .

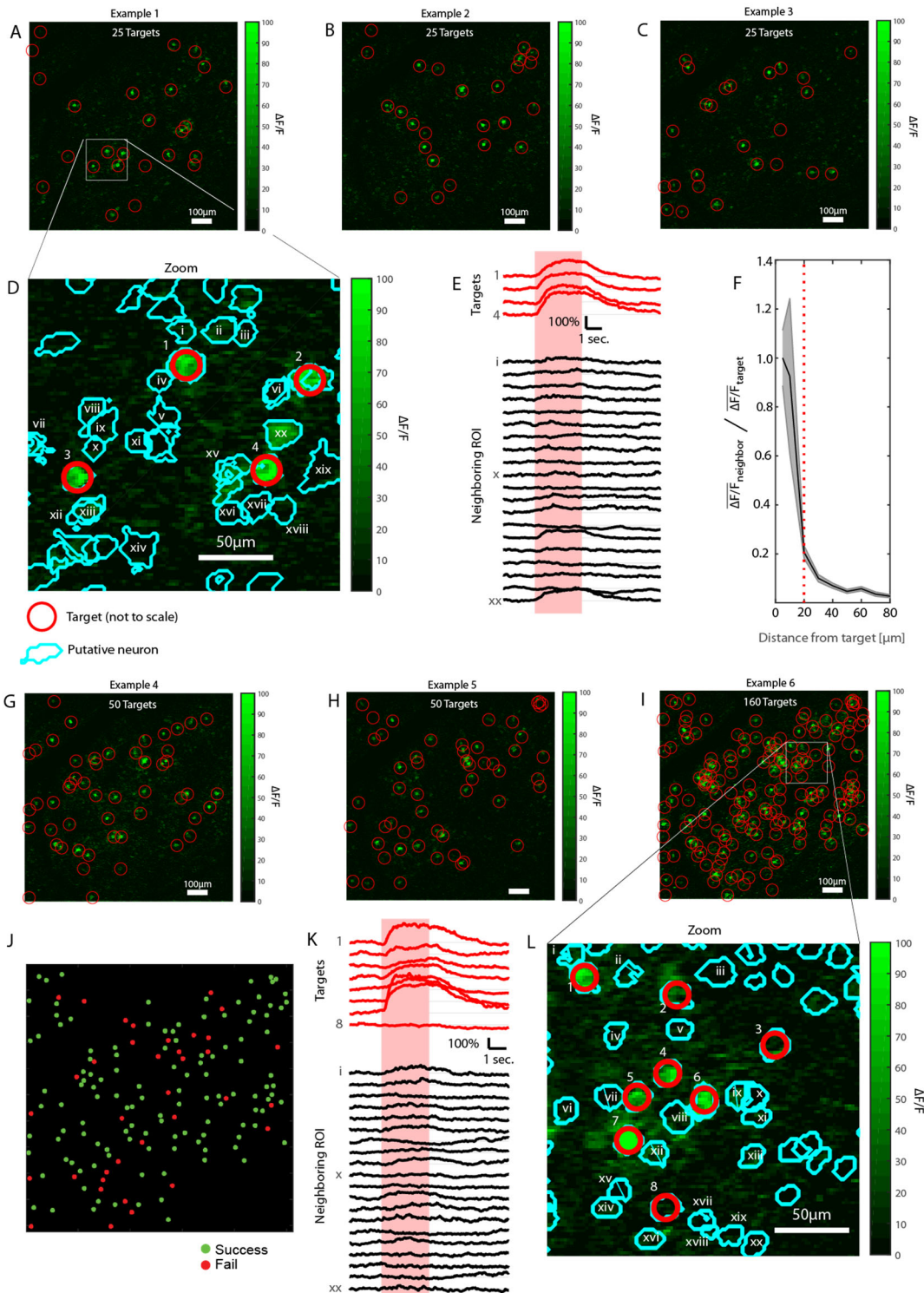


**Fig. S5. Optogenetic targeting and ‘off-target’ properties.** (A) Pixel-wise  $\Delta F/F$  across the entire acquisition image during the simultaneous optogenetic excitation of 25 targets using protocol in panel Fig. S4G. Targets are denoted as red circles which are not to scale with the actual target spiral. Note that the colormap has a max.  $\Delta F/F$  of 100% to aid in visualization of weaker modulations associated with putative ‘off-target’ neurons which may or may not be present across

the sample. Average of 8 trials. Two additional examples acquired under exact same conditions are provided as (B-C). (D) Visualization of putative ‘off-target’ neurons from (A) with ROIs provided of estimated neurons from CNMF. (E)  $\Delta F/F$  traces from the binary ROIs identified in (D) showing representative target (red) and neighboring (black) neuron activity across the stimulation epoch. Average of 8 trials, baseline is 1 sec. of data prior to stimulation. (F) Quantification of the average  $\Delta F/F$  from neurons located in  $10\mu\text{m}$  annuli as a function of distance from a target in (A-C), scaled relative to the average  $\Delta F/F$  of targets which experienced successful stimulation (70/75 targets, one-sided t-test of target ROI during stimulation epoch vs. during control trials,  $p \leq 0.01$ ). Exclusion radius of all ROIs used in neural analyses of behavioral data is  $20\mu\text{m}$ . Error bars are s.e.m. (G-H) Pixel-wise  $\Delta F/F$  across the entire acquisition image during the simultaneous optogenetic excitation of 50 targets using protocol in Fig. S4G. (I) Pixel-wise  $\Delta F/F$  across the entire acquisition image during the sequential optogenetic excitation of 160 targets using protocol in Fig. S4H (average of 27 targets per 1ms exposure). (J) 160 target cells are identified as successful optogenetic stimulations (green) or unsuccessful (red) and used to map the success rate across the imaging field-of-view in Fig. 2C. (K-L) Visualization and  $\Delta F/F$  traces of putative ‘off-target’ neurons from (I) with ROIs provided of estimated neurons from CNMF.



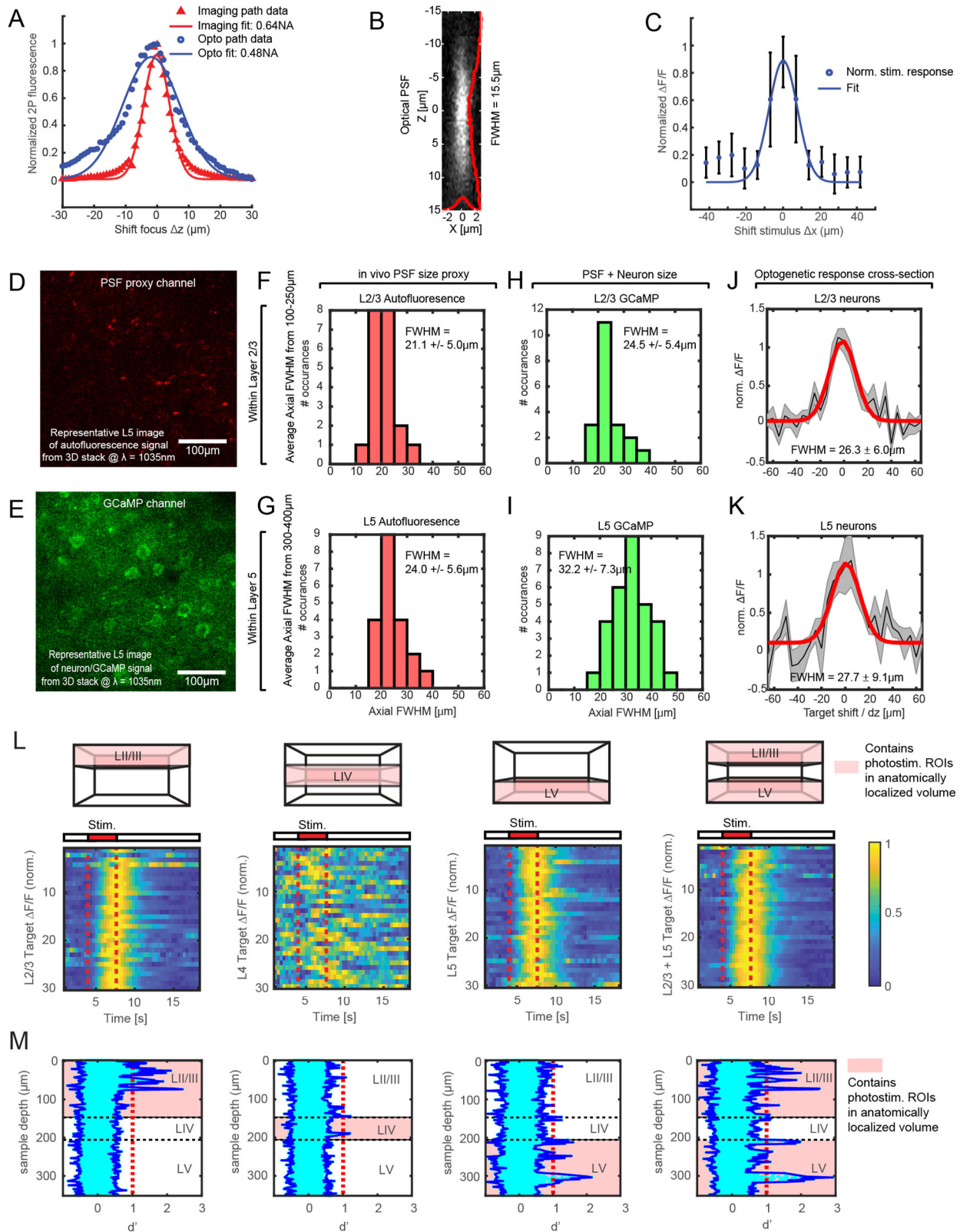


**Fig. S6. Spatial precision of the MultiSLM.** (A) Empirical, axial optical PSF measurements of both the optical imaging beam (FWHM = 9.6 $\mu$ m, NA<sub>est</sub> = 0.64) and an optogenetic stimulation beam (FWHM = 21.4 $\mu$ m, NA<sub>est</sub> = 0.48) using the Nikon 16x/0.8 NA microscope objective in the MultiSLM microscope. Data collected by translating a ~3 $\mu$ m thick fluorescent slide through a focused beam. Best-fit to the empirical measurements was calculated using the square of a Gaussian function. (B) Empirical optical PSF measurements of the MultiSLM optogenetic beam taken at  $\lambda$ =1035nm, using 1 $\mu$ m fluorescent beads. (C) The physiological response, as characterized by the percentage change in GCaMP6m fluorescence, when using a 15 $\mu$ m diameter spiral for optogenetic photostimulation (9-spirals, 0.63ms duration, as used in behavior experiments; n = 10 neurons in vivo, mean response across 5 trials per stimulation location—the spiral was intentionally shifted from center of each cell by the defined lateral offset—randomized and interleaved, normalized to maximum for each cell, fit with a single gaussian function, error bars are s.e.m.). (D) The red acquisition channel of a raster-scanned image using the MultiSLM optogenetic beam and scanning with the optogenetic galvo pair. Excited fluorescence from data acquisition of an in vivo preparation following the same protocols as the behavior cohort is suspected to be lipofuscin granules of ~7-8 $\mu$ m diameter. (E) The simultaneous green acquisition channel from raster-scanning the beam in (D). Excited fluorescence is GCaMP6m. (F) Putative granules from (D) were manually identified (N=20) in Layer 2/3 of cortex and Gaussian envelopes were fitted to the axial intensity profiles. The FWHM of the fits are reported as the histogram. (G) Putative granules from (D) were manually identified (N=20) in Layer 5 of cortex and the associated FWHM fits are reported in the histogram. (H) Neurons from (E) were manually identified (N=20) in Layer 2/3 of cortex and Gaussian envelopes were fitted to the axial intensity profiles. The FWHM of the fits are reported as the histogram. (I) Neurons from (E) were manually identified (N=30) in Layer 5 of cortex and Gaussian envelopes were fitted to axial intensity profiles. (J) All-optical physiological response of Layer 2/3 neurons (N=7), as measured by the relative change in GCaMP6m fluorescence, as the optogenetic ensemble target pattern is axially displaced, dz. Error bars are s.e.m. (K) All-optical physiological response of Layer 5 neurons (N=7), as measured by the relative change in GCaMP6m fluorescence, as the optogenetic ensemble target pattern is axially displaced, dz. Error bars are s.e.m. (L) Optogenetic excitation of manually-selected targets with no known functional association, segregated by anatomical layer (L2/3 only, L4 only, L5 only, L2/3+L5), demonstrate positively responding neurons localized only in the anatomical layers associated with viral expression under the AAV8-CaMKIIa-GCaMP6m-p2a-ChRmine-TS-Kv2.1-HA construct. Averaged and normalized  $\Delta F/F$  results from N=5 randomized trials of the four unique target ensembles in each of the four cases are presented in the lower row. The imaging conditions match those reported in our naïve and behavior protocols. Note that since little expression was localized to L4, the targets for that stimulation condition are not localized to cell bodies with high confidence. (M) To measure to axial localization of the photostimulation response across the entire sampled volume, fluorescence modulations were quantified from every exclusive set of 8x8 pixel ROIs throughout the image acquisition volume. They are then organized according to sample depth during image acquisition and then aligned by the conditions in (L). Optogenetic modulation is measured by the d' (the difference in the mean number of counts acquired during photostimulation versus baseline, divided by the average of the standard deviation in counts of both time epochs) of each 8x8 pixel ROI. Supporting evidence that the optogenetic targeting is axially/anatomically localized is seen in the 1<sup>st</sup>, 3<sup>rd</sup>, and 4th columns where significant

responses are isolated to L2/3, L5 and L2/3+L5, respectively. Conversely, when the same amount of stimulation light is delivered to L4, no significant modulation is seen in layers above or below.

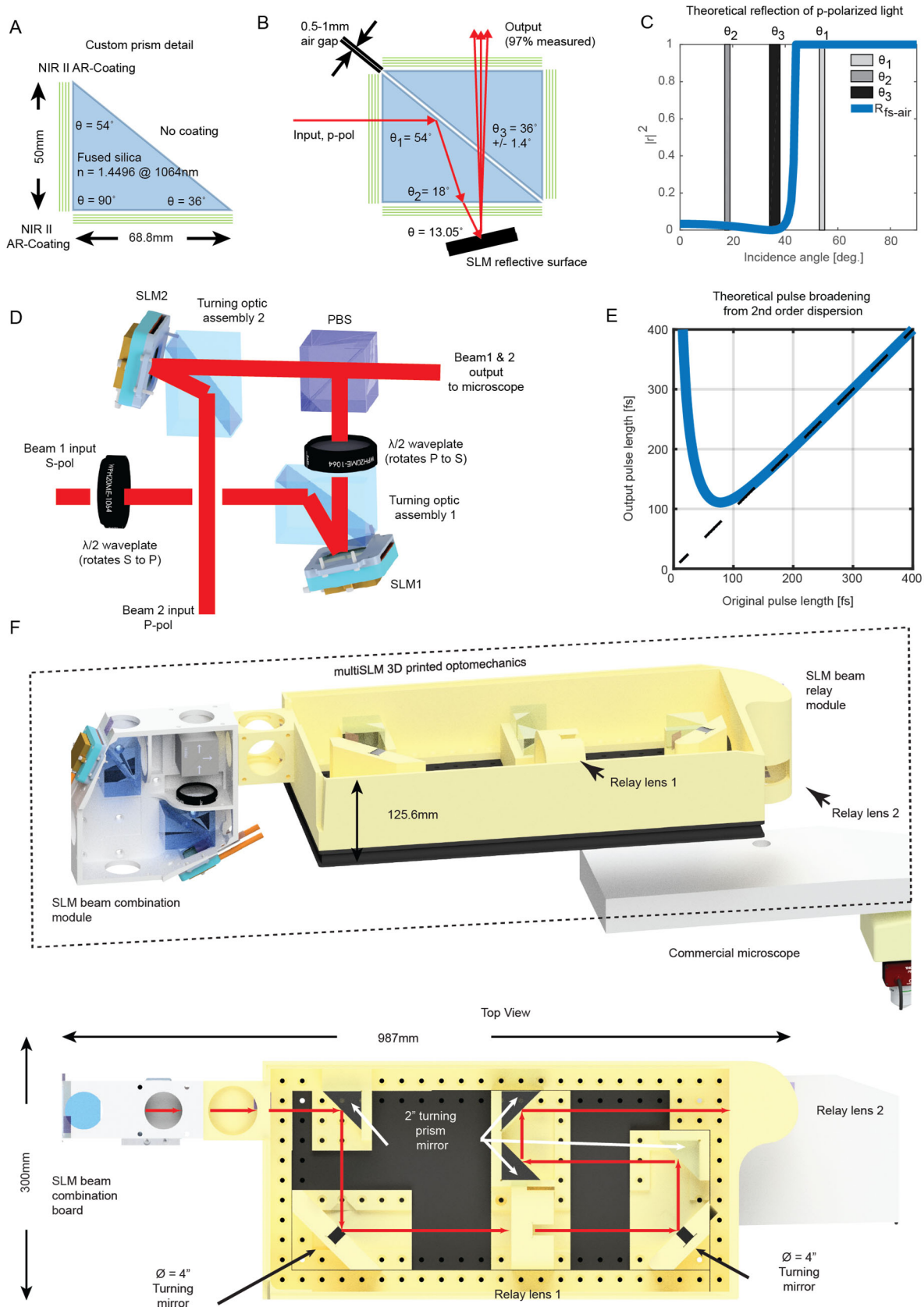


**Fig. S7. Optomechanics for MultiSLM.** The MultiSLM microscope utilizes a novel beam folding approach and 3D printed optomechanics to minimize size and promote mechanical stability. (A) A custom 36°-54°-90° prism was manufactured (Edmund Optics) of fused silica and anti-reflection (AR) coated on two faces to minimize air-to-glass interface reflections. (B) A pair of prisms, separated by an air gap, are used to redirect a P-polarized input beam to an SLM and to have the SLM output beam exit at a 90° angle, with minimal optical loss (97% throughput measured using a mirror as a proxy for SLM backplane). Note the three specified angles ( $\theta_1$ ,  $\theta_2$  and  $\theta_3$ ) are all related to the angle of the beam when propagating from the fused silica into the associated air interface. (C) The specific angles of the prism were chosen to allow beam propagation through the turning prism assembly which is aligned to the peak and minimum Fresnel reflection coefficients ( $|r|^2 = 0$  is total transmission,  $|r|^2 = 1$  is total reflection) in order to allow maximum photon efficiency. The specific angles highlighted with a gray-scaled bar are associated with the angles identified in (B).  $R_{fs-air}$  is the theoretical scalar coefficient of reflected intensity (e.g., the reflection coefficient of the first interface  $\theta_1$ , from the fused silica to the air-gap, is 1 – indicating total reflection). (D) Two turning optic assemblies are utilized, along with beam polarization optics, to co-linearly combine the SLM outputs from a pair of input beams. Half-waveplates are utilized to control the light polarization for maximum transmission through the system. (E) Pulse propagation through di-electric material (e.g. glass) can induce a chromatic phase delay which leads to pulse broadening, and therefore less efficient multi-photon excitation. Theoretical modeling of femto-second pulses from the light source as it propagates through these turning prisms (118.8 mm of fused silica, blue curve) indicates that while sub-100 fs pulses would experience significant pulse broadening, minimal pulse broadening is expected using the current optogenetic stimulation light source (nominally between 250 and 300 fs) (83). (F) 3D printed optomechanics are used to mount and align the MultiSLM optogenetic path to the commercial microscope. Two distinct optomechanic groups represent the complete set of 3D fabricated parts - the SLM beam combination module and the SLM beam relay module. The SLM beam combination module provides convenient reference points to align and secure the SLMs as well as the beam turning prisms and polarization optics. The MacroSLMs were designed to use the mechanical face of the external SLM mount as a flush and parallel mount to the combination module using 4-40# cap screws. The prism pair are kept parallel to each other and normal to the incident beam by reference groves in the seating of the 3D printed module. The SLM combination module mounts to the beam relay module by use of cap screws and/or Thorlabs cage railings in order to provide a reliable alignment. Within the beam relay module, the optical path is folded by use of 50 mm leg right-angle mirrors and 100 mm circular mirrors to ensure that zero beam vignetting occurs on this smaller footprint. Each 50 mm leg right-angle mirror has guide-points along each leg for precise placement on the 3D printed footings which directly bolt to a 12"x24" Thorlabs breadboard using the 1" hole-spacing. The custom beam relay lenses were aligned and mounted in custom 3D printed optomechanics within the module. By referencing to the 1" grid system of the breadboard, and keyed to other 3D printed components on the board, the relative positions of the two lenses could be readily optimized to ensure precise alignment and telecentricity. Note, both the relay lenses could be rapidly removed from the system to test or verify alignment using these custom optomechanics.

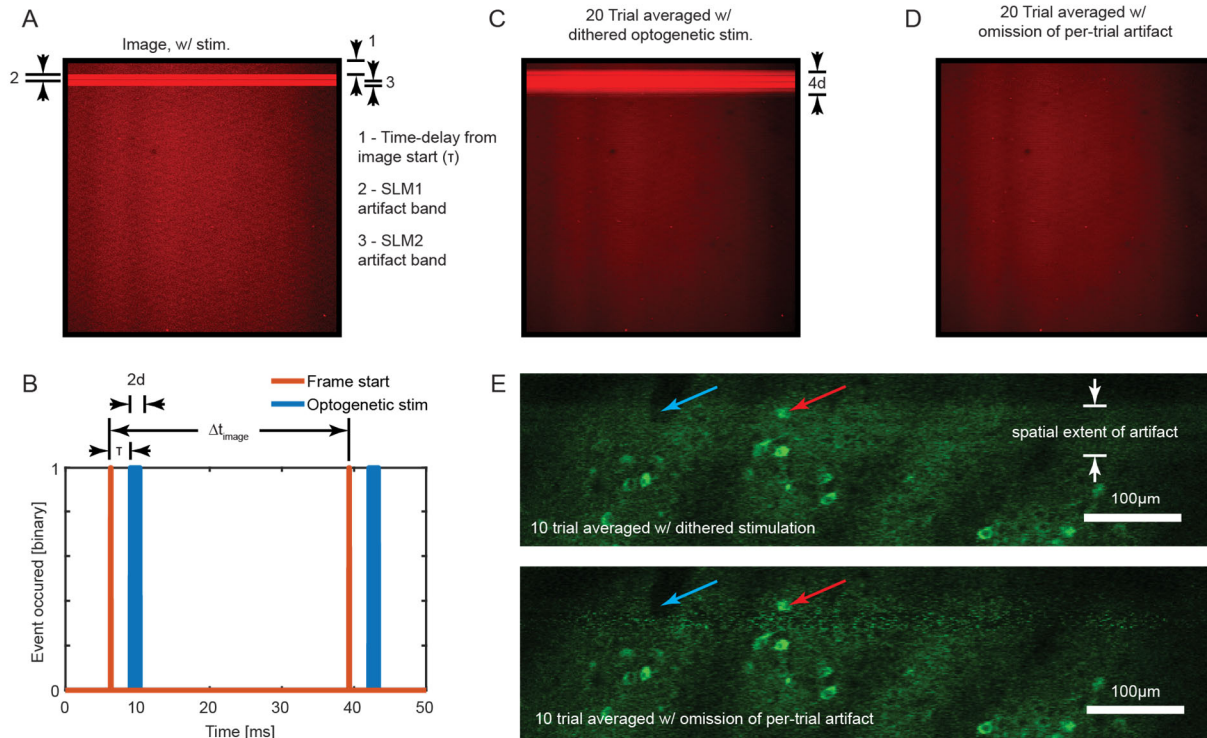


**Fig. S8. Removal of photostimulation artifact in imaging channel of MultiSLM.** (A) Targeted excitation of the opsin-fluorophore expressing neurons at  $\lambda = 1035\text{nm}$  results in a spatial block of pixels with increased background signal from co-excitation of the GCaMP6m reporter (here a bulk fluorescent slab serves as a phantom proxy), where the width of the artifact block is directly related to the excitation duration width. Note that optogenetic stimulation of each ensemble will result in an individual artifact band of width proportional to the ratio of the photostimulation duration (here  $0.63\text{ ms}$ ) to the imaging line-scan time (here, typical is  $64.9\text{ }\mu\text{s}$ ). Shown here are two ensemble stim artifacts,  $e_1$  (SLM1) and  $e_2$  (SLM2), analogous to **Fig. S4J** and the protocol applied *in vivo*. (B) Random offsets of the trial time ( $\tau$ ), where  $\tau \in \{-\mathbf{d}, \mathbf{0}, +\mathbf{d}\}$  and  $\mathbf{d}$  is the optogenetic exposure duration, diversifies which image pixels which will have a photostimulation artifact. Representative recording of the optogenetic stimulation onset and frame start (where  $\Delta t_{\text{image}}$  is frame acquisition time) which is used to track the relative timing and therefore the pixels which are contaminated by the artifact. (C) Trial mean intensity image taken from 10 trials of 30 Hz stimulation with trial-to-trial temporal shifting (dithering) of the onset ( $\tau$ ). The randomized onset shift broadens the artifact on average but the diversity provides artifact-free access to every pixel for at least 1/3 of trials. (D) Result from artifact removal in the trial mean intensity image by omitting all pixels with artifact from the average on a per trial basis. (E) Comparison of this artifact removal *in vivo*. Top: Mean intensity image (one time-point averaged from 10 trials) when including the temporally shifted photostimulation artifact. Bottom: Mean intensity image (same time-point at above) when omitting the pixels associated with photostimulation artifact on a per trial basis. Areas representative of the increased contrast as a result of removing the additive photostimulation artifact are highlighted (cyan and red arrows). Note a Kalman filter (gain = 0.8, noise = 0.05) was applied to the time-series data after the artifact removal. All stimulation artifact

fluorescence was completely removed from analyses of visual experiments by excluding artifact-contaminated pixels (**Materials and Methods**).

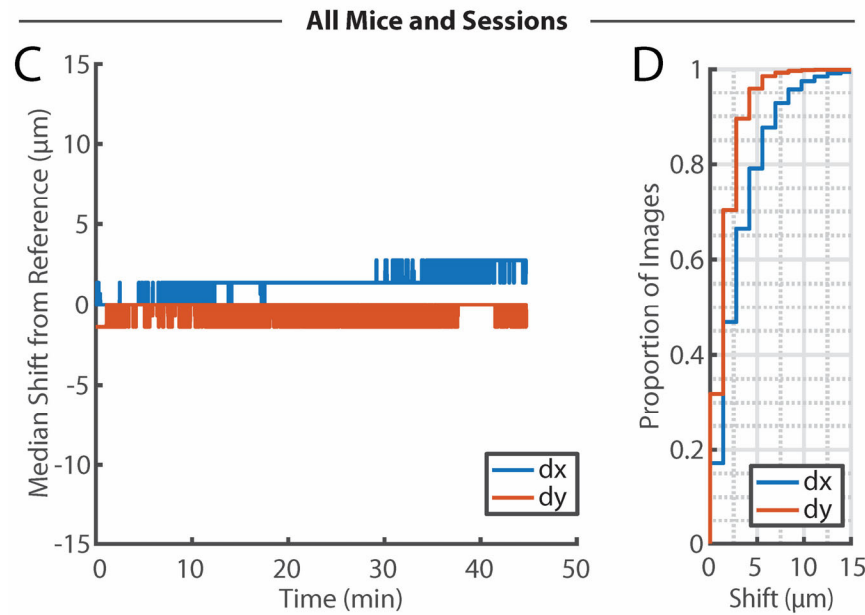
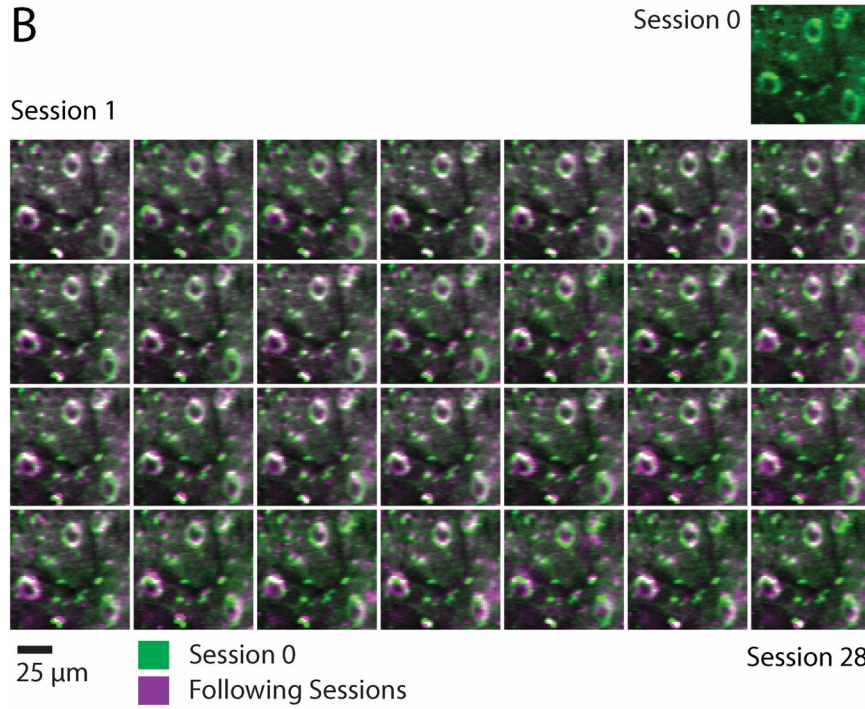
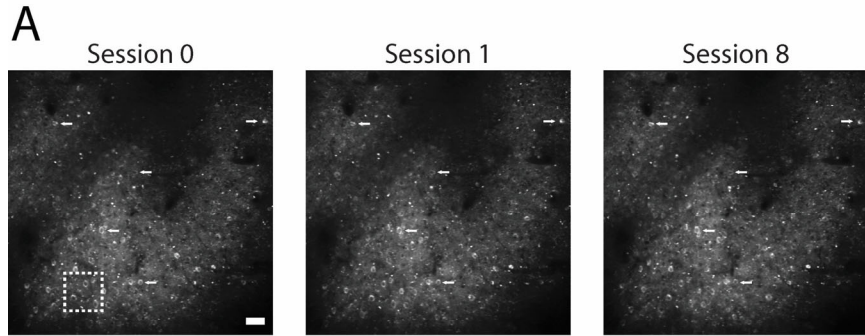




**Fig. S9. Targeting the same ensembles across weeks with cellular resolution.** (A,B) The same population of neurons is revisited for many weeks (29 sessions spanning 54 days) by precisely aligning the MultiSLM imaging/optogenetic volumetric stimulation systems to the original field of view (A, full optical slice in layer 5 from the live imaging volume, scale bar 50  $\mu\text{m}$ , white arrows indicate examples of correspondence between the images; B, region of interest in layer 5 with 4 labeled cell bodies, corresponding to white box in A; overlay: green, original imaging session, magenta, each subsequent session of imaging and optogenetics). (C,D) Alignment is maintained online during the experiment using a real-time cross-correlation algorithm to compensate for the shift between the instantaneous image and the reference image (from day 0) for each slice through the volume (**Materials and Methods**). (C) Shift relative to the reference image over the duration of the experiment (dx, blue; dy, red; median data are plotted across 9 mice, optical z slices and sessions). (D) Shifts relative to reference image for all images (dx, blue, dy, red; 95% of all shifts were  $< 8.34 \mu\text{m}$  (dx) and  $< 4.17 \mu\text{m}$  (dy);  $\sim 2.5$  million image shifts from reference across 9 mice from all optical z slices and sessions).

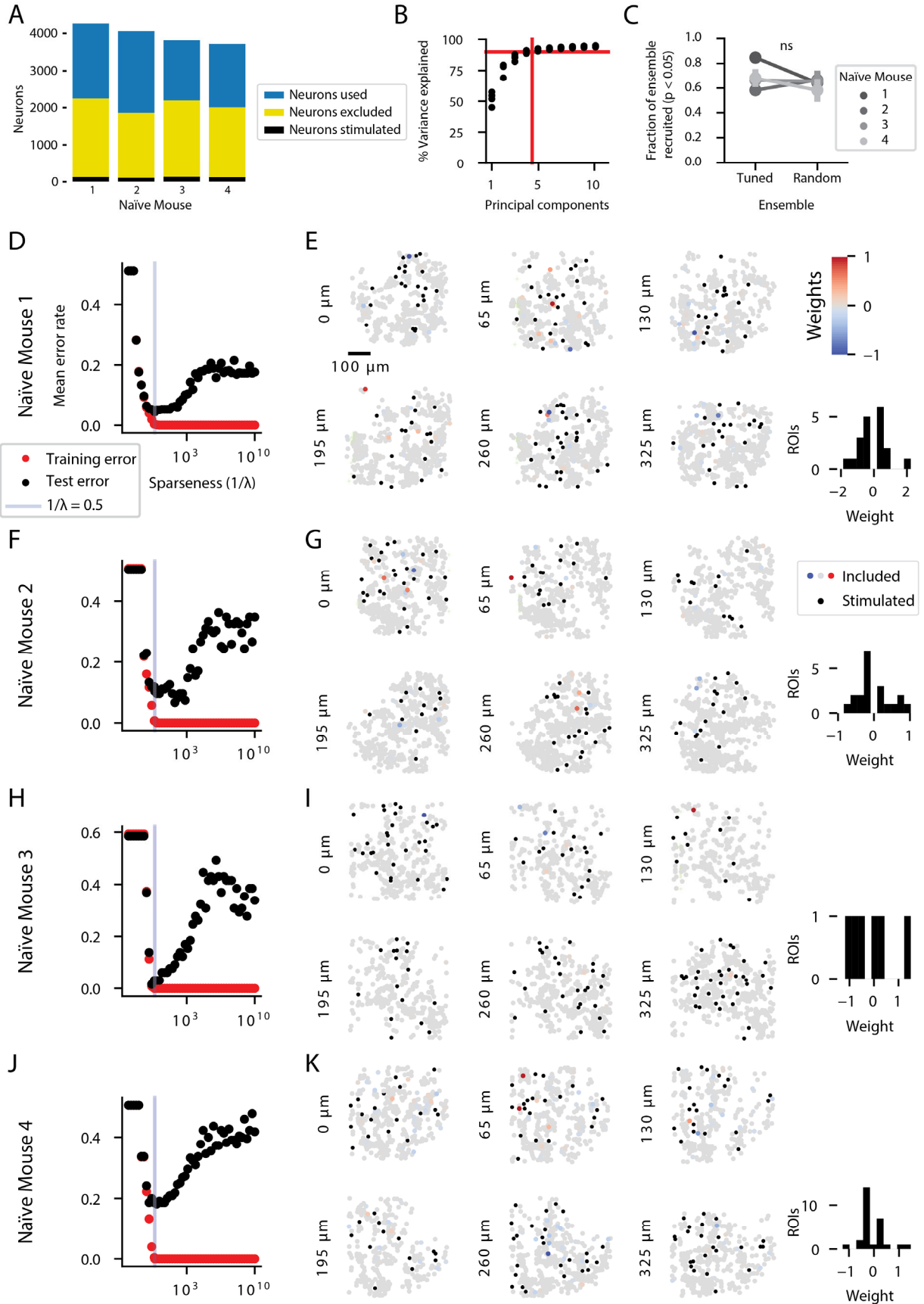


**Fig. S10. Parameter estimation for classifier analysis of behaviorally naïve mice.** (A) Bar graph indicating the fraction of all imaged neurons that were used for classifier and neural trajectory analyses (neurons used are termed “unstimulated neurons”). (B) Plot indicating cumulative variance explained by increasing numbers of Principal Components (PCs) as applied to the unstimulated neuronal traces during visual stimulus presentation. Results shown for four mice. Horizontal red line is at 90%. The vertical red line indicates that five PCs are necessary to explain at least 90% of the variance in all four mice. (C) The fraction of optogenetically stimulated tuned (left) and random (right) neurons that were significantly modulated by light is shown for  $n = 4$  naïve mice using 60 stimulation trials/neuron (using conservative metrics; see **Materials and Methods**). A paired t-test pooling across mice revealed no significant difference between these two distributions ( $p = 0.48$ ). (D, F, H, J) Classifier performance shown for four behaviorally naïve mice as a function of the number of neurons with classifier regression weights equal to zero increases (which increases as a function of the parameter  $1/\lambda$ ). A constant value ( $1/\lambda = 0.5$ ) was used across all four mice. We found that this value approximately minimized each model’s prediction error on held-out test data (that was not used for training). (E, G, I, K) Spatial map of all ROIs extracted across six cortical depths shown for four naïve mice. Black dots (targets) were excited by 2P illumination in at least one experimental condition. Excluded ROIs (not shown but counted in Panel A) were within 20 microns of a target ROI at some depth or were contaminated by a 2P-induced stimulus fluorescence artifact and were excluded from the classifier analysis. Remaining ROIs (colors) were used for classifier analysis. Right histograms show weight values for ROIs that had weights  $> 10\%$  of the maximum weight obtained by any ROI. Scale bar is 100  $\mu\text{m}$ .

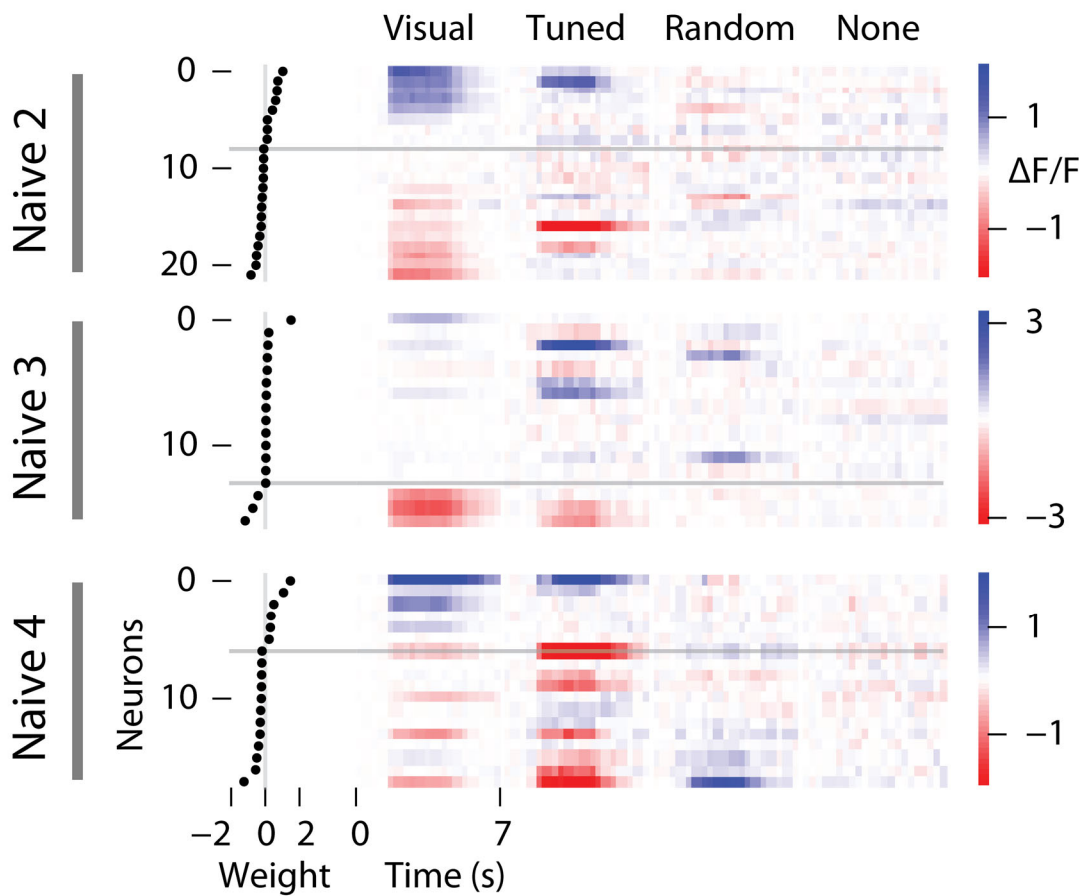


**Fig. S11. Neural selectivity of additional behaviorally naïve mice.** Each row shows the trial-averaged fluorescence response of a neuron during the  $0^\circ$  visual stimulus minus its response during the  $90^\circ$  visual stimulus (or matched optogenetic stimulus) for all neurons with large classifier weights (defined as  $\text{abs}(\text{weight}) > 99^{\text{th}}$  percentile). This analysis is shown here for three naïve mice not shown in the main text. Dots on the left-hand side of each row indicate the classifier weight of each neuron. Blue indicates neural responses preferential to the  $0^\circ$  condition, red responses were stronger for the  $90^\circ$  condition.

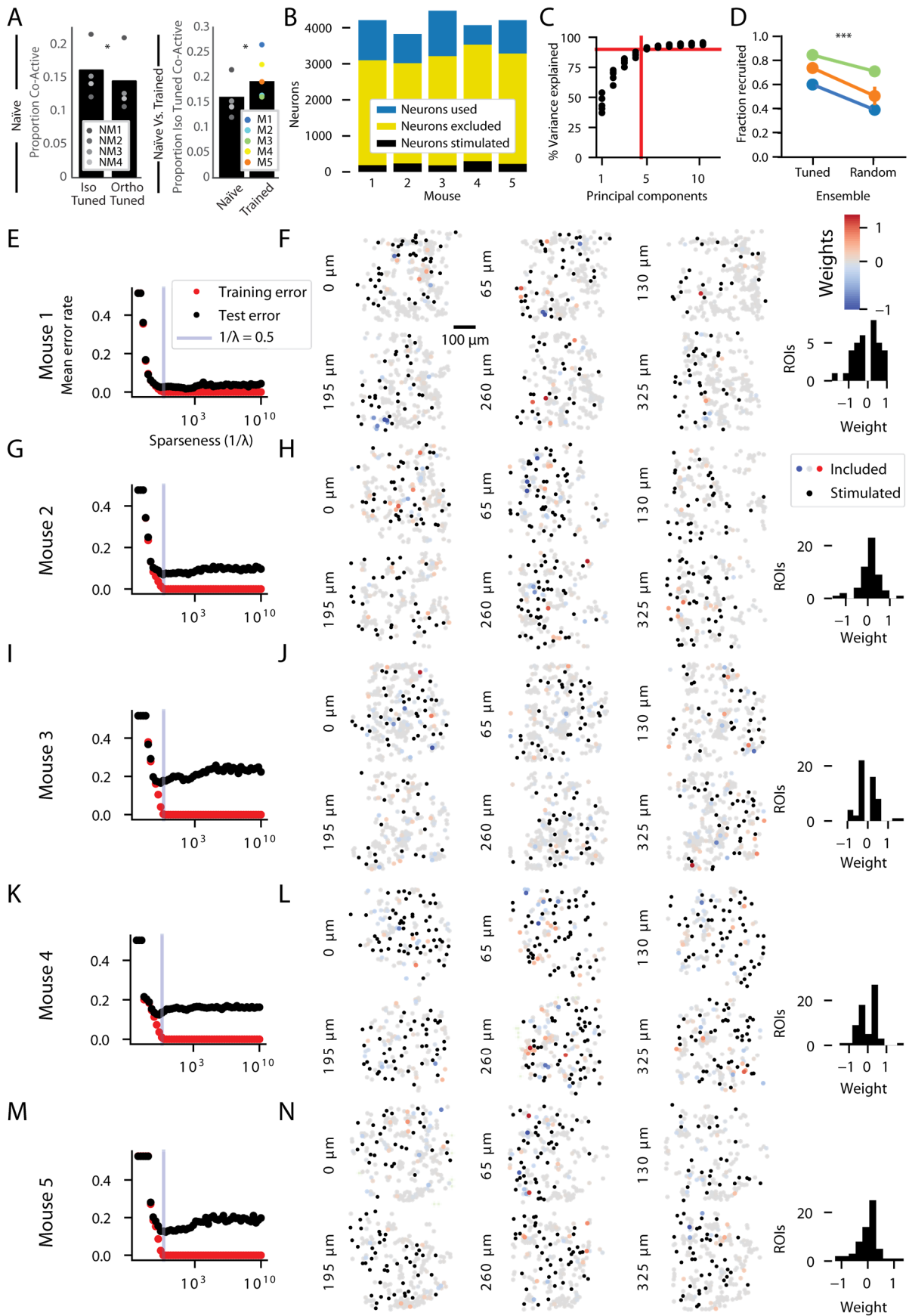


**Fig. S12. Parameter estimation for classifier analysis and tuned visual network recruitment in behaviorally trained mice.** (A, left) Among the non-targeted cells in naïve mice, both iso-tuned and orthogonally-tuned neurons are secondarily recruited during tuned ensemble optogenetic stimulation, with a modest preference for iso-tuned in the absence of visual stimuli, ( $p < 0.05$ ,  $\chi^2$  two tailed test). Data are pooled across sessions and mice for bars and statistics ( $n = 25$  sessions in 5 mice; co-active neurons are found by two-tailed Wilcoxon signed-rank tests,  $p < 0.05$ , sample window vs. baseline, **Materials and Methods**). (A, right) Recruitment of iso-tuned populations is enhanced with training on the visual discrimination task ( $p < 0.05$ ,  $\chi^2$  two tailed test, trained vs. naïve cohorts). Data for each mouse in each cohort are shown as shaded or color dots corresponding to stratified Cochran-Mantel-Haenszel (CMH) tests controlling for mouse identity (**Materials and Methods**, see legends: NM is Naïve Mouse, M corresponds to a trained mouse consistent with main figures and numbering throughout this figure). (B) Bar graph indicating the fraction of all imaged neurons that were used for classifier and neural trajectory analyses (neurons used are termed “unstimulated neurons”). The number of unstimulated neurons was  $929 \pm 250$  [mean  $\pm$  SD], or  $21 \pm 5\%$  of all neurons in each of the 5 mice in this cohort. (C) Plot indicating cumulative variance explained by increasing numbers of Principal Components (PCs) as applied to the unstimulated neuronal traces during visual stimulus presentation. Results shown for five trained mice. Horizontal red line is at 90%. The vertical red line indicates that five PCs are necessary to explain at least 90% of the variance in all five mice. (D) The fraction of optogenetically stimulated tuned (left) and random (right) neurons that were significantly modulated by light is shown for  $n = 3$  trained mice that had at least 40 stimulation trials/neuron (using conservative metrics; line color corresponds legend in (A); see **Materials and Methods**). A paired t-test revealed that a higher fraction of neurons within tuned ensembles were recruited by optogenetic stimulation than with random ensembles (Fig. S10D,  $p < 0.001$ , paired t-test,  $n = 3$  mice). The remaining two mice in the trained mouse cohort had insufficient random-only stimulation data (i.e. the random condition was not run on enough days) to make this comparison. (E, G, I, K, M) Classifier performance shown for five trained mice as a function of the number of neurons with classifier regression weights equal to zero increases (which increases as a function of the parameter  $1/\lambda$ ). A constant value ( $1/\lambda = 0.5$ ) was used across all five mice. We found that this value approximately minimized each model’s prediction error on held-out test data (that was not used for training). (F, H, J, L, N) Spatial map of all ROIs extracted across six cortical depths shown for five mice. Black dots (targets) were excited by 2P illumination in at least one experimental condition. Excluded ROIs (not shown but counted in panel (A)) were within 20 microns of a target ROI at some depth or were contaminated by a 2P-induced stimulus fluorescence artifact and were excluded from the classifier analysis. Remaining ROIs (colors) were used for classifier analysis. Right histograms show weight values for ROIs that had weights  $> 10\%$  of the maximum weight obtained by any ROI. Scale bar is 100  $\mu\text{m}$ .

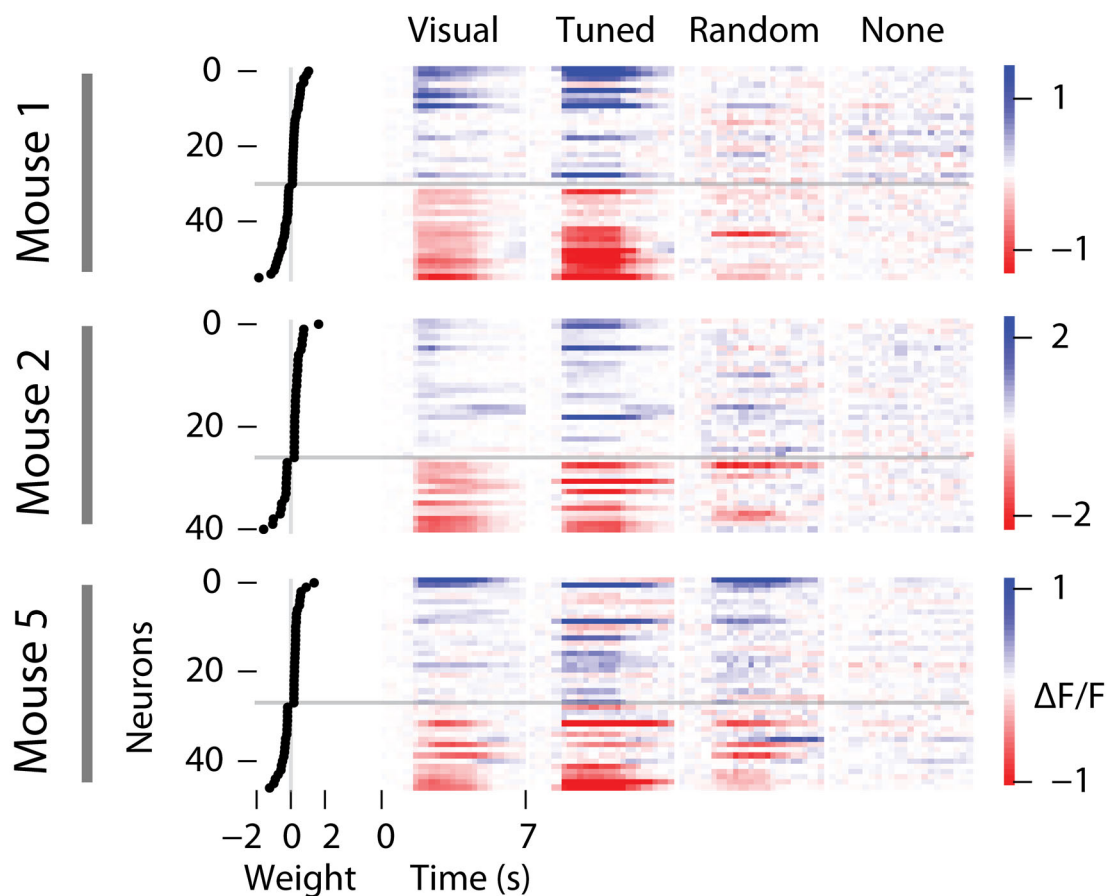


**Fig. S13. Neural selectivity of additional behaviorally trained mice.** Each row shows the trial-averaged fluorescence response of a neuron during the  $0^\circ$  visual stimulus minus its response during the  $90^\circ$  visual stimulus (or matched optogenetic stimulus) for all neurons with large classifier weights (defined as  $\text{abs}(\text{weight}) > 95^{\text{th}}$  percentile). This analysis is shown here for three trained mice not shown in the main text. Dots on the left-hand side of each row indicate the classifier weight of each neuron. Blue indicates neural responses preferential to the  $0^\circ$  condition; red responses were stronger for the  $90^\circ$  condition.

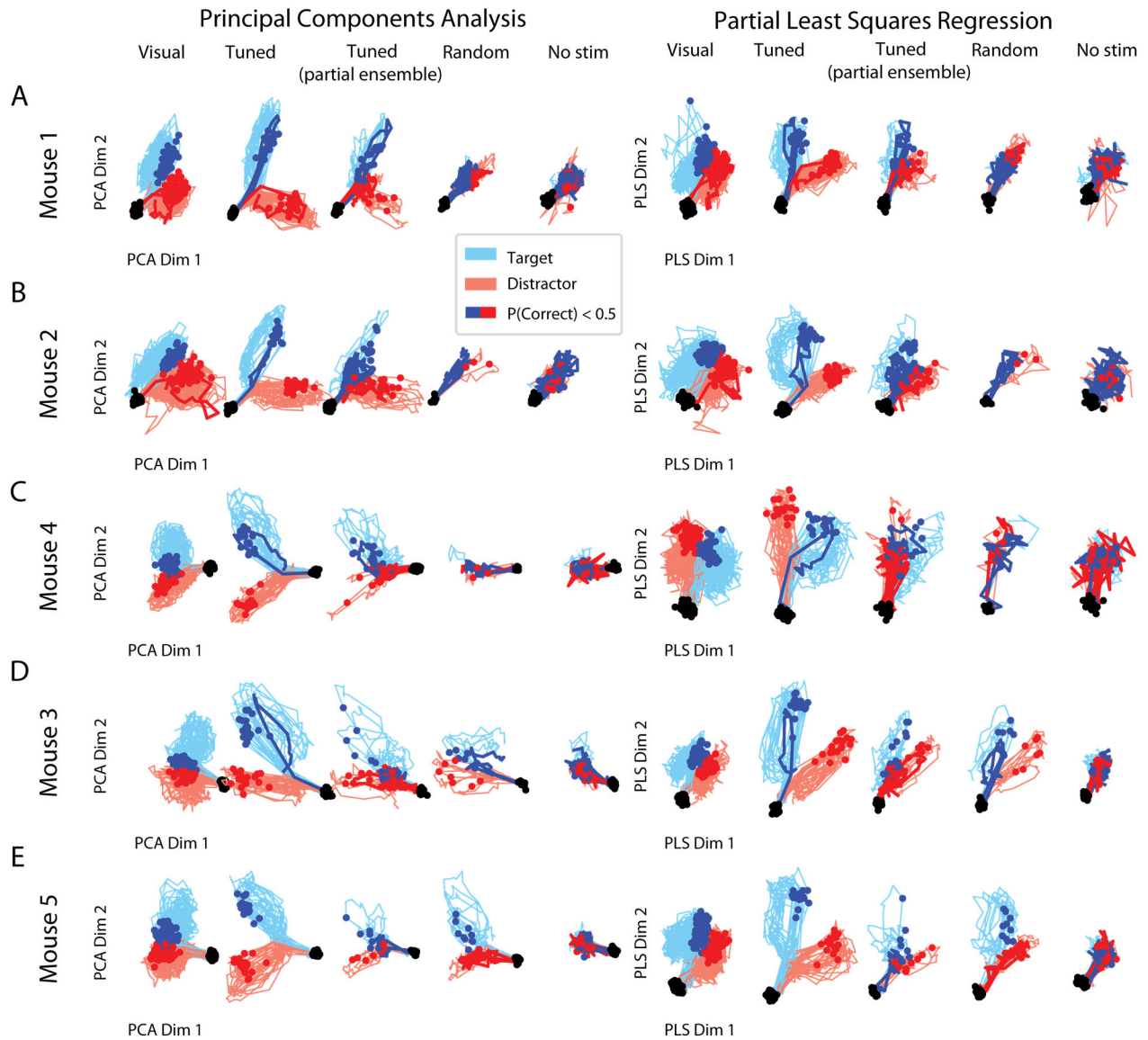


**Fig. S14. Visually evoked population activity is more similar to that evoked by stimulation of tuned ensembles than by random stimulation.** (A-E) Neural trajectories were computed individually for each experimental condition on each experimental day. The basis vectors were computed for each mouse with the visual only data, using either Principal Components Analysis (PCA, left column) or Partial Least Squares Regression (PLS, right column). Light blue trajectories represent data obtained during target conditions and light red trajectories represent distractor conditions. Dark blue and red trajectories denote target or distractor conditions where the mouse performed with mean performance less than 50% (meaning fewer than half of the trials on that condition and day elicited the correct behavioral response). Each trajectory is composed of neurons that were never optogenetically stimulated and that lie at least 20 microns away from any stimulated neuron. Principal Components (PC) were computed using visual-only data. Black dots represent the start of each trajectory. Red and blue dots mark the first frame following visual or



optogenetic stimulus onset and are superimposed onto each trajectory. For Mouse 3 and Mouse 4, all but the tuned partial-ensemble panels were shown in **Fig. 5**. They are reproduced here for completeness. If motor behavior plays a role in the shape of these neural trajectories, it would be expected that in the case of the mouse making a large number of behavioral errors, those trajectories would look distinct from trajectories constructed from data where high behavioral performance was observed. Instead we see that the highlighted red and blue trajectories (where mean performance was  $< 50\%$ ) look qualitatively indistinguishable from other red and blue trajectories from conditions where few errors were observed.

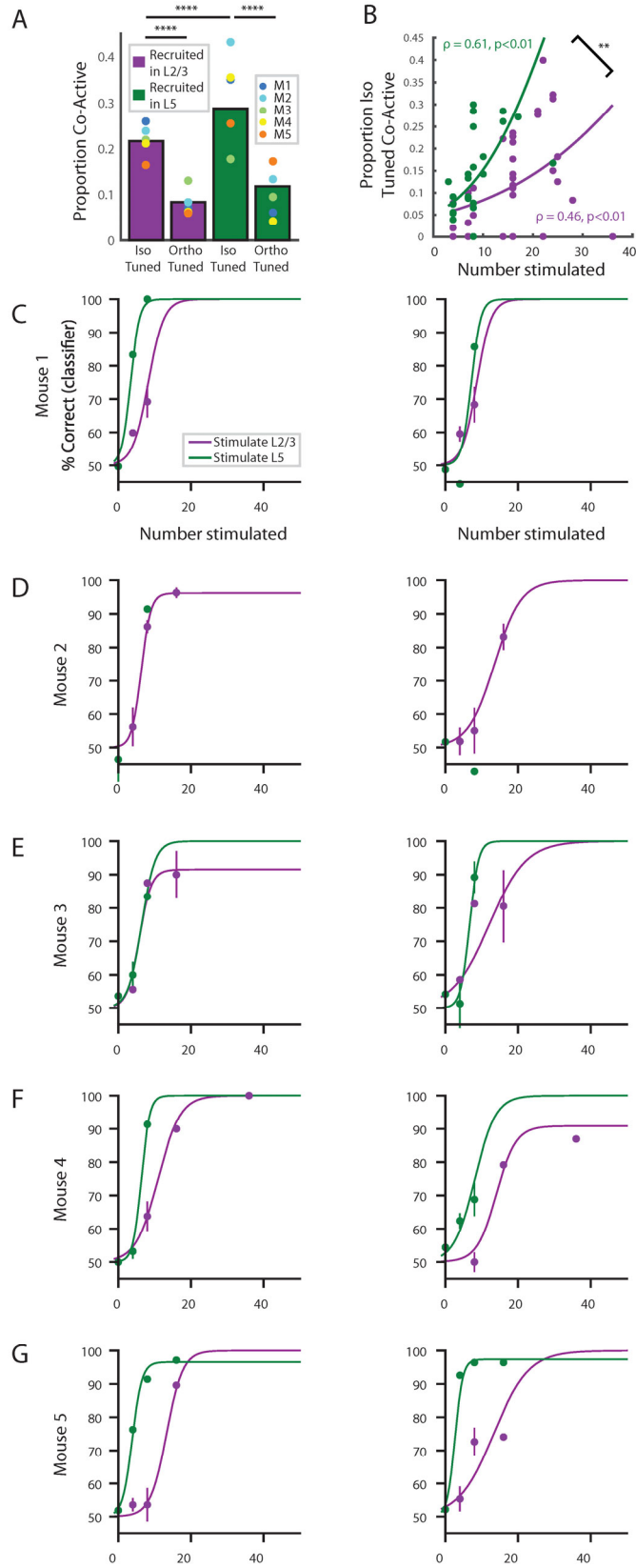


**Fig. S15. Selective laminar recruitment and excitation event threshold visualized for five individual mice.** (A) Stimulation of full tuned ensembles involving both layers 2/3 and 5 preferentially recruited iso-tuned neurons in both layer 2/3 and layer 5 ( $p < 0.0001$ ,  $\chi^2$  two tailed test, iso vs. ortho in each layer; co-active neurons are found by two-tailed Wilcoxon signed-rank tests,  $p < 0.01$ , sample window vs. baseline, **Materials and Methods**). A greater proportion of layer 5 iso-tuned neurons was recruited compared to layer 2/3 ( $p < 0.0001$ ,  $\chi^2$  two tailed test,  $n = 58$  experiments in 5 mice). Data were pooled across sessions and mice for each colored bar and reported with Pearson's  $\chi^2$  square test results; pooled data across sessions for each mouse shown as colored dots (see legend, per **Figs. 4H, 5D, 6A; Materials and Methods**: stratified CMH tests controlling for mouse identity). \*\* $p < 0.01$ , \*\*\*\* $p < 0.0001$  throughout. (B) Data from **Fig 6B,D** showing direct comparison of iso-tuned recruitment within each stimulated layer. Stimulation of layer 5 neurons recruits a greater fraction of layer 5 iso-tuned neurons more rapidly than layer 2/3 stimulation recruits iso-tuned layer 2/3 cells ( $p < 0.01$ , ANCOVA controlling for the covariate of number stimulated; Spearman's  $\rho = 0.46$ ,  $p < 0.01$ ,  $n = 46$  data points, within layer 2/3 and Spearman's  $\rho = 0.61$ ,  $p < 0.01$ ,  $n = 24$  data points for layer 5 recruitment). (C) Logistic psychometric functions (solid lines) fit to predictions derived from a classifier trained on either neural (left column) or behavioral data (right column) taken from a single mouse. Each curve relates the mouse's performance to the stimulation of a specific number of neurons. Individual points represent averages across the one or more days where a particular experimental condition was run +/- the s.e.m. Each plot shows fits to data for only conditions where ensembles resided in individual layers. (D-G) Results shown for four additional mice. Format matches (C). No psychometric function was fit to the layer 5 data from Mouse 2 because of insufficient data (there were not many targetable layer 5 neurons in that mouse). Matched target and distractor ensembles stimulated in each mouse differ in size by at most one neuron. Importantly, the parameters underlying the psychometric function fits were not used for any quantitative statistical analysis and are presented only for illustrative purposes.

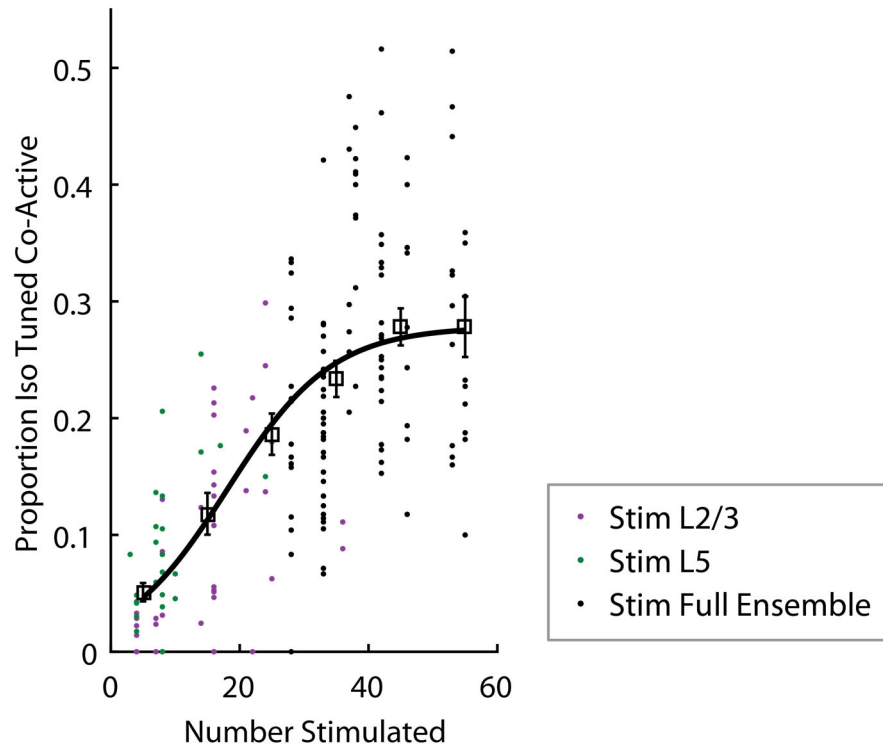


**Fig. S16. Summary of selective recruitment across the cortical volume for all layer-specific and full ensemble stimulation experiments.** The proportion of iso-tuned neurons that were recruited throughout the cortical volume during all layer-specific (layer 2/3 stimulation, magenta dots; layer 5 stimulation, green dots) and full, original ensemble stimulation experiments (black dots; data reproduced from **Fig. 5E**) rapidly increased as the number of stimulated neurons increased (Spearman's  $\rho=0.71$ ,  $p<0.0001$ ,  $n=186$  data points; combining full ensemble stimulation data shown in **Fig. 5E** and full volume, across layers recruitment data corresponding to the layer-specific stimulation experiments shown in **Fig. 6A-D**). Means $\pm$ s.e.m. (black boxes and error bars) are computed using data binned by number stimulated (width=10). A logit function (black curve) was fit to the mean, binned data for visualization purposes. For the fit, mean data points were normalized by dividing by the maximum mean value; the fit was rescaled for plotting by multiplying by the same value.

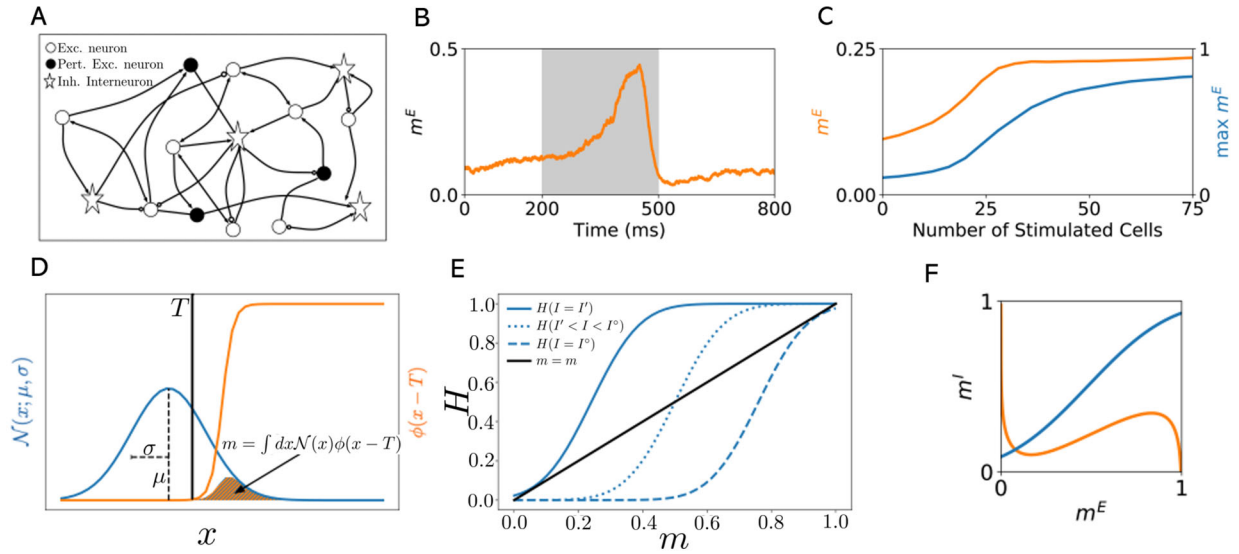


**Fig. S17. A critically excitable network model: simulation and analysis.** (A) A network schematic of recurrently connected excitatory (circles) and inhibitory (stars) neurons. Optogenetic stimulation is modelled by clamping the activity of a small number of excitatory neurons (black dots) to their saturated firing rate. (B,C) Direct simulation of the equations governing the single neuron input-output nonlinearity (2), membrane voltage integration dynamics (3), neuronal inputs (4), network connectivity (5), and external inputs (10) are performed via Euler integration with a time-step  $dt = 0.6\text{ms}$ . Smaller timesteps yielded similar results. Parameters exhibiting critical excitability were chosen to be  $N = 1500$ ,  $g=10$ ,  $p = 0.3$ ,  $I=0$ ,  $w^{EE} = 3$ ,  $w^{EI} = 2.25$ ,  $w^{IE} = 2.25$ ,  $w^{II} = 0.15$  and all thresholds were set to  $T=1$ . Zero mean noise is injected to each neuron with standard deviations  $\sigma_0^E = 0.75$  and  $\sigma_0^I = 0.75$ . (B) The  $I$  population is slower than the  $E$  population:  $\tau^E = 20\text{ms}$ ,  $\tau^I = 66\text{ms}$ . For a period of  $300\text{ms}$  (grey bar) a small subset of 30 excitatory neurons is stimulated, and the temporal traces show the mean activity ( $m^E$ ) of the rest of the unstimulated neurons. (C) The temporal average (orange) and peak fraction (blue) of mean activity of unstimulated neurons,  $m^E$ , during stimulation window (grey) yields a nonlinear increase to increasing stimulation. Error bars are smaller than the line thickness and reflect standard error across 250 repeated stimulation windows. (D) Illustration of the mean field solution. The distribution of membrane potentials  $x_i(t)$  across neurons  $i$  in a given population at an instant of time  $t$  converges in the limit of large numbers of neurons to a Gaussian distribution (blue) with mean  $\mu$  and standard deviation  $\sigma$ . The transfer function,  $\phi(x - T)$  (orange) relates the membrane potential to a firing rate. Here it is given by the logistic function  $\phi(z) = \exp gx / (1 + \exp gx)$ ; for large values of the parameter  $g$  it approaches the Heaviside function, which we employ in our theoretical analysis. The resultant output firing rate  $m$  of the population (shaded area) is given by the integral of the product of transfer function and the distribution of membrane voltages through (12). (E) Stationary points for the output firing rate of the excitatory subpopulation with fixed external inhibition marked by crossing of lines. Different curves show the RHS of (15) for different levels of inhibition  $I$ , while the unity line shows the LHS of (15). As the inhibition level is increased, the excitatory subpopulation undergoes two saddle-node bifurcations. (F) Nullclines of inhibitory (orange) and excitatory (blue) populations from equations (15) and (16) plotted as a function of the fraction of active neurons  $m^I$  and  $m^E$  in each population.

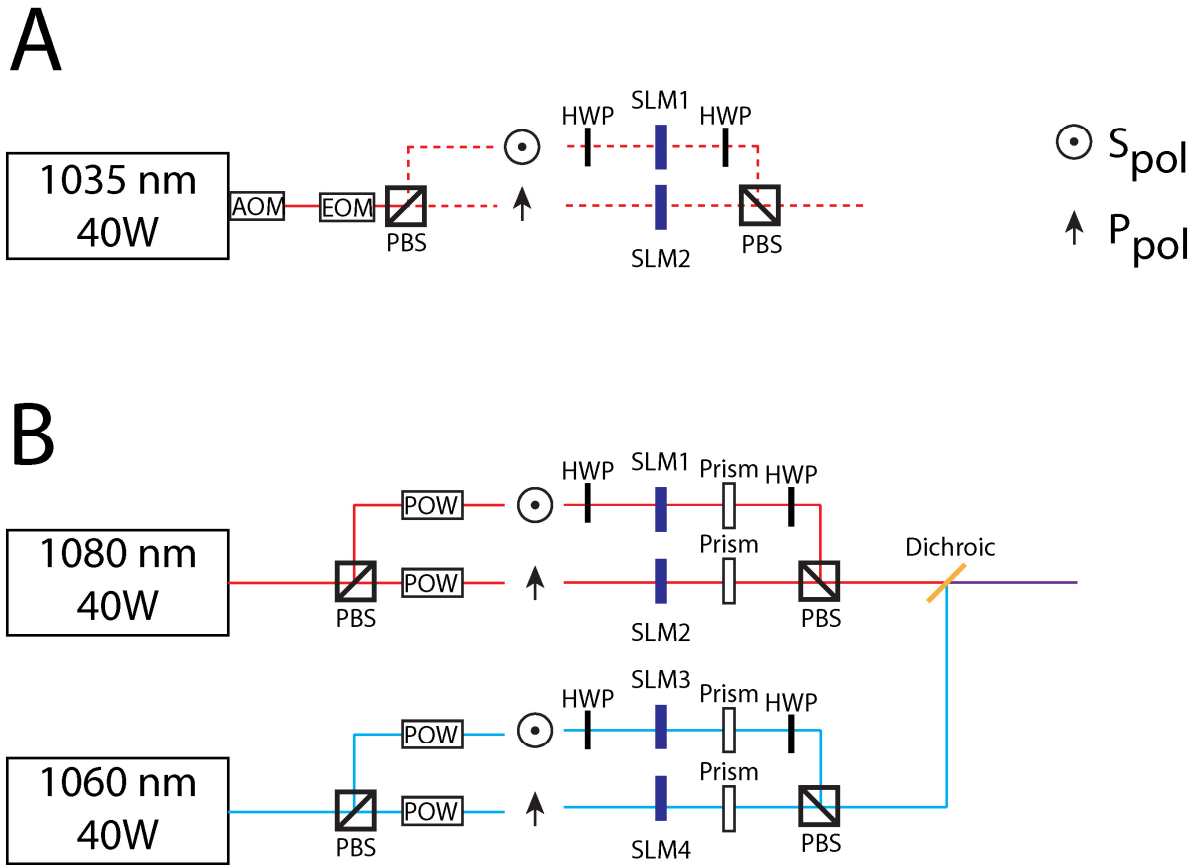
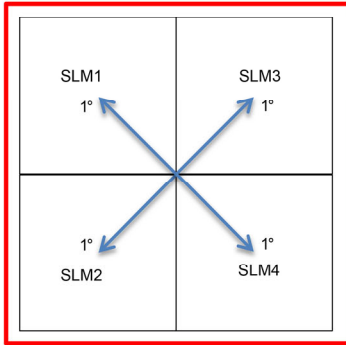


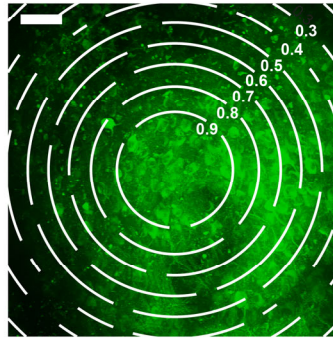
**Fig. S18. MultiSLM designs and scalability.** (A) Simplified, modular design for multiplexing two SLMs. This basic design was used for figures in the main text to enable temporal multiplexing of two SLMs in time to achieve kilohertz hologram refresh rate. In this implementation, the laser contains an acousto-optic modulator (AOM) to rapidly modulate power (200 kHz). The electro-optic modulator (EOM; Pockels cell) rapidly switches polarization (200 kHz, between S polarization/ $S_{pol}$ , and P polarization/ $P_{pol}$ ). A polarization beamsplitter (PBS) determines the subsequent optical path based on polarization of the beam, and therefore either SLM1 or SLM2, for hologram illumination. Half waveplates (HWP) rotate polarization before and after SLM1 to optimize illumination of the SLM ( $P_{pol}$  is optimal for MacroSLM; alternatively, the SLM could be rotated  $90^\circ$  to achieve the same effect). A polarization beamsplitter (PBS) combines both SLM-modulated paths together onto a single beam path. In this configuration, only one SLM path is illuminated at any time. (B) Multiplexing four SLMs using polarization, similar to (A), and wavelength (proof of concept in Fig. S19). Power is modulated on each independent SLM path (POW; either a Pockels cell with PBS, or AOM in our setup). A prism after each SLM is used to add constant tilt to the beam, effectively increasing the maximum deflection angle of the modulated path. Adding this tilt at  $90^\circ$  rotations for each SLM path allows each quadrant of a larger FOV to be addressed. A PBS combines both polarizations of each single wavelength, and a dichroic mirror combines both wavelengths. All four SLM paths can be illuminated and combined

fully simultaneously. In our setup, both lasers lines are synchronized to one another (and we have two 40W laser amplifiers available at each wavelength, fully synchronized, such that all four SLMs can receive a full 40W beam), and given inherently different path lengths for each SLM modulated beam, the combined beams from all beams do not interfere with one another given their low duty cycle on the femtosecond scale. Orthogonal polarizations should also effectively eliminate any interference, and wavelength differences should significantly reduce possible interference. Removing the prism from the beam paths (using a magnetic mount in our setup) re-centers each SLM on the same FOV, allowing full 4x multiplex of the same addressable volume in time.

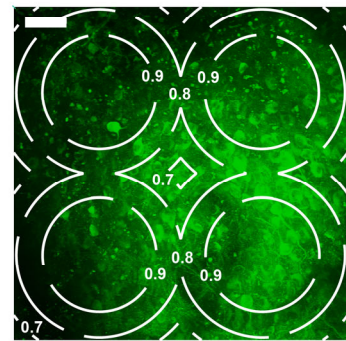
**A** Multiplexed FOV



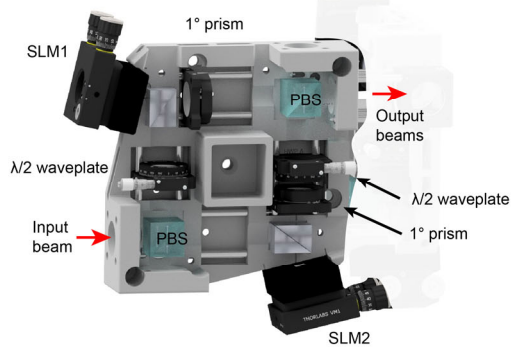
**B**



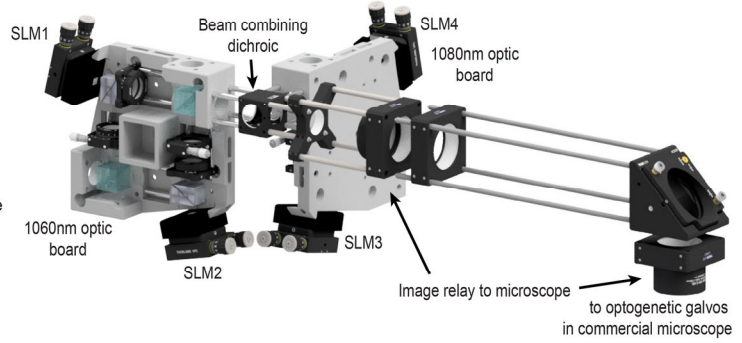
**C**



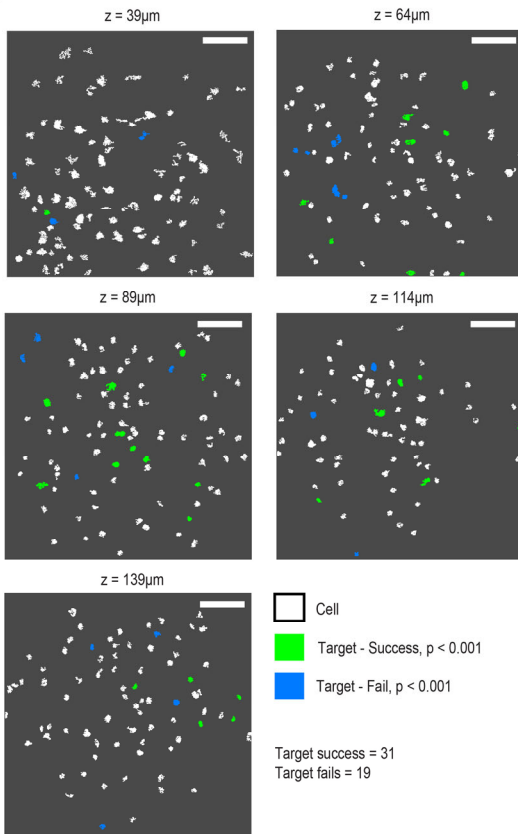
**D** View 1: Individual board



**E**



**F**



**G**

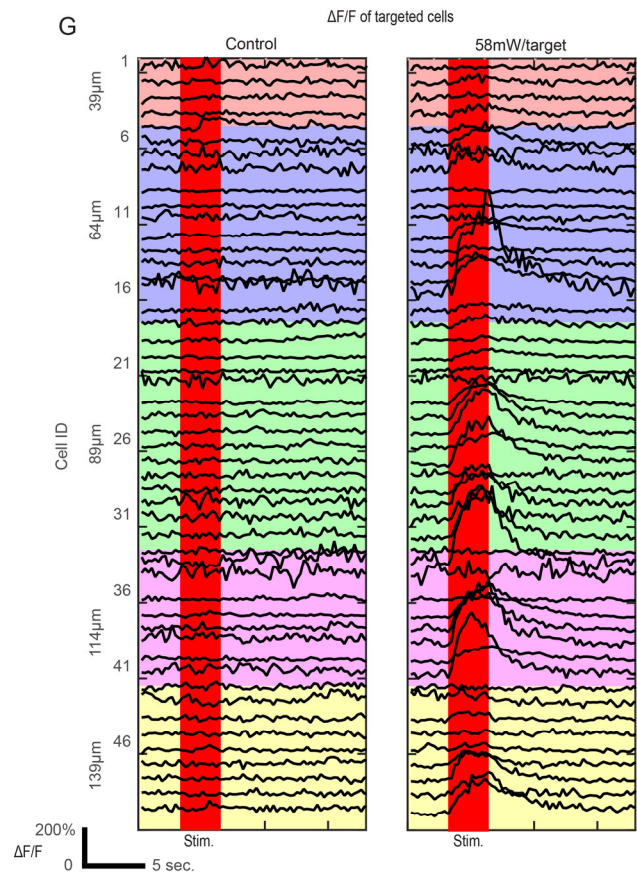




**Fig. S19. 4x MultiSLM for expanded addressable field of view.** (A) Spatial multiplexing of the sample field-of-view (FOV) is realized by dividing the field into quadrants and assigning a unique SLM to each one. This is implemented by placement of wedge prisms (Edmund Optics #45-558) in the optical path near each SLM face – adding a fixed  $1^\circ$  tilt offset to each beam. Each of the four tilting prisms is rotated  $90^\circ$  from each other such that all four SLM beams are tilted radially outward. This tilt of the optical beam will be scaled by the relay optics to the microscope objective to effectively tile the full, square FOV. This configuration substantially improves two-photon efficiency of diffracted spots across an enlarged field of view. (B) Theoretical multi-photon excitation efficiency across the  $450\ \mu\text{m}$  FOV of an Olympus 25x/1.05NA objective when using a conventional SLM ( $512 \times 512$  pixel array,  $15\ \mu\text{m}$  pixels, BNS/Meadowlark) which is scaled to realize a 0.48 NA photostimulation path. (C) Theoretical multi-photon excitation efficiency of the spatially multiplexed approach addresses the full FOV at high multi-photon excitation efficiency ( $> 0.7$ ) (scale bars  $50\ \mu\text{m}$ ). Values for two-photon efficiency (contours) take into account the quadratic dependence of the two-photon effect. (D) Mechanical layout of an individual SLM beam combination module dedicated for two SLM units. The layout is functionally similar to that described in **Fig. S7F** but scaled to accommodate the different sized SLMs. One additional utility of the board is to integrate the wedge prism close to the SLM face (the  $1^\circ$  prisms). Note that in this design there is only a single port where the optogenetic stimulation laser will enter before being selected by the polarizing beam splitter (PBS) to be directed to either of the two integrated SLMs. In this way, the input beam polarization can be rotated to continuously control the amount of power directed to either quadrant. The turning prism assembly for this design is a scaled version of that presented earlier so that it fit appropriately on the 3D printed assembly board. (E) Mechanical layout, combining two of the MultiSLM beam combination boards into a common optical path which is relayed to the optogenetic galvanometer set in the microscope. Each module has a dedicated laser and the two light sources are spectrally separated ( $\lambda_1 = 1060\ \text{nm}$  vs.  $\lambda_2 = 1080\ \text{nm}$ , Laser-femto Uranus). Each module can therefore be multiplexed onto a common optical axis by a beam combining dichroic (Semrock LPD02-1064RU), see **Fig. S18B**. The spectral- and polarization-multiplexed beams are then optically relayed into a commercial microscope (Bruker Ultima II) via a pair of lenses (Thorlabs AC508-400-B-ML,  $f = 400\ \text{mm}$  and Edmund Optics #49-391,  $f = 150\ \text{mm}$ , total magnification =  $0.375\times$ ) where the  $6\ \text{mm}$  clear aperture, optogenetic/uncaging galvanometers are utilized to generate the raster scanned spirals of the SLM-mediated focused points in the sample. (F) A random subset of 50 neurons expressing C1V1<sub>TT</sub> and GCaMP6m are targeted for stimulation in a  $450 \times 450 \times 100\ \mu\text{m}$  volume of layer 2/3 cortical cells (green, targeted cell showing statistically significant GCaMP response,  $p < 0.001$ , one-sided t-test, cyan, targeted cell not showing a response, white, other cells). (G) Comparison of the trial-averaged responses ( $N=5$  trials each for control and optogenetic stimulation) across all cells identified for targeting during randomized, no optogenetic stimulation control trials (left) versus in the presence of the optogenetic stimulation (right) ( $20\ \mu\text{m}$  diameter spirals,  $2.1\ \text{ms}$  exposure duration, 12 revolutions per spiral). The majority of targeted cells show a robust, statistically significant response in the stimulation period relative to the pre-stimulation baseline ( $p < 0.001$ , one-sided t-test). Successful targets are found throughout the volume, regardless of position.

## References and Notes

1. B. van Vugt, B. Dagnino, D. Vartak, H. Safaai, S. Panzeri, S. Dehaene, P. R. Roelfsema, The threshold for conscious report: Signal loss and response bias in visual and frontal cortex. *Science* **360**, 537–542 (2018). [doi:10.1126/science.aar7186](https://doi.org/10.1126/science.aar7186) [Medline](#)
2. M. R. Joglekar, J. F. Mejias, G. R. Yang, X.-J. Wang, Inter-areal balanced amplification enhances signal propagation in a large-scale circuit model of the primate cortex. *Neuron* **98**, 222–234.e8 (2018). [doi:10.1016/j.neuron.2018.02.031](https://doi.org/10.1016/j.neuron.2018.02.031) [Medline](#)
3. S. Dehaene, J.-P. Changeux, Experimental and theoretical approaches to conscious processing. *Neuron* **70**, 200–227 (2011). [doi:10.1016/j.neuron.2011.03.018](https://doi.org/10.1016/j.neuron.2011.03.018) [Medline](#)
4. G. A. Mashour, The controversial correlates of consciousness. *Science* **360**, 493–494 (2018). [doi:10.1126/science.aat5616](https://doi.org/10.1126/science.aat5616) [Medline](#)
5. D. K. Murphey, J. H. R. Maunsell, M. S. Beauchamp, D. Yoshor, Perceiving electrical stimulation of identified human visual areas. *Proc. Natl. Acad. Sci. U.S.A.* **106**, 5389–5393 (2009). [doi:10.1073/pnas.0804998106](https://doi.org/10.1073/pnas.0804998106) [Medline](#)
6. C. D. Salzman, K. H. Britten, W. T. Newsome, Cortical microstimulation influences perceptual judgements of motion direction. *Nature* **346**, 174–177 (1990). [doi:10.1038/346174a0](https://doi.org/10.1038/346174a0) [Medline](#)
7. H. Ko, S. B. Hofer, B. Pichler, K. A. Buchanan, P. J. Sjöström, T. D. Mrsic-Flogel, Functional specificity of local synaptic connections in neocortical networks. *Nature* **473**, 87–91 (2011). [doi:10.1038/nature09880](https://doi.org/10.1038/nature09880) [Medline](#)
8. A. Wertz, S. Trenholm, K. Yonehara, D. Hillier, Z. Raics, M. Leinweber, G. Szalay, A. Ghanem, G. Keller, B. Rózsa, K.-K. Conzelmann, B. Roska, Single-cell-initiated monosynaptic tracing reveals layer-specific cortical network modules. *Science* **349**, 70–74 (2015). [doi:10.1126/science.aab1687](https://doi.org/10.1126/science.aab1687) [Medline](#)
9. L. Cossell, M. F. Iacaruso, D. R. Muir, R. Houlton, E. N. Sader, H. Ko, S. B. Hofer, T. D. Mrsic-Flogel, Functional organization of excitatory synaptic strength in primary visual cortex. *Nature* **518**, 399–403 (2015). [doi:10.1038/nature14182](https://doi.org/10.1038/nature14182) [Medline](#)
10. H. Ko, L. Cossell, C. Baragli, J. Antolik, C. Clopath, S. B. Hofer, T. D. Mrsic-Flogel, The emergence of functional microcircuits in visual cortex. *Nature* **496**, 96–100 (2013). [doi:10.1038/nature12015](https://doi.org/10.1038/nature12015) [Medline](#)
11. W.-C. A. Lee, V. Bonin, M. Reed, B. J. Graham, G. Hood, K. Glattfelder, R. C. Reid, Anatomy and function of an excitatory network in the visual cortex. *Nature* **532**, 370–374 (2016). [doi:10.1038/nature17192](https://doi.org/10.1038/nature17192) [Medline](#)
12. L. L. Glickfeld, M. L. Andermann, V. Bonin, R. C. Reid, Cortico-cortical projections in mouse visual cortex are functionally target specific. *Nat. Neurosci.* **16**, 219–226 (2013). [doi:10.1038/nn.3300](https://doi.org/10.1038/nn.3300) [Medline](#)
13. C. Y. L. Huh, J. P. Peach, C. Bennett, R. M. Vega, S. Hestrin, Feature-specific organization of feedback pathways in mouse visual cortex. *Curr. Biol.* **28**, 114–120.e5 (2018). [doi:10.1016/j.cub.2017.11.056](https://doi.org/10.1016/j.cub.2017.11.056) [Medline](#)
14. S. N. Chettih, C. D. Harvey, Single-neuron perturbations reveal feature-specific competition in V1. *Nature* **567**, 334–340 (2019). [doi:10.1038/s41586-019-0997-6](https://doi.org/10.1038/s41586-019-0997-6) [Medline](#)

15. R. J. Douglas, C. Koch, M. Mahowald, K. A. Martin, H. H. Suarez, Recurrent excitation in neocortical circuits. *Science* **269**, 981–985 (1995). [doi:10.1126/science.7638624](https://doi.org/10.1126/science.7638624) [Medline](#)
16. A. D. Lien, M. Scanziani, Tuned thalamic excitation is amplified by visual cortical circuits. *Nat. Neurosci.* **16**, 1315–1323 (2013). [doi:10.1038/nn.3488](https://doi.org/10.1038/nn.3488) [Medline](#)
17. K. D. Harris, T. D. Mrsic-Flogel, Cortical connectivity and sensory coding. *Nature* **503**, 51–58 (2013). [doi:10.1038/nature12654](https://doi.org/10.1038/nature12654) [Medline](#)
18. B. K. Murphy, K. D. Miller, Balanced amplification: A new mechanism of selective amplification of neural activity patterns. *Neuron* **61**, 635–648 (2009). [doi:10.1016/j.neuron.2009.02.005](https://doi.org/10.1016/j.neuron.2009.02.005) [Medline](#)
19. D. O. Hebb, *Organization of Behavior* (Wiley, 1949).
20. C. Clopath, L. Büsing, E. Vasilaki, W. Gerstner, Connectivity reflects coding: A model of voltage-based STDP with homeostasis. *Nat. Neurosci.* **13**, 344–352 (2010). [doi:10.1038/nn.2479](https://doi.org/10.1038/nn.2479) [Medline](#)
21. L. Carrillo-Reid, W. Yang, Y. Bando, D. S. Peterka, R. Yuste, Imprinting and recalling cortical ensembles. *Science* **353**, 691–694 (2016). [doi:10.1126/science.aaf7560](https://doi.org/10.1126/science.aaf7560) [Medline](#)
22. R. Prakash, O. Yizhar, B. Grewe, C. Ramakrishnan, N. Wang, I. Goshen, A. M. Packer, D. S. Peterka, R. Yuste, M. J. Schnitzer, K. Deisseroth, Two-photon optogenetic toolbox for fast inhibition, excitation and bistable modulation. *Nat. Methods* **9**, 1171–1179 (2012). [doi:10.1038/nmeth.2215](https://doi.org/10.1038/nmeth.2215) [Medline](#)
23. J. P. Rickgauer, K. Deisseroth, D. W. Tank, Simultaneous cellular-resolution optical perturbation and imaging of place cell firing fields. *Nat. Neurosci.* **17**, 1816–1824 (2014). [doi:10.1038/nn.3866](https://doi.org/10.1038/nn.3866) [Medline](#)
24. A. M. Packer, L. E. Russell, H. W. P. Dalgleish, M. Häusser, Simultaneous all-optical manipulation and recording of neural circuit activity with cellular resolution in vivo. *Nat. Methods* **12**, 140–146 (2015). [doi:10.1038/nmeth.3217](https://doi.org/10.1038/nmeth.3217) [Medline](#)
25. W. Yang, L. Carrillo-Reid, Y. Bando, D. S. Peterka, R. Yuste, Simultaneous two-photon imaging and two-photon optogenetics of cortical circuits in three dimensions. *eLife* **7**, e32671 (2018). [doi:10.7554/eLife.32671](https://doi.org/10.7554/eLife.32671) [Medline](#)
26. A. R. Mardinly, I. A. Oldenburg, N. C. Pégard, S. Sridharan, E. H. Lyall, K. Chesnov, S. G. Brohawn, L. Waller, H. Adesnik, Precise multimodal optical control of neural ensemble activity. *Nat. Neurosci.* **21**, 881–893 (2018). [doi:10.1038/s41593-018-0139-8](https://doi.org/10.1038/s41593-018-0139-8) [Medline](#)
27. P. J. Keeling, F. Burki, H. M. Wilcox, B. Allam, E. E. Allen, L. A. Amaral-Zettler, E. V. Armbrust, J. M. Archibald, A. K. Bharti, C. J. Bell, B. Beszteri, K. D. Bidle, C. T. Cameron, L. Campbell, D. A. Caron, R. A. Cattolico, J. L. Collier, K. Coyne, S. K. Davy, P. Deschamps, S. T. Dyhrman, B. Edvardsen, R. D. Gates, C. J. Gobler, S. J. Greenwood, S. M. Guida, J. L. Jacobi, K. S. Jakobsen, E. R. James, B. Jenkins, U. John, M. D. Johnson, A. R. Juhl, A. Kamp, L. A. Katz, R. Kiene, A. Kudryavtsev, B. S. Leander, S. Lin, C. Lovejoy, D. Lynn, A. Marchetti, G. McManus, A. M. Nedelcu, S. Menden-Deuer, C. Miceli, T. Mock, M. Montresor, M. A. Moran, S. Murray, G. Nadathur, S. Nagai, P. B. Ngam, B. Palenik, J. Pawlowski, G. Petroni, G. Piganeau, M. C. Posewitz, K. Rengefors, G. Romano, M. E. Rumpho, T. Rynearson, K. B. Schilling, D. C. Schroeder, A. G. B. Simpson, C. H. Slamovits, D. R. Smith, G. J. Smith, S. R. Smith, H. M. Sosik, P. Stief, E.

- Theriot, S. N. Twary, P. E. Umale, D. Vaultot, B. Wawrik, G. L. Wheeler, W. H. Wilson, Y. Xu, A. Zingone, A. Z. Worden, The Marine Microbial Eukaryote Transcriptome Sequencing Project (MMETSP): Illuminating the functional diversity of eukaryotic life in the oceans through transcriptome sequencing. *PLOS Biol.* **12**, e1001889 (2014). [doi:10.1371/journal.pbio.1001889](https://doi.org/10.1371/journal.pbio.1001889) [Medline](#)
28. T.-W. Chen, T. J. Wardill, Y. Sun, S. R. Pulver, S. L. Renninger, A. Baohan, E. R. Schreiter, R. A. Kerr, M. B. Orger, V. Jayaraman, L. L. Looger, K. Svoboda, D. S. Kim, Ultrasensitive fluorescent proteins for imaging neuronal activity. *Nature* **499**, 295–300 (2013). [doi:10.1038/nature12354](https://doi.org/10.1038/nature12354) [Medline](#)
29. J. C. D. Kaufmann, B. S. Krause, C. Grimm, E. Ritter, P. Hegemann, F. J. Bartl, Proton transfer reactions in the red light-activatable channelrhodopsin variant ReaChR and their relevance for its function. *J. Biol. Chem.* **292**, 14205–14216 (2017). [doi:10.1074/jbc.M117.779629](https://doi.org/10.1074/jbc.M117.779629) [Medline](#)
30. D. Urmann, C. Lorenz, S. M. Linker, M. Braun, J. Wachtveitl, C. Bamann, Photochemical properties of the red-shifted channelrhodopsin Chrimson. *Photochem. Photobiol.* **93**, 782–795 (2017). [doi:10.1111/php.12741](https://doi.org/10.1111/php.12741) [Medline](#)
31. C. A. Baker, Y. M. Elyada, A. Parra, M. M. Bolton, Cellular resolution circuit mapping with temporal-focused excitation of soma-targeted channelrhodopsin. *eLife* **5**, e14193 (2016). [doi:10.7554/eLife.14193](https://doi.org/10.7554/eLife.14193) [Medline](#)
32. M. Dal Maschio, J. C. Donovan, T. O. Helmbrecht, H. Baier, Linking neurons to network function and behavior by two-photon holographic optogenetics and volumetric imaging. *Neuron* **94**, 774–789.e5 (2017). [doi:10.1016/j.neuron.2017.04.034](https://doi.org/10.1016/j.neuron.2017.04.034) [Medline](#)
33. J. Poort, A. G. Khan, M. Pachitariu, A. Nemri, I. Orsolich, J. Krupic, M. Bauza, M. Sahani, G. B. Keller, T. D. Mrsic-Flogel, S. B. Hofer, Learning enhances sensory and multiple non-sensory representations in primary visual cortex. *Neuron* **86**, 1478–1490 (2015). [doi:10.1016/j.neuron.2015.05.037](https://doi.org/10.1016/j.neuron.2015.05.037) [Medline](#)
34. A. Schoups, R. Vogels, N. Qian, G. Orban, Practising orientation identification improves orientation coding in V1 neurons. *Nature* **412**, 549–553 (2001). [doi:10.1038/35087601](https://doi.org/10.1038/35087601) [Medline](#)
35. Y. Fu, J. M. Tucciarone, J. S. Espinosa, N. Sheng, D. P. Darcy, R. A. Nicoll, Z. J. Huang, M. P. Stryker, A cortical circuit for gain control by behavioral state. *Cell* **156**, 1139–1152 (2014). [doi:10.1016/j.cell.2014.01.050](https://doi.org/10.1016/j.cell.2014.01.050) [Medline](#)
36. A. R. Seitz, D. Kim, T. Watanabe, Rewards evoke learning of unconsciously processed visual stimuli in adult humans. *Neuron* **61**, 700–707 (2009). [doi:10.1016/j.neuron.2009.01.016](https://doi.org/10.1016/j.neuron.2009.01.016) [Medline](#)
37. P. M. Goltstein, G. T. Meijer, C. M. Pennartz, Conditioning sharpens the spatial representation of rewarded stimuli in mouse primary visual cortex. *eLife* **7**, e37683 (2018). [doi:10.7554/eLife.37683](https://doi.org/10.7554/eLife.37683) [Medline](#)
38. E. L. Bienenstock, L. N. Cooper, P. W. Munro, Theory for the development of neuron selectivity: Orientation specificity and binocular interaction in visual cortex. *J. Neurosci.* **2**, 32–48 (1982). [doi:10.1523/JNEUROSCI.02-01-00032.1982](https://doi.org/10.1523/JNEUROSCI.02-01-00032.1982) [Medline](#)

39. H. Markram, W. Gerstner, P. J. Sjöström, A history of spike-timing-dependent plasticity. *Front. Synaptic Neurosci.* **3**, 4 (2011). [doi:10.3389/fnsyn.2011.00004](https://doi.org/10.3389/fnsyn.2011.00004) [Medline](#)
40. J. H. Marshel, T. Mori, K. J. Nielsen, E. M. Callaway, Targeting single neuronal networks for gene expression and cell labeling in vivo. *Neuron* **67**, 562–574 (2010). [doi:10.1016/j.neuron.2010.08.001](https://doi.org/10.1016/j.neuron.2010.08.001) [Medline](#)
41. Y. Yoshimura, J. L. M. Dantzker, E. M. Callaway, Excitatory cortical neurons form fine-scale functional networks. *Nature* **433**, 868–873 (2005). [doi:10.1038/nature03252](https://doi.org/10.1038/nature03252) [Medline](#)
42. E. J. Kim, A. L. Juavinett, E. M. Kyubwa, M. W. Jacobs, E. M. Callaway, Three types of cortical layer 5 neurons that differ in brain-wide connectivity and function. *Neuron* **88**, 1253–1267 (2015). [doi:10.1016/j.neuron.2015.11.002](https://doi.org/10.1016/j.neuron.2015.11.002) [Medline](#)
43. K. D. Harris, G. M. G. Shepherd, The neocortical circuit: Themes and variations. *Nat. Neurosci.* **18**, 170–181 (2015). [doi:10.1038/nn.3917](https://doi.org/10.1038/nn.3917) [Medline](#)
44. S. P. Brown, S. Hestrin, Intracortical circuits of pyramidal neurons reflect their long-range axonal targets. *Nature* **457**, 1133–1136 (2009). [doi:10.1038/nature07658](https://doi.org/10.1038/nature07658) [Medline](#)
45. M. Siegel, T. J. Buschman, E. K. Miller, Cortical information flow during flexible sensorimotor decisions. *Science* **348**, 1352–1355 (2015). [doi:10.1126/science.aab0551](https://doi.org/10.1126/science.aab0551) [Medline](#)
46. R. Romo, V. de Lafuente, Conversion of sensory signals into perceptual decisions. *Prog. Neurobiol.* **103**, 41–75 (2013). [doi:10.1016/j.pneurobio.2012.03.007](https://doi.org/10.1016/j.pneurobio.2012.03.007) [Medline](#)
47. C.-T. Law, J. I. Gold, Reinforcement learning can account for associative and perceptual learning on a visual-decision task. *Nat. Neurosci.* **12**, 655–663 (2009). [doi:10.1038/nn.2304](https://doi.org/10.1038/nn.2304) [Medline](#)
48. J. H. Marshel, M. E. Garrett, I. Nauhaus, E. M. Callaway, Functional specialization of seven mouse visual cortical areas. *Neuron* **72**, 1040–1054 (2011). [doi:10.1016/j.neuron.2011.12.004](https://doi.org/10.1016/j.neuron.2011.12.004) [Medline](#)
49. M. L. Andermann, A. M. Kerlin, D. K. Roumis, L. L. Glickfeld, R. C. Reid, Functional specialization of mouse higher visual cortical areas. *Neuron* **72**, 1025–1039 (2011). [doi:10.1016/j.neuron.2011.11.013](https://doi.org/10.1016/j.neuron.2011.11.013) [Medline](#)
50. M. M. Roth, F. Helmchen, B. M. Kampa, Distinct functional properties of primary and posteromedial visual area of mouse neocortex. *J. Neurosci.* **32**, 9716–9726 (2012). [doi:10.1523/JNEUROSCI.0110-12.2012](https://doi.org/10.1523/JNEUROSCI.0110-12.2012) [Medline](#)
51. G. N. Pho, M. J. Goard, J. Woodson, B. Crawford, M. Sur, Task-dependent representations of stimulus and choice in mouse parietal cortex. *Nat. Commun.* **9**, 2596 (2018). [doi:10.1038/s41467-018-05012-y](https://doi.org/10.1038/s41467-018-05012-y) [Medline](#)
52. M. Carandini, A. K. Churchland, Probing perceptual decisions in rodents. *Nat. Neurosci.* **16**, 824–831 (2013). [doi:10.1038/nn.3410](https://doi.org/10.1038/nn.3410) [Medline](#)
53. S. J. Yang, W. E. Allen, I. Kauvar, A. S. Andalman, N. P. Young, C. K. Kim, J. H. Marshel, G. Wetzstein, K. Deisseroth, Extended field-of-view and increased-signal 3D holographic illumination with time-division multiplexing. *Opt. Express* **23**, 32573–32581 (2015). [doi:10.1364/OE.23.032573](https://doi.org/10.1364/OE.23.032573) [Medline](#)

54. W. E. Allen, M. Z. Chen, N. Pichamoorthy, R. H. Tien, M. Pachitariu, L. Luo, K. Deisseroth, Thirst regulates motivated behavior through modulation of brainwide neural population dynamics. *Science* **364**, eaav3932 (2019). [Medline](#)
55. J. H. Jennings, C. K. Kim, J. H. Marshel, M. Raffiee, L. Ye, S. Quirin, S. Pak, C. Ramakrishnan, K. Deisseroth, Interacting neural ensembles in orbitofrontal cortex for social and feeding behaviour. *Nature* **565**, 645–649 (2019). [doi:10.1038/s41586-018-0866-8](https://doi.org/10.1038/s41586-018-0866-8) [Medline](#)
56. S. J. Bensmaia, L. E. Miller, Restoring sensorimotor function through intracortical interfaces: Progress and looming challenges. *Nat. Rev. Neurosci.* **15**, 313–325 (2014). [doi:10.1038/nrn3724](https://doi.org/10.1038/nrn3724) [Medline](#)
57. D. J. O’Shea, E. Trautmann, C. Chandrasekaran, S. Stavisky, J. C. Kao, M. Sahani, S. Ryu, K. Deisseroth, K. V. Shenoy, The need for calcium imaging in nonhuman primates: New motor neuroscience and brain-machine interfaces. *Exp. Neurol.* **287**, 437–451 (2017). [doi:10.1016/j.expneurol.2016.08.003](https://doi.org/10.1016/j.expneurol.2016.08.003) [Medline](#)
58. Y. S. Kim, H. E. Kato, K. Yamashita, S. Ito, K. Inoue, C. Ramakrishnan, L. E. Fenno, K. E. Evans, J. M. Paggi, R. O. Dror, H. Kandori, B. K. Kobilka, K. Deisseroth, Crystal structure of the natural anion-conducting channelrhodopsin GtACR1. *Nature* **561**, 343–348 (2018). [doi:10.1038/s41586-018-0511-6](https://doi.org/10.1038/s41586-018-0511-6) [Medline](#)
59. H. E. Kato, F. Zhang, O. Yizhar, C. Ramakrishnan, T. Nishizawa, K. Hirata, J. Ito, Y. Aita, T. Tsukazaki, S. Hayashi, P. Hegemann, A. D. Maturana, R. Ishitani, K. Deisseroth, O. Nureki, Crystal structure of the channelrhodopsin light-gated cation channel. *Nature* **482**, 369–374 (2012). [doi:10.1038/nature10870](https://doi.org/10.1038/nature10870) [Medline](#)
60. G. T. Prusky, R. M. Douglas, Characterization of mouse cortical spatial vision. *Vision Res.* **44**, 3411–3418 (2004). [doi:10.1016/j.visres.2004.09.001](https://doi.org/10.1016/j.visres.2004.09.001) [Medline](#)
61. A. Forli, D. Vecchia, N. Binini, F. Succol, S. Bovetti, C. Moretti, F. Nespoli, M. Mahn, C. A. Baker, M. M. Bolton, O. Yizhar, T. Fellin, Two-photon bidirectional control and imaging of neuronal excitability with high spatial resolution in vivo. *Cell Reports* **22**, 3087–3098 (2018). [doi:10.1016/j.celrep.2018.02.063](https://doi.org/10.1016/j.celrep.2018.02.063) [Medline](#)
62. G. Thalhammer, R. W. Bowman, G. D. Love, M. J. Padgett, M. Ritsch-Marte, Speeding up liquid crystal SLMs using overdrive with phase change reduction. *Opt. Express* **21**, 1779–1797 (2013). [doi:10.1364/OE.21.001779](https://doi.org/10.1364/OE.21.001779) [Medline](#)
63. E. Ronzitti, M. Guillon, V. de Sars, V. Emiliani, LCoS nematic SLM characterization and modeling for diffraction efficiency optimization, zero and ghost orders suppression. *Opt. Express* **20**, 17843–17855 (2012). [doi:10.1364/OE.20.017843](https://doi.org/10.1364/OE.20.017843) [Medline](#)
64. W. Yang, J. E. Miller, L. Carrillo-Reid, E. Pnevmatikakis, L. Paninski, R. Yuste, D. S. Peterka, Simultaneous multi-plane imaging of neural circuits. *Neuron* **89**, 269–284 (2016). [doi:10.1016/j.neuron.2015.12.012](https://doi.org/10.1016/j.neuron.2015.12.012) [Medline](#)
65. S. Quirin, D. S. Peterka, R. Yuste, Instantaneous three-dimensional sensing using spatial light modulator illumination with extended depth of field imaging. *Opt. Express* **21**, 16007–16021 (2013). [doi:10.1364/OE.21.016007](https://doi.org/10.1364/OE.21.016007) [Medline](#)

66. M. A. A. Neil, R. Juskaitis, M. J. Booth, T. Wilson, T. Tanaka, S. Kawata, Adaptive aberration correction in a two-photon microscope. *J. Microsc.* **200**, 105–108 (2000). [doi:10.1046/j.1365-2818.2000.00770.x](https://doi.org/10.1046/j.1365-2818.2000.00770.x) [Medline](#)
67. E. A. Pnevmatikakis, D. Soudry, Y. Gao, T. A. Machado, J. Merel, D. Pfau, T. Reardon, Y. Mu, C. Lacefield, W. Yang, M. Ahrens, R. Bruno, T. M. Jessell, D. S. Peterka, R. Yuste, L. Paninski, Simultaneous denoising, deconvolution, and demixing of calcium imaging data. *Neuron* **89**, 285–299 (2016). [doi:10.1016/j.neuron.2015.11.037](https://doi.org/10.1016/j.neuron.2015.11.037) [Medline](#)
68. H. H. Schütt, S. Harmeling, J. H. Macke, F. A. Wichmann, Painfree and accurate Bayesian estimation of psychometric functions for (potentially) overdispersed data. *Vision Res.* **122**, 105–123 (2016). [doi:10.1016/j.visres.2016.02.002](https://doi.org/10.1016/j.visres.2016.02.002) [Medline](#)
69. F. Perez, B. E. Granger, IPython: A system for interactive scientific computing. *Comput. Sci. Eng.* **9**, 21–29 (2007). [doi:10.1109/MCSE.2007.53](https://doi.org/10.1109/MCSE.2007.53)
70. E. A. Oliphant, *Guide to NumPy* (Trelgol Publishing, 2006).
71. J. D. Hunter, Matplotlib: A 2D graphics environment. *Comput. Sci. Eng.* **9**, 90–95 (2007). [doi:10.1109/MCSE.2007.55](https://doi.org/10.1109/MCSE.2007.55)
72. W. McKinney, in *Proceedings of the 9th Python in Science Conference* (2010), pp. 51–56.
73. F. Pedregosa, G. Varoquaux, A. Gramfort, V. Michel, B. Thirion, O. Grisel, M. Blondel, P. Prettenhofer, R. Weiss, V. Dubourg, J. Vanderplas, A. Passos, D. Cournapeau, M. Brucher, M. Perrot, É. Duchesnay, Scikit-learn: Machine learning in Python. *J. Mach. Learn. Res.* **12**, 2825–2830 (2011).
74. E. Jones, T. Oliphant, P. Peterson, others, *SciPy: Open source scientific tools for Python* (2001); [www.scipy.org/](http://www.scipy.org/).
75. S. Skipper, J. Perktold, in *Proceedings of the 9th Python in Science Conference* (2010), pp. 57–61.
76. H. E. Kato, Y. S. Kim, J. M. Paggi, K. E. Evans, W. E. Allen, C. Richardson, K. Inoue, S. Ito, C. Ramakrishnan, L. E. Fenno, K. Yamashita, D. Hilger, S. Y. Lee, A. Berndt, K. Shen, H. Kandori, R. O. Dror, B. K. Kobilka, K. Deisseroth, Structural mechanisms of selectivity and gating in anion channelrhodopsins. *Nature* **561**, 349–354 (2018). [doi:10.1038/s41586-018-0504-5](https://doi.org/10.1038/s41586-018-0504-5) [Medline](#)
77. W. Denk, J. H. Strickler, W. W. Webb, Two-photon laser scanning fluorescence microscopy. *Science* **248**, 73–76 (1990). [doi:10.1126/science.2321027](https://doi.org/10.1126/science.2321027) [Medline](#)
78. A. Cheng, J. T. Gonçalves, P. Golshani, K. Arisaka, C. Portera-Cailliau, Simultaneous two-photon calcium imaging at different depths with spatiotemporal multiplexing. *Nat. Methods* **8**, 139–142 (2011). [doi:10.1038/nmeth.1552](https://doi.org/10.1038/nmeth.1552) [Medline](#)
79. J. Kadmon, H. Sompolinsky, Transition to chaos in random neuronal networks. *Phys. Rev. X* **5**, 041030 (2015). [doi:10.1103/PhysRevX.5.041030](https://doi.org/10.1103/PhysRevX.5.041030)
80. Y. Song, F. DiMaio, R. Y.-R. Wang, D. Kim, C. Miles, T. Brunette, J. Thompson, D. Baker, High-resolution comparative modeling with RosettaCM. *Structure* **21**, 1735–1742 (2013). [doi:10.1016/j.str.2013.08.005](https://doi.org/10.1016/j.str.2013.08.005) [Medlines](#)

81. T. J. Dolinsky, J. E. Nielsen, J. A. McCammon, N. A. Baker, PDB2PQR: An automated pipeline for the setup of Poisson-Boltzmann electrostatics calculations. *Nucleic Acids Res.* **32**, W665–W667 (2004). [doi:10.1093/nar/gkh381](https://doi.org/10.1093/nar/gkh381) [Medline](#)
82. Z. Peng, Y. Liu, L. Yao, Z. Cao, Q. Mu, L. Hu, L. Xuan, Improvement of the switching frequency of a liquid-crystal spatial light modulator with optimal cell gap. *Opt. Lett.* **36**, 3608–3610 (2011). [doi:10.1364/OL.36.003608](https://doi.org/10.1364/OL.36.003608) [Medline](#)
83. J. Diels, W. Rudolf, *Ultrashort Laser Pulse Phenomena* (Academic Press, ed. 2, 2006).